Stresses, viscous flow and crystallization kinetics in thin films of amorphous chalcogenides used for optical data storage

von

Johannes Andreas Kalb

Diplomarbeit in Physik

vorgelegt der

Fakultät für Mathematik, Informatik und Naturwissenschaften
der Rheinisch-Westfälischen Technischen Hochschule Aachen

im April 2002

angefertigt am

I. Physikalischen Institut

Prof. Dr. Matthias Wuttig

Abstract

Modern computers usually contain several kinds of data storage devices. Very frequently magnetic and optical storage media are being used. The latter have become of great interest especially throughout the last decade: nowadays a significant amount of data is being stored on compact discs (CDs) and digital versatile discs (DVDs). Recently *rewritable* CDs have become commercially available. Their data storage layer usually consists of a thin film of a glass forming chalcogenide alloy (generally a Te alloy), which can be switched by laser heating locally and reversibly from the amorphous to the crystalline state. Rewritable DVDs and random access memories (RAMs) based on Te alloys are currently being developed. Therefore, it is important to enhance the insight into the material properties of Te alloys. For this reason thermal and mechanical properties of sputtered thin films of some of the most frequently used Te alloys $Ag_{0.055}In_{0.065}Sb_{0.59}Te_{0.29}$, $Ge_4Sb_1Te_5$ and $Ge_2Sb_2Te_5$ were studied by differential scanning calorimetry and wafer curvature measurements. The main focus was directed to the study of their *amorphous* phases.

Part I of this thesis deals with the *thermal* analysis of these Te alloys, based on differential scanning calorimetry measurements. The crystallization temperature and the heat of crystallization of the amorphous phases, the melting temperature and the heat of fusion of the crystalline phases, and the heat capacity of crystalline and liquid AgInSbTe were measured. The entropies of fusion are large ($\geq 2R$). In contrast to amorphous AgInSbTe and $Ge_4Sb_1Te_5$ which upon heating crystallize to a single phase within a small temperature interval, the crystallization of amorphous $Ge_2Sb_2Te_5$ was observed to be complicated by a subsequent cubic-to-hexagonal transformation. No thermal evidence of a glass transition was found below the crystallization temperatures. The ratio of the glass transition temperature (approximated as the crystallization temperature) to the liquidus temperature is 0.49–0.56, which identifies the materials as marginal glass formers. The heat capacity measurements on AgInSbTe were used to estimate the temperature dependence of the difference in enthalpy, entropy and Gibbs free energy between the undercooled liquid and the crystal.

Part II deals with the *mechanical* analysis of thin films of these Te alloys, based on wafer curvature measurements. The biaxial modulus and the linear coefficient of thermal expansion of the amorphous and crystalline phases were determined from stress versus temperature measurements on two different substrates. Viscous flow in the amorphous phase was measured by stress relaxation experiments under isothermal conditions. Far away from metastable equilibrium, the viscosity was found to increase linearly with time, which was attributed to bimolecular structural relaxation kinetics. The isoconfigurational activation energy of the viscosity was determined and scaled with the absolute melting temperature of the material. Additionally, the stress build-up caused by mass density changes upon crystallization of the amorphous phases was investigated, and experimental results were compared with computer simulations.

In Part III a preliminary model will be suggested, by which the crystallization mechanism of the Te alloys can be predicted. Based on the results from the viscosity measurements, this model yields a quantitative separation of nucleation and growth upon the crystallization of these alloys.

Contents

IV Appendix 143

List of Figures

List of Tables

Part I

Thermal analysis of thin amorphous chalcogenide films used for optical data storage

Chapter 1

Theoretical background

1.1 The glass transition

When a liquid is cooled below its melting point of liquidus temperature T_l, it either undergoes crystallization or retains the liquid structure. In the first case a crystalline solid is formed *discontinuously* by nucleation and growth of crystallites at the solid-liquid-interface. In the second case the liquid is being *undercooled* and is *continuously* hardened, which is observed by a large but continuous increase in its shear viscosity η that reflects the slowing dynamics in the liquid upon undercooling. The undercooled liquid is *metastable* with respect to the (stable) crystalline state but remains in *internal equilibrium*. This means that its molecular mobility is still large enough (i. e. its viscosity still low enough) to sample all thermodynamically accessible configurations. At the so-called *glass transition temperature* T_g the time scales necessary for atomic rearrangements have become larger than the experimentally imposed time window. Therefore, the undercooled liquid is configurationally frozen at T_g. As a consequence it is no longer in internal equilibrium. X-ray diffraction (XRD) experiments have shown that these frozen solids lack long-range translational symmetry. They exhibit the statistical structure of a liquid at a fixed time. This structure is commonly called *amorphous*. The solid itself is called a *glass*. The glass transition commonly occurs at the point where the shear viscosity η approaches a value of order of 10^{12} Pa·s [1].

At the end of the fifties, Cohen and Turnbull [2] made the important prediction of the *universality of the glass transition*: They postulated that *each* given liquid exhibits the glass transition if crystallization upon undercooling can be avoided. Ten years later, Turnbull [3] was able to identify the *reduced glass transition temperature* $T_{rg} = T_g/T_l$ as the quantitative measure for the *glass forming ability* of a given liquid: For $T_{rg} > \frac{2}{3}$, the viscosity increases very quickly upon undercooling. As a consequence, the maximum homogeneous crystal nucleation frequency is negligibly small in the regime of the undercooled liquid, and glass formation is *easy*[1]. In this case the critical (minimal) cooling rate $|\dot{T}_{min}|$ required to avoid crystallization is low. For $T_{rg} < \frac{1}{2}$, the viscosity increases rather slowly upon undercooling and the nucleation frequency is several orders of magnitude higher than for easy glass formers. Therefore, glass formation is rather *marginal*: the critical cooling rate is extremely high. Some of the easiest glass formers are SiO_2 ($T_{rg} = 0.835$) and B_2O_3 ($T_{rg} = 0.76$). Their critical cooling rate $|\dot{T}_{min}|$ is less than 10^{-2} Ks^{-1}. An example for a marginal glass former is $Fe_{95}B_5$ ($T_{rg} < 0.4$, $|\dot{T}_{min}| \approx 10^{12}$ Ks^{-1}) [4]. A crystalline solid is formed in case the cooling rate is lower than the critical cooling rate. In the last decades, glasses have indeed been found in materials of every bond type (covalent, ionic, metallic, van der Waals or hydrogen bonded), as predicted by Cohen and Turnbull.

It should be mentioned here that amorphous solids have also been formed by other methods than melt quenching, e. g. by vapor condensation, electrodeposition or sputtering.

1.2 The heat capacity C_p and the kinetic phenomenon of the glass transition

Characteristic for the glass transition is a sudden drop in the heat capacity C_p upon cooling[2] [5]. According to Fig. 1.1, the heat capacity of the undercooled liquid below the melting temperature T_m is higher than the heat capacity of the crystal due to the additional configurational degrees of freedom of a liquid[3]. Due to the freezing-out of the configurational modes of the liquid at T_g the heat capacity of glass and crystal

---

[1] see Appendix A

[2] The index p refers to the heat capacity at constant *pressure*.

[3] The assessment of a *unique* melting temperature is not obvious for the case of *alloys*, where melting generally occurs over a *range* of temperatures.

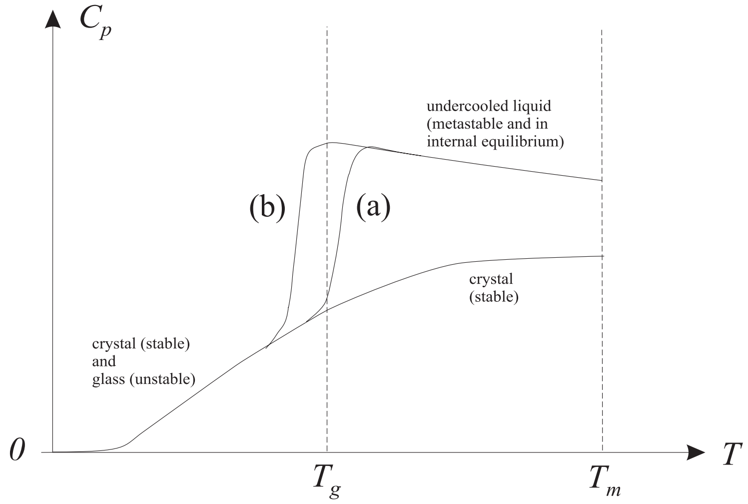

Figure 1.1: Heat Capacity C_p of a glass former in various stability regimes. (a) Fast cooling. (b) Slow cooling.

become approximately equal for $T < T_g$. However, the glass transition temperature depends on the cooling rate. For high cooling rates, the experimentally imposed time window for atomic rearrangements is smaller and the freezing occurs earlier, i. e. at lower viscosity or at higher temperature [path (a) in Fig. 1.1]. Slower cooling allows more time for equilibration upon cooling and results in path (b). Therefore, the glass transition is a *kinetic* and not a *thermodynamic* phenomenon.

1.3 Enthalpy H, Entropy S and Gibbs Free Energy G

The heat capacity C_p and the enthalpy H are related by

$$dH = C_p dT \tag{1.1}$$

Therefore, the difference in enthalpy ΔH_{lc} of the liquid and the crystal at a temperature T is given by

$$\boxed{\Delta H_{lc}(T) = H_l(T) - H_c(T) = \Delta H_f + \int\limits_{T_m}^{T} \Delta C_{p,lc}(T')dT'} \tag{1.2}$$

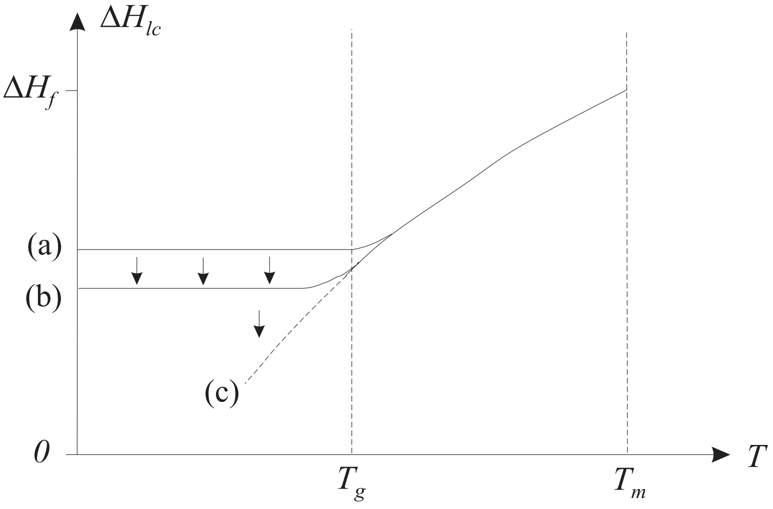

Figure 1.2: Difference in enthalpy H between liquid and crystal in two stability regimes: metastable equilibrium between T_g and T_m; unstable isoconfigurational states below T_g

where H_l and H_c are the enthalpy of the liquid and the crystal, respectively and $\Delta C_{p,lc} = C_{p,l} - C_{p,c}$ the difference in heat capacity between liquid and crystal. The integration constant $\Delta H_f = H_l(T_m) - H_c(T_m)$ is called the *heat of fusion*. It is the amount of heat, which additionally has to be provided to break bonds upon melting of a crystal. The result of the integration is shown qualitatively in Fig. 1.2. Slower cooling (b) leads to a lower ΔH_{lc} below T_g. Curve (c) is obtained by extrapolating the equilibrium curve of the undercooled liquid, which corresponds to the (theoretical) case of infinitively slow cooling. In this case the undercooled liquid remains in internal equilibrium without undergoing a glass transition. This is just due to the fact that the experimentally imposed time window is infinitively large, which means that the system has sufficient time for atomic rearrangements at arbitrary temperature. However, infinitively slow cooling is not possible *experimentally*: the undercooled liquid would crystallize for cooling rates lower than the critical cooling rate.

In order to get an expression for the entropy S, the total differential of the enthalpy

$$dH = TdS + VdP \tag{1.3}$$

has to be considered. Assuming constant pressure ($dP = 0$) and using Eq. (1.1), this results in

$$dS = C_p \frac{dT}{T} \tag{1.4}$$

The difference in entropy ΔS_{lc} of liquid and crystal as a function of temperature is obtained by integration:

$$\boxed{\Delta S_{lc}(T) = S_l(T) - S_c(T) = \Delta S_f + \int\limits_{T_m}^{T} \frac{\Delta C_{p,lc}(T')}{T'} dT'} \tag{1.5}$$

where S_l and S_c are the entropy of liquid and crystal respectively and the integration constant $\Delta S_f = S_l(T_m) - S_c(T_m)$ the *entropy of fusion*. A relation between ΔH_f and ΔS_f can be derived by using the definition of Gibbs free energy:

$$G = H - TS. \tag{1.6}$$

Therefore,

$$\Delta G_{lc}(T) = \Delta H_{lc}(T) - T\Delta S_{lc}(T). \tag{1.7}$$

For a single component system,

$$\Delta G_{lc}(T_m) = 0, \tag{1.8}$$

and therefore

$$\boxed{\Delta S_f = \frac{\Delta H_f}{T_m}}. \tag{1.9}$$

Figure 1.3 displays the temperature dependence of the entropy obtained from integration. According to Kauzmann [5], both ΔS_{lc} and ΔH_{lc} decrease upon cooling from T_m to T_g by a factor of two or more. Extrapolation (Fig. 1.3c) of the equilibrium curve to temperatures below T_g yields $\Delta S_{lc} = 0$ at a temperature $T_k > 0$ [5]. For many materials, T_k has been obtained from heat capacity measurements in the regime of the undercooled liquid. As a result of extrapolation, T_k and T_g differed generally by a few tens of degrees. T_k is commonly called the *Kauzmann temperature*. ΔS_{lc} remains zero for $T < T_k$. Therefore, the undercooled liquid in internal equilibrium becomes *fully ordered* at low temperatures. At first sight, a fully ordered non-crystalline solid seems to be paradox. A solution of this problem is given in Chapter 1.5.

Figure 1.4 displays the Gibbs free energy G, which can be obtained in two ways: one option is to substitute Eqs. (1.2) and (1.5) into Eq. (1.7). The other option is to consider the total differential for G,

$$dG = -SdT + VdP. \tag{1.10}$$

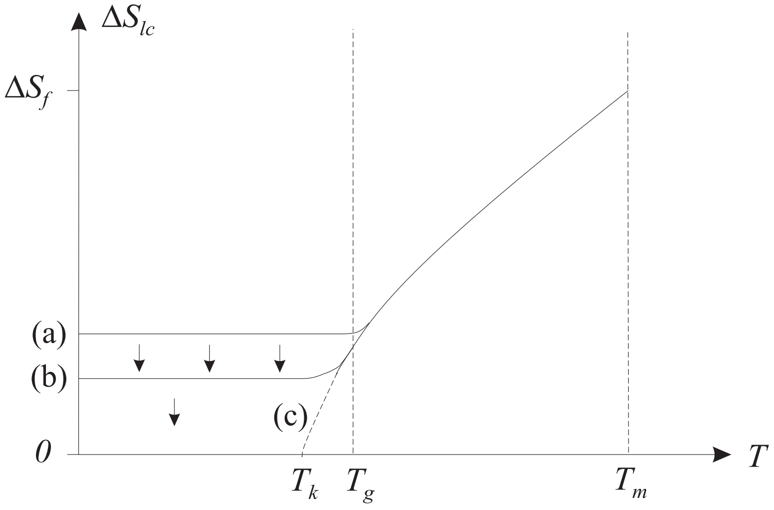

Figure 1.3: Difference in entropy S between liquid and crystal in two stability regimes: metastable equilibrium between T_g and T_m; unstable isoconfigurational states below T_g

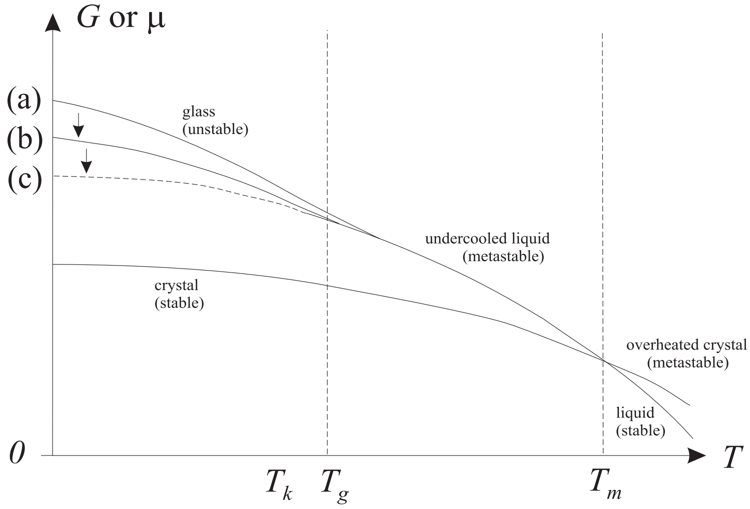

Figure 1.4: Gibbs free energy G or chemical potential $\mu = \frac{G}{N}$ (N = number of particles) in various stability regimes

For $dP = 0$,

$$\boxed{\Delta G_{lc}(T) = G_l(T) - G_c(T) = -\int_{T_m}^{T} \Delta S_{lc}(T')dT'}. \tag{1.11}$$

Due to Eq. (1.8) the integration constant vanishes here.

1.4 Isoconfigurational states and structural relaxation

Due to the freezing-out of the undercooled liquid at the glass transition temperature T_g, the atomic configuration of the glasses shown in path (a) and (b) of Figs. 1.2–1.4 is equal to an *instantaneous* configuration of the undercooled liquid at T_g. Therefore, path (a) and (b) are commonly called *isoconfigurational states.* The undercooled liquid is said to be *configurationally frozen* at T_g.

As already mentioned, all glasses are unstable due to the fact that they have gone out of equilibrium at T_g. One of the most basic laws of thermodynamics is the *equilibrium condition*, which states that all non-equilibrium systems tend to approach the equilibrium again. For the case of a system at constant temperature and pressure, this condition says

$$\boxed{G(T,p) = \text{minimum} \qquad (T,\, p \text{ externally imposed})}. \tag{1.12}$$

Therefore, glasses continuously lower their Gibbs free energy in order to approach their equilibrium structure [curve (c) in Figs. 1.2–1.4]. This process is commonly called *structural relaxation* and is indicated by the arrows in Figs. 1.2–1.4. On the other hand, if a glass is heated quickly above T_g (Fig. 1.5), one obtains an overheated glass. In this case, entropy and enthalpy *increase* continuously with time due to structural relaxation. Once equilibrium is reached, structural relaxation stops. However, in most cases the glass crystallizes before approaching equilibrium. Therefore, the experimental determination of equilibrium properties of glasses is often difficult.

As a consequence of structural relaxation, each material property of a glass that depends on atomic configuration is time-dependent at constant temperature and depends on the thermal history of the glass [6]. This causes serious problems in studying

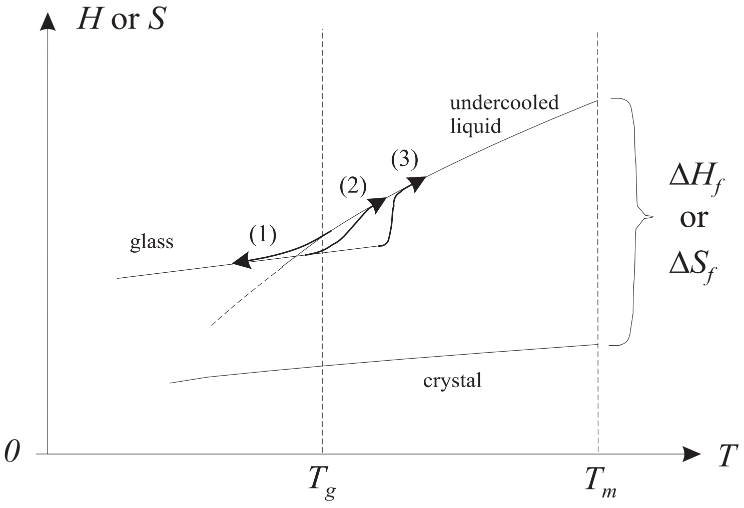

Figure 1.5: Hysteresis effects around the glass transition. (1) Cooling. (2) Slow heating. (3) Quick heating.

properties of amorphous materials experimentally. For example, the electrical resistivity changes by about 1%, Young's modulus by about 5 – 10% and the mass density by about 0.5% [7]. However, atomic transport coefficients exhibit the most significant changes: the shear viscosity η and the diffusivity D often change by several orders of magnitude [8, 9, 10, 11]. This is investigated in more detail in Part II of this thesis.

1.5 Atomic order

The *short range* atomic order in simple liquids or glasses[4] is similar to the order in icosahedral *quasicrystals*. Figure 1.6(a) displays the shape of an icosahedron. It is formed by 20 tetrahedra, which share a common vertex [Fig. 1.6(b)]. This can only be achieved by slight distortion of each tetrahedron – an atom is about 5% further apart from its neighbors on the surface of the icosahedron than it is from the atom at the center.

In an icosahedral quasicrystal, the icosahedral clusters are arranged to give long-range quasiperiodicity. This results in five-fold-symmetry axes. The x-ray diffraction (XRD) pattern of a quasicrystal exhibits discrete peaks similar to periodic crystals.

---

[4] Simple liquids or glasses consist of atoms or molecules interacting by spherically symmetrical potentials, e. g. metallic or van der Waals systems.

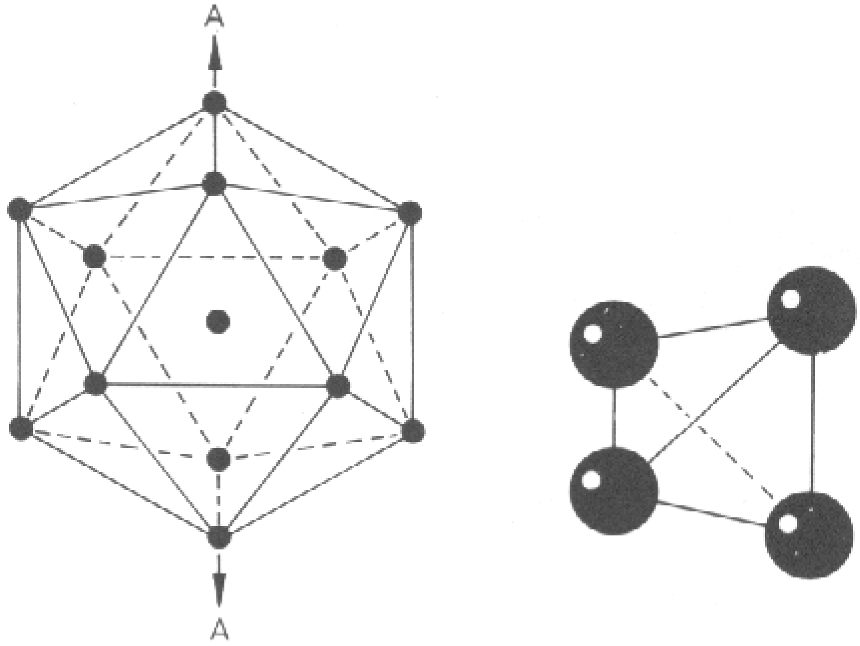

(a) The icosahedron exhibits 12 vertices and six five-fold symmetry axes: the line AA is one of them.

(b) Arranging 20 slightly distorted tetrahedra to share a common vertex results in the icosahedron of (a).

Figure 1.6: Icosahedral arrangement of atoms. From [12].

Therefore, a quasicrystal is really a crystal: instead of having a periodic structure, it has a quasiperiodic structure: This means that one needs a finite number of integers that is greater than the dimensionality of the space to specify the quasilattice coordinates or to index the diffraction peaks. For an icosahedral quasicrystal, this number is six, whereas it is only three for a periodic crystal.

In a glass or a liquid, the atomic structure is also polytetrahedral as for the case of quasicrystals. In many glasses the *short range* order even resembles icosahedral arrangement. However, glasses do not exhibit a periodic or quasi-periodic *long range* order. Their XRD pattern is continuous and cannot be specified by a finite number of integers. This also applies to the fully ordered amorphous equilibrium state, which is obtained theoretically by infinitively slow cooling [curve (c) in Figs. 1.2–1.4]. In this case, the full order is not obtained by periodicity or quasi-periodicity but by formulating a set of short-range order rules, which do not allow any choices during the construction of the entire phase. This results in a *unique* state with an entropy equal to zero. As already mentioned, the fully ordered amorphous state cannot be obtained experimentally due to equilibration times becoming infinitely long. Therefore, all glasses have a certain amount of residual entropy at low temperatures, which indicates that they have gone out of equilibrium at the glass transition.

1.6 Crystallization

The Gibbs free energy is not only the driving force for structural relaxation but also for crystallization: According to Fig. 1.4 and Eq. (1.12) the crystal is the thermodynamically most favorable structure below the melting temperature. Therefore, all glasses tend to crystallize. However, due to the fact that crystallization is thermally activated,[5] it is a function of time *and* temperature. Glasses can resist crystallization much longer at lower temperatures. It is not uncommon that they remain amorphous for several decades (or even more) at room temperature. Around the glass transition temperature (or at even higher temperatures), marginal glass formers often crystallize much more quickly than easy glass formers. In this temperature regime, crystallization times can vary by several orders of magnitude between different glasses and can be

---

[5] For more details see Chapter 8.

even shorter than a second. In case a glass crystallizes quickly in the regime of the undercooled liquid, the experimental study of physical quantities in this temperature range is extremely difficult: the time window is just too small for most measurements. Therefore, in order to obtain information about the undercooled liquid and its crystallization kinetics, one has to rely on measurements in the amorphous, crystalline and liquid state in this case.

Chapter 2

Experimental details

2.1 Samples

Crystallization kinetics of three different amorphous Te alloys have been investigated by analyzing some of their thermal properties experimentally:

(a) AgInSbTe (for a precise specification of the composition see Chapter 2.2)

(b) $Ge_4Sb_1Te_5$

(c) $Ge_2Sb_2Te_5$

Characteristic for these glass forming Te alloys is an extremely strong temperature dependence of their time window of crystallization: They can remain amorphous for many decades at room temperature but crystallize in a split microsecond at elevated temperatures [13, 14]. This makes them applicable for *fast* optical data storage in *rewritable* compact discs (CDs). They can be switched within short time intervals by laser heating locally and reversibly from the amorphous to the crystalline state [15, 16, 17, 18]. These states have different reflectivities and can therefore be distinguished optically. Commercially available CDs are coated by a *thin film* of one of the Te alloys listed above. These films are initially crystalline. An amorphous bit (diameter $d < 1\,\mu\mathrm{m}$) in this crystalline matrix is written by locally melting the matrix. Due to the short duration of the laser pulse and the small bit diameter, the cooling rate in the bit area is extremely high ($|\dot{T}| > 10^{10}\ \mathrm{K\,s^{-1}}$)) and the undercooled melt becomes amorphous. Reliable data storage is guaranteed as the bit remains amorphous for many decades at room temperature. However, in order to obtain a *re*writable CD, *quick externally controlled* bit erasure (re-crystallization) must also be guaranteed. This is obtained by heating the bit to elevated temperatures using laser power. As the bit temperature can be adjusted via the choice of the power and due to the fact that crystallization is a function of time *and* temperature, the re-crystallization time can be minimized by carefully determining an appropriate laser power. This has been done for the Te alloys listed above. For instance, re-crystallization of $Ge_2Sb_2Te_5$ was reported to be possible within less than 10 ns, while 16 ns were necessary for the re-crystallization of $Ge_4Sb_1Te_5$ [14]. Due to the fact that these materials can undergo such phase transformations on very short time scales, they are called *phase change materials* in the data storage community.

The present demanding challenge of research is to make use phase change materials more widespread. For instance, rewritable digital versatile discs (DVDs) and random access memories (RAMs) based on phase change materials are currently being developed. For this purpose (a) the data storage density, (b) the durability (cyclability) of the media and (c) the data transfer rate has to be increased.

(a) The storage density could be increased by decreasing the bit diameter, which would be possible by decreasing the laser wavelength.

(b) The cyclability is probably the most serious problem: due to the density change upon the phase transition of order of 5–10% [13, 19, 20] large stresses are induced, which result in irreversible mechanical deformations. Therefore, the material ages after a finite amount of write-erase cycles and the media has to be replaced. This still hampers rewritable CDs to replace mass storage devices like magnetic hard discs. Stress formation is analyzed in detail in Part II of this thesis.

(c) The data transfer rate can only be increased by accelerating the re-crystallization process, which is still the time-limiting factor. The differential scanning calorimetry (DSC) measurements presented in Part I of this thesis are helpful to get insight into the kinetics of crystallization and glass formation.

2.2 Sample preparation

Phase change films of approximately 7 µm thickness were deposited on thin plates of stainless steel by direct current magnetron sputtering. The background pressure was approximately 10^{-6} mbar and the working pressure during sputtering in Ar ambient $7 \cdot 10^{-3}$ mbar. The sputtering power was 100 W. As determined from XRD measurements, the structure of the as-deposited films was amorphous [13, 14]. Subsequently the film was peeled off by substrate bending in order to obtain fragments on the order of a few square millimeters.

The specification of composition of the sputtering targets obtained from the manufacturer was verified by inductive coupled argon plasma emission spectroscopy and energy dispersive x-ray analysis:

(a) Ag 5.5%, In 6.5%, Sb 59%, Te 29% (atomic %) [13]

(c) Ge 21.9%, Sb 24.1%, Te 54.0% (atomic %)

For $Ge_4Sb_1Te_5$ a precise verification has not been done and the specification from the manufacturer was taken for granted.

At this point it should be noted that these samples were prepared at the RWTH Aachen but the measurements were performed at Harvard University in Cambridge. As a consequence, the time between sample preparation and actual measurement was approximately two to three weeks. In order to reduce sample oxidation, the sample fragments were sealed in small closeable test tubes until they were used for the measurements.

2.3 Experimental setup

A calibrated power-compensated differential scanning calorimeter (DSC) was employed in order to measure thermal properties of Te alloys. This device is a highly sensitive instrument, which measures the heat flow $\dot{H} = dH/dt$ (H: enthalpy) into a material as it is gradually heated. $\dot{H}$ is determined by measuring the power required to maintain a superimposed temperature change in the sample. Typically 30 mg of sample fragments were sealed in both standard aluminum and platinum pans[1] and were scanned

---

[1] Pan dimensions: cylindrically shaped, approximately 6 mm diameter and 2 mm height.

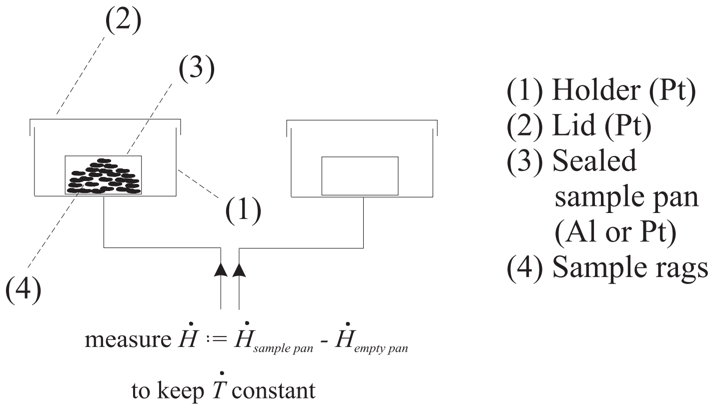

Figure 2.1: Differential scanning calorimetry (DSC) technique

at constant heating rates from room temperature to 600 ℃ (aluminum pans) and 660 ℃ (platinum pans). Above 600 ℃, aluminum melts, and above 660 ℃, reactions occurred between the sample and the platinum of the pans, which limited the range of the measurements. High purity argon was used to provide an inert atmosphere. In order to subtract out the heat that flows into the sample holder and the sample pan, a sample holder with an empty sample pan was used as a reference. In other words, the device determined the *net* heat flow into the sample fragments by comparing the heat flow into the filled and the unfilled holder (Fig 2.1).

As a material is heated up it may respond with various chemical and physical transformations. These transformations are either endothermic (solid-state transitions, crystal melting, glass transition, endothermic chemical reactions) or exothermic in nature (crystallization, exothermic chemical reactions). For the phase change materials, a scanning at constant heating rates allowed the determination of the glass transition temperature T_g, the onset temperature of crystallization T_c, the peak temperature of crystallization $T_{c,p}$, the temperature where crystallization is completed T_f, the solidus temperature T_s, the peak melting temperature T_m, the liquidus temperature T_l, the heat of crystallization ΔH_c and the heat of fusion ΔH_f from the thermal curves. As already mentioned in Chapter 1, both the glass transition temperature and the crystallization temperature are expected to depend on the heating rate $\dot{T}$.

Chapter 3

Results and discussion

3.1 Crystallization and melting

3.1.1 AgInSbTe

Figure 3.1 displays the heat flow $\dot{H}$ as a function of temperature T for AgInSbTe in the vicinity of 170 °C (heating rate: 5 K/min)[1]. From earlier x-ray diffraction (XRD) measurements [13], the exothermic peak can be identified with the crystallization of the initially amorphous sample. The onset temperature of crystallization T_c, the peak temperature of crystallization $T_{c,p}$, and the temperature where crystallization is completed T_f are listed in Table 3.1. These temperatures are close to the values determined from measurements of the electrical film resistance [13]. In order to obtain the heat of crystallization ΔH_c, the peak had to be integrated numerically [21]:

$$\Delta H_c = \int\limits_{peak} \dot{H} dt = \int\limits_{peak} \dot{H} \frac{dT}{\dot{T}} \tag{3.1}$$

The straight line, which connects T_c and T_f, was chosen as the baseline for this numerical integration[2]. The result is displayed in Table 3.3.

---

[1] All heat flow data presented in this Chapter were normalized with respect to the *amount of substance*. '1 mol' was defined as an amount of $6.022 \cdot 10^{23}$ *atoms*, independent of whether they were Ag, In, Ge, Sb or Te atoms.

[2] The DSC device is only able to measure $\dot{H}$ with respect to an *unknown* baseline $\dot{H}_0(T)$. This baseline may also be temperature dependent. Therefore, the offset of the heat flow axis in all DSC figures is chosen arbitrarily.

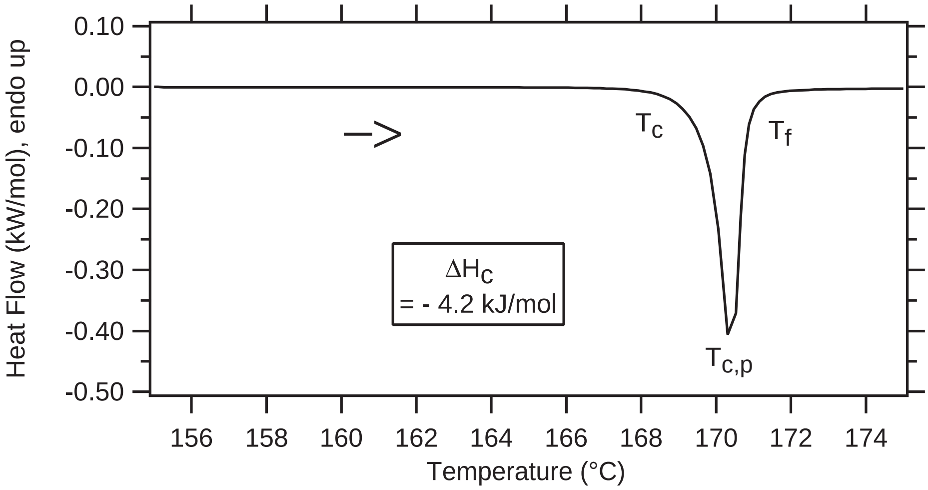

Figure 3.1: Heat flow $\dot{H}$ as a function of temperature for AgInSbTe (heating rate: 5 K/min). The arrow indicates the direction of temperature change. The phrase 'endo up' on the vertical axis is short for 'endothermic signal in positive direction'. The exothermic peak is due to crystallization of the initially amorphous sample. Sample pan material: Al.

It should be mentioned here that the heat of crystallization ΔH_c depends on the thermal history of the sample: By comparison with Fig. 1.2, the heat of crystallization corresponds to the distance between a corresponding isoconfigurational state and the horizontal axis. Obviously, the exact isoconfigurational state at the onset of crystallization is not known as it depends on heating rate and thermal history. However, no heating rate dependence of ΔH_c was observed within range of error for heating rates between 5 K/min and 80 K/min. Therefore, it can be concluded that the effect of structural relaxation on the magnitude of ΔH_c is negligible within the range of heating rates employed.

Upon further heating [Fig. (3.2)], the sample melts, which is accompanied by an endothermic peak. This occurs over a temperature range. The solidus temperature T_s, the peak melting temperature T_m and the liquidus temperature T_l were determined from Fig. 3.2 and are listed in Table 3.2. T_m approximately coincides with the literature value [22] for the alloy Sb_2Te, which is similar in composition to AgInSbTe. The heat of fusion ΔH_f, obtained from peak integration according to Eq. (3.1), is given in Table 3.3. The straight line that connects T_s and T_l was chosen as the baseline for this integration. Upon cooling down (Fig. 3.2), the sample re-crystallizes again, producing

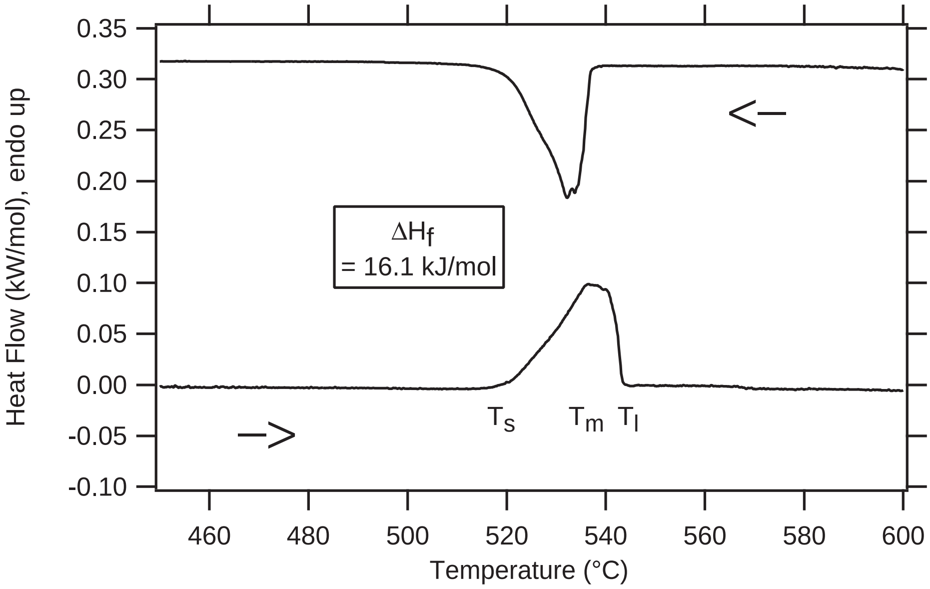

Figure 3.2: Heat flow $\dot{H}$ as a function of temperature for AgInSbTe at heating (cooling) rate of 5 K/min. The arrows indicate the direction of temperature change. The endothermic peak is due to melting of the crystal and the exothermic peak due to solidification of the melt. The temperature axis was calibrated for the heating signal only. Sample pan material: Al.

an exothermic peak of the same area, implying that the heat of fusion is equal to the heat of solidification. The occurrence of the solidification peak shows that the cooling rate of 5 K/min was not high enough to form a glass by melt-quenching. In contrast to the heat of crystallization, the heat of fusion is not expected to depend on thermal history, due to the *thermodynamic* phenomenon of melting. In order to check reversibility, each sample was subsequently heated up a second time. In the heating signal of the re-scan no crystallization peak occurred any more as expected (not shown), as the sample was already crystalline. However, the melting peak and the re-solidification peak of the same peak area were observed again, implying that no material was lost.

3.1.2 $Ge_4Sb_1Te_5$

Figure 3.3 displays the exothermic crystallization peak for $Ge_4Sb_1Te_5$ (heating rate: 5 K/min). The crystallization temperature (Table 3.1) is close to the results from XRD and electrical film resistance measurements [14]. The heat of crystallization is similar

Table 3.1: Onset temperature of crystallization T_c, peak temperature of crystallization $T_{c,p}$, and temperature where crystallization is completed T_f for three Te alloys. The superscript indicates heating rate at which the data were taken (5 K/min, 40 K/min or 80 K/min.)

	$T_c^{(5)}$ (°C)	$T_{c,p}^{(5)}$ (°C)	$T_f^{(5)}$ (°C)	$T_c^{(40)}$ (°C)	$T_{c,p}^{(40)}$ (°C)	$T_f^{(40)}$ (°C)	$T_c^{(80)}$ (°C)	$T_{c,p}^{(80)}$ (°C)	$T_f^{(80)}$ (°C)
AgInSbTe	168	170.3	172	179	181.6	186	183	185.6	203
$Ge_4Sb_1Te_5$	185	190.2	194	... [a]	...	...	200	203.7	215
$Ge_2Sb_2Te_5$	101	155.1	~ 280	...	...	...	150	173.1	~ 310

[a] no data available

Table 3.2: Solidus temperature T_s, peak temperature in the melting signal T_m, liquidus temperature T_l and reduced glass transition temperature T_{rg} for three Te alloys. The data were taken for a heating rate of 5 K/min.

	T_s (°C)	T_m (°C)	T_l (°C)	$T_{rg} = \frac{T_g}{T_l}$
AgInSbTe	516	537	544	0.56
$Ge_4Sb_1Te_5$	642 [a]	... [b]	694 [a]	0.49
$Ge_2Sb_2Te_5$	610	621	638	0.49

[a] from Ref. [23]
[b] no data available

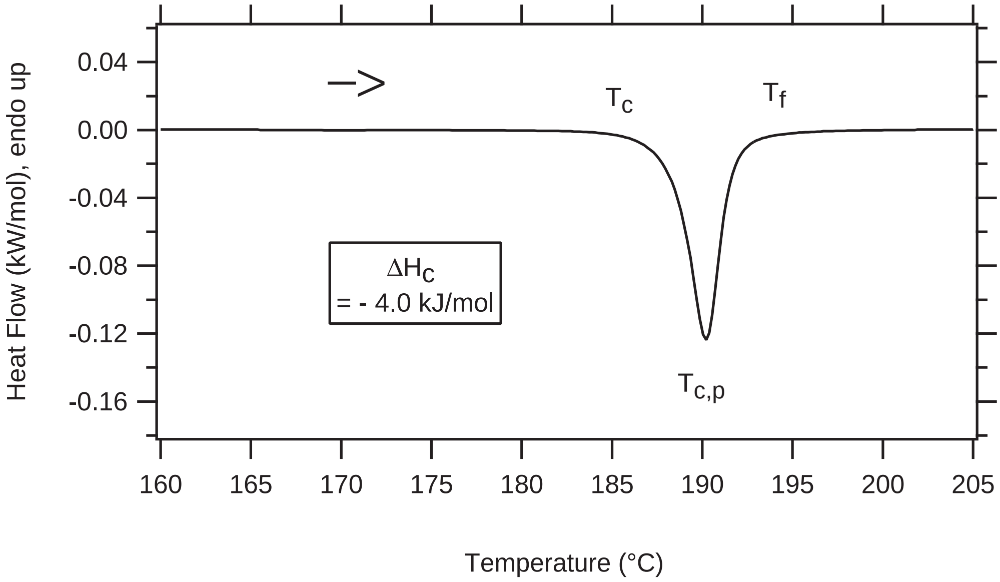

Figure 3.3: Heat flow $\dot{H}$ as a function of temperature for $Ge_4Sb_1Te_5$ (heating rate: 5 K/min). The arrow indicates the direction of temperature change. The exothermic peak is due to crystallization of the initially amorphous sample. Sample pan material: Al.

to AgInSbTe (Table 3.3) and was observed to be independent of heating rate within range of error for $\dot{T} \leq 80\,\mathrm{K/min}$. The peak shape of $Ge_4Sb_1Te_5$ differs slightly from AgInSbTe: for $Ge_4Sb_1Te_5$, it is broader and less high. Clear indications for melting of $Ge_4Sb_1Te_5$ could not be observed below 660 °C. For the sake of completeness, T_s and T_l were taken from literature values [23] for Ge-Sb-Te alloys that exhibit a composition close to $Ge_4Sb_1Te_5$ (Table 3.2).

3.1.3 $Ge_2Sb_2Te_5$

The results for $Ge_2Sb_2Te_5$ are shown in Figs. 3.4 and 3.5. In contrast to AgInSbTe and $Ge_4Sb_1Te_5$, crystallization in this alloy occurs over a range of temperatures. A sharp peak is observed at $T_{c,p} = 155.1$ °C and a second (much broader) peak at around 200 °C. By comparing the entire curve to the re-scan of the crystallized sample, the onset of crystallization is found to occur around $T_c = 101$ °C. The end of the transformation process is not well defined and can therefore only be estimated as 280±30 °C. This uncertainty produces a larger error in the heats of transformation. XRD measurements have shown that the main peak at $T_{c,p} = 155.1$ °C is due to crystallization to a cubic phase,

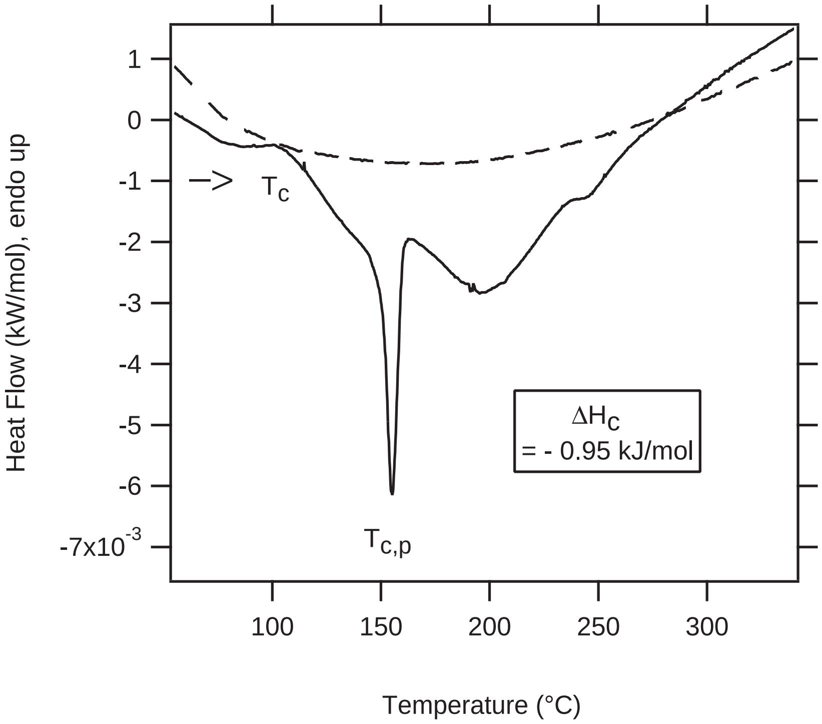

Figure 3.4: Heat flow $\dot{H}$ as a function of temperature for $Ge_2Sb_2Te_5$ (heating rate: 5 K/min). Solid curve: exothermic signal due to crystallization of the initially amorphous sample and subsequent crystal-to-crystal transformation. Dashed curve: signal upon rerun (same heating rate). Sample pan material: Al.

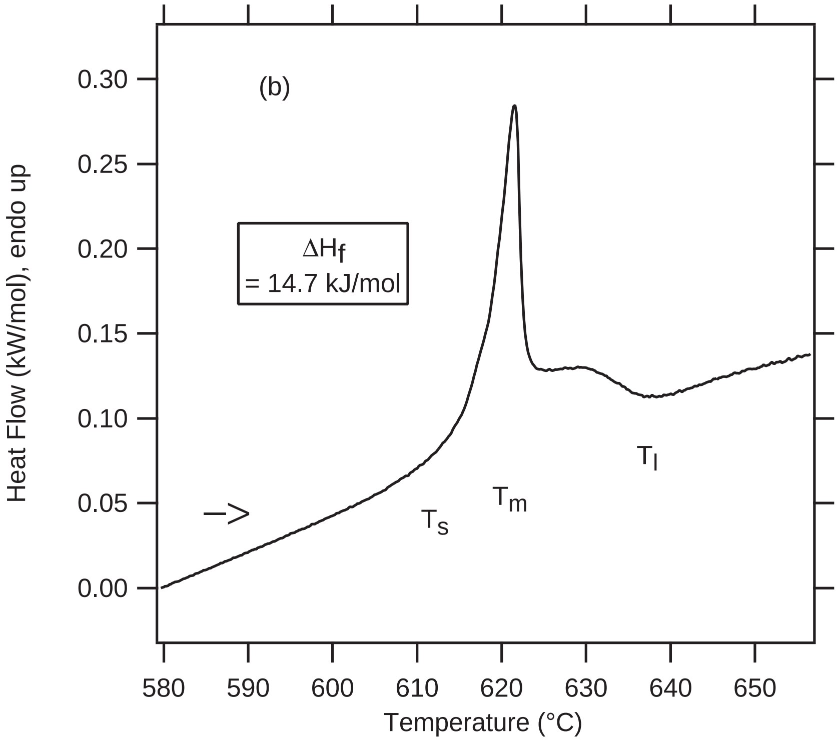

Figure 3.5: Heat flow $\dot{H}$ as a function of temperature for $Ge_2Sb_2Te_5$ (heating rate: 5 K/min). The endothermic signal is due to melting of the crystalline sample. Sample pan material: Pt.

whereas the second peak at 200 ℃ results from a transformation from the cubic to a hexagonal crystalline phase [14, 24]. In contrast, the structure of crystalline AgInSbTe and $Ge_4Sb_1Te_5$ is stable at all temperatures up to T_s (hexagonal for AgInSbTe and cubic for $Ge_4Sb_1Te_5$) and a second peak is not observed for these two alloys. The heat of crystallization of $Ge_2Sb_2Te_5$ is estimated by integrating the transformation signal between $T_c = 101$ ℃ and $T = 163$ ℃, at which the signal has a minimum. This gives an estimated value of $\Delta H_c = 0.95 \pm 0.30\,\mathrm{kJ/mol}$. The remainder of the signal, which is assigned to the heat of the cubic-to-hexagonal transformation ΔH_{c-h}, integrates to $\Delta H_{c-h} = 1.80 \pm 0.70\,\mathrm{kJ/mol}$. The signal upon rerun was used as the baseline for these integrations. The heat of crystallization ΔH_c is significantly smaller for $Ge_2Sb_2Te_5$ than for AgInSbTe and $Ge_4Sb_1Te_5$.

The crystallization kinetics of $Ge_2Sb_2Te_5$ have been studied very intensely over the past decade but the data are not in full agreement. Some authors [24, 25, 26] do not observe the early onset of crystallization around $T_c = 101$ ℃, while others do [27]. Yet

Table 3.3: Heat of crystallization ΔH_c, heat of fusion ΔH_f, and entropy of fusion ΔS_f for three Te alloys. The numbers result from measurements at heating rate of 5 K/min.

	ΔH_c (kJ mol^{-1})	ΔH_f (kJ mol^{-1})	$\Delta H_f/\Delta H_c$	ΔS_f (J mol^{-1} K^{-1})	$\Delta S_f/R$
AgInSbTe	4.2 ± 0.3	16.1 ± 0.1	3.8 ± 0.3	19.9 ± 0.2	2.39 ± 0.03
$Ge_4Sb_1Te_5$	4.0 ± 0.1	... [a]	...	...	...
$Ge_2Sb_2Te_5$	0.95 ± 0.30 [b]	14.7 ± 0.7	...	16.5 ± 0.9	1.98 ± 0.11

[a] no data available

[b] Estimate only. This does not include the heat of the cubic-to-hexagonal transformation ΔH_{c-h}.

others [28] observe the early onset, but at a higher temperature. These variations may be the result of slight differences in composition or sample preparation, possibly also a result of sample oxidation. A slight difference in composition is probably the most dominant factor [29].

In order to find out more about these variations, XRD measurements and measurements of the electrical film resistance were carried out using three different samples ($i = 1, 2, 3$) of 1 µm thickness deposited on glass substrates. Except for the film thickness, these samples were prepared under the same sputtering conditions as the samples used for the DSC measurements. Sample i was heated to temperature T_i by 2 K/min and cooled down at the same cooling rate ($T_1 = 107$ ℃, $T_2 = 131$ ℃, $T_3 = 420$ ℃). The electrical resistance was measured simultaneously upon heating and cooling. *Subsequently*, the structure of the film was measured by XRD measurements. The results for the resistance measurements are shown in Fig. 3.6. The curve of sample 3 shows that the film resistance is decreasing by several orders of magnitude upon crystallization between about 140 ℃ and 160 ℃. However, for samples 1 and 2 no indication for crystallization (i. e. no decrease in film resistance) is visible. The resistance evolution is approximately reversible upon heating and cooling, i. e. clear indications of thermal history effects (structural relaxation) are not observed. The XRD measurements yielded an amorphous structure for sample 1 and sample 2 and a hexagonal structure for sample 3. The deviations from the DSC measurements can possibly be explained if the crystalline nuclei are assumed to be *isolated* inside the amorphous random network

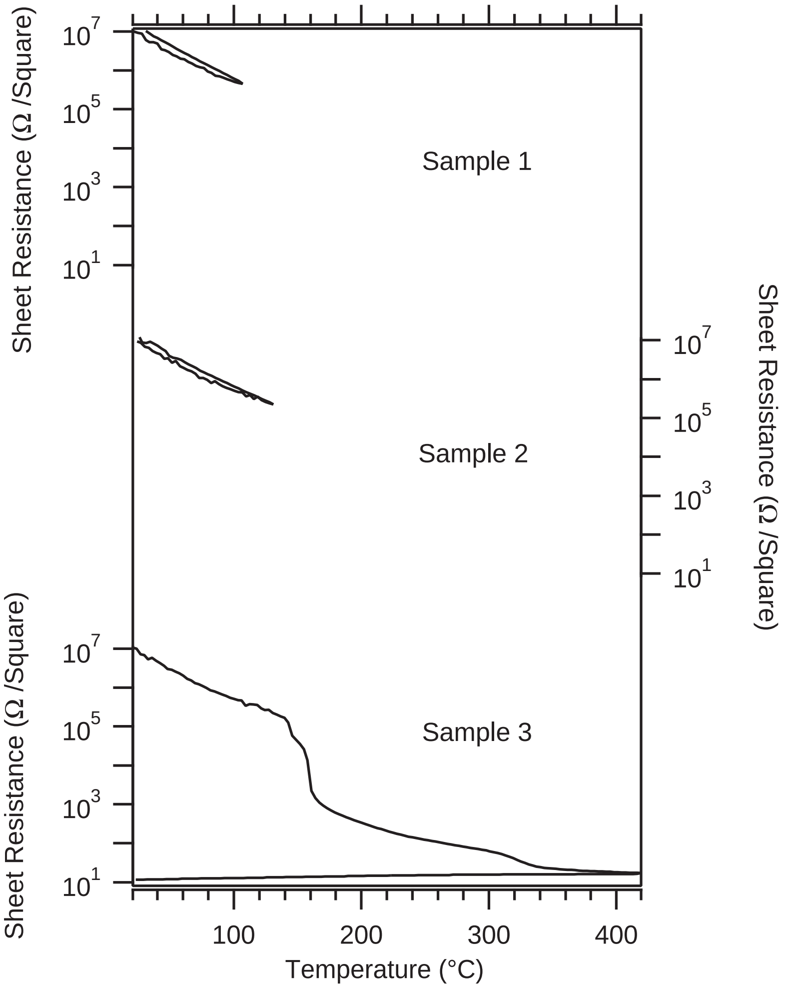

Figure 3.6: Electrical film resistance measurements using a four point probe setup based on *van der Pauw method.*

at temperatures between 100℃ and 140℃. In this case, electrical conductivity would be mainly due to the amorphous phase. Possibly the resolution of the XRD detector was not high enough in order to resolve small nuclei resulting from the early onset of crystallization.

The literature is also not in full agreement concerning the cubic-to-hexagonal transformation: In some studies [24], the phase transition to the hexagonal phase is found around 200℃, whereas in others [14] it is seen around 300℃. This may also be due to slight differences in composition. On the other hand, the values for $T_{c,p}$, T_s, T_m and T_l found in the literature are entirely consistent with those found in this work (Tables 3.1

and 3.2). The heat of fusion was obtained by numerically integrating the endothermic melting peak (Fig. 3.5, Table 3.3). Above 660 ℃ (not shown) the sample fragments reacted with the platinum of the pans. As a result, a large noise was observed in the signal. Due to this reaction, no re-solidification peak was observed upon cooling. However, due to the fact that the reactions started 25 ℃ above the liquidus temperature T_l, the experimentally obtained value for the heat of fusion is not affected by that.

3.2 Entropy of fusion

The entropy of fusion ΔS_f is obtained from Eq. (1.9) and is listed in Table 3.3. For the error propagation, an error in the peak melting temperature T_m of 5 K was assumed. The values were normalized with respect to the gas constant $R = N_A k_B$, where N_A is Avogadro's number. ΔS_f is remarkably large for both AgInSbTe and $Ge_2Sb_2Te_5$ ($2.39R$ and $1.98R$ respectively). For comparison, Fig. 3.7 displays the heat of fusion ΔH_f of all elements from the periodic table of atomic number $Z \leq 88$ as a function of melting temperature T_m. In this graph, the entropy of fusion ΔS_f is obtained from the slope of the line that connects the corresponding data point with the origin. AgInSbTe and $Ge_2Sb_2Te_5$ are marked by a cross. Characteristic for the metallic elements is an entropy of fusion on the order of $\Delta S_f = 10\,\mathrm{J\,mol^{-1}\,K^{-1}} = 1.2R$. Large entropies of fusion are also observed in Si and Ge ($\Delta S_f > 3R$), and are the result of a change in chemical bonding, from covalent to metallic, upon melting. This suggests that the nature of the bonding in the crystalline and the liquid/ amorphous phases of the Te alloys may also be qualitatively different [30]. The large difference in specific heat at the melting point (see Chapter 3.5) points in the same direction. It is interesting to mention that the entropy of fusion of elementary Te is also large ($2.9R$).

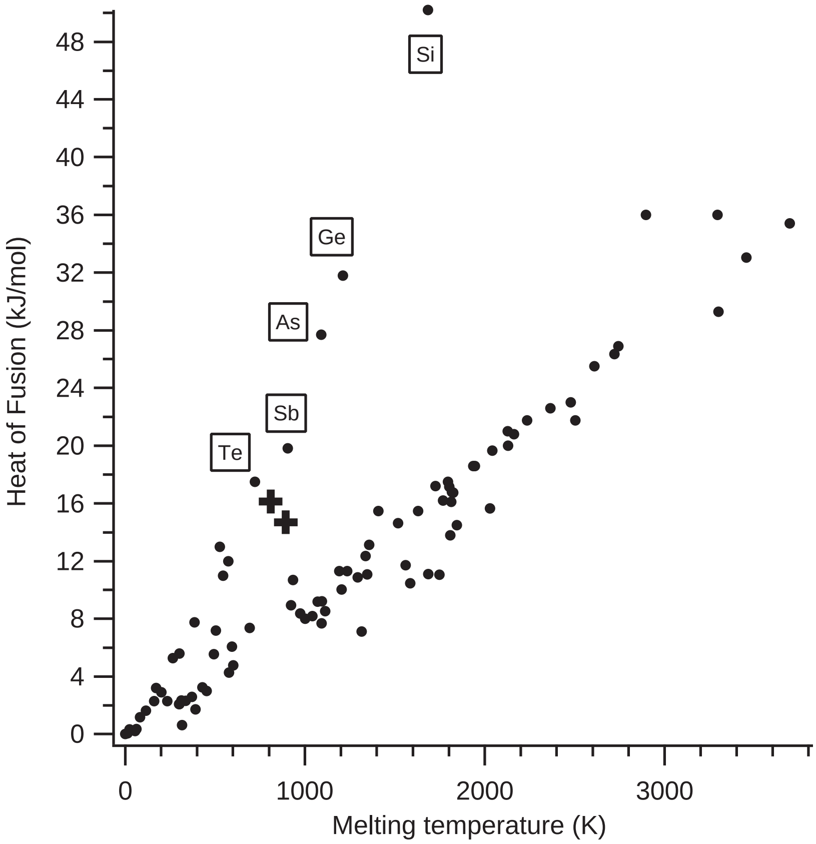

Figure 3.7: Heat of fusion ΔH_f as a function of melting temperature T_m for all elements of the periodic table of atomic number $Z \leq 88$. Due to its high heat of fusion, carbon ($T_m = 3825\,\mathrm{K}$, $\Delta H_f = 117\,\mathrm{kJ\,mol^{-1}}$) is not indicated. The crosses indicate AgInSbTe and $Ge_2Sb_2Te_5$.

3.3 Glass transition

In Figs. 3.1, 3.3 and 3.4 no thermal signal of a glass transition can be observed[3] for $T < T_c$: According to Fig. 1.2 the derivative of the enthalpy

$$\frac{\partial H}{\partial T} = \frac{1}{\dot{T}} \dot{H}$$

exhibits a discontinuity at T_g. Therefore, an endothermic step is expected in the DSC signal when the amorphous sample is heated over the glass transition into the regime of the undercooled liquid (if crystallization can be avoided). Hence, it can be concluded that the glass transition temperature T_g is not below the onset of crystallization T_c for all three alloys at heating rates of 5 K/min. However, according to Fig. 1.5, the endothermic step in $\dot{H}$ would be much more pronounced at higher heating rates. Therefore, it is sometimes possible to reveal T_g by increasing the heating rate. Therefore, all DSC scans were also performed at heating rates of 80 K/min. For AgInSbTe and $Ge_4Sb_1Te_5$ the crystallization peak shifted to higher temperatures (Table 3.1) but still no glass transition was observed below T_c for both alloys. These curves are not shown here as they look qualitatively very similar to Figs. 3.1 and 3.3, i. e. there are sharp peaks in both cases. Figure 3.8 shows the result for $Ge_2Sb_2Te_5$. The high heating rate also shifts T_c and $T_{c,p}$ to higher temperatures for this alloy, but the early onset of crystallization is not that pronounced any more. Comparing the entire curve to the re-scan of the already crystallized sample (dashed) reveals the shape of the exothermic crystallization peak. Again, no glass transition can be observed below $T_c \approx 150$ °C. Therefore, it can be concluded that T_g is not below T_c for heating rates between 5 K/min and 80 K/min for all three alloys. Hence, T_g can be estimated to be close to the crystallization temperature. This is appropriate, as these two temperatures usually do not differ significantly: Around T_g the temperature dependence of the diffusivity D is very strong (large equilibrium activation energy for the viscosity and the diffusivity) [Fig. 4.3, Eq. (8.7)]. If crystallization occurs diffusion limited[4], the crystallization temperature upon heating is (among other things) determined by the point at which the diffusivity becomes sufficiently large.

---

[3] These figures just show a zoom around the crystallization peak, but also for lower temperatures up to room temperature the glass transition could not be observed.

[4] see Chapter 9

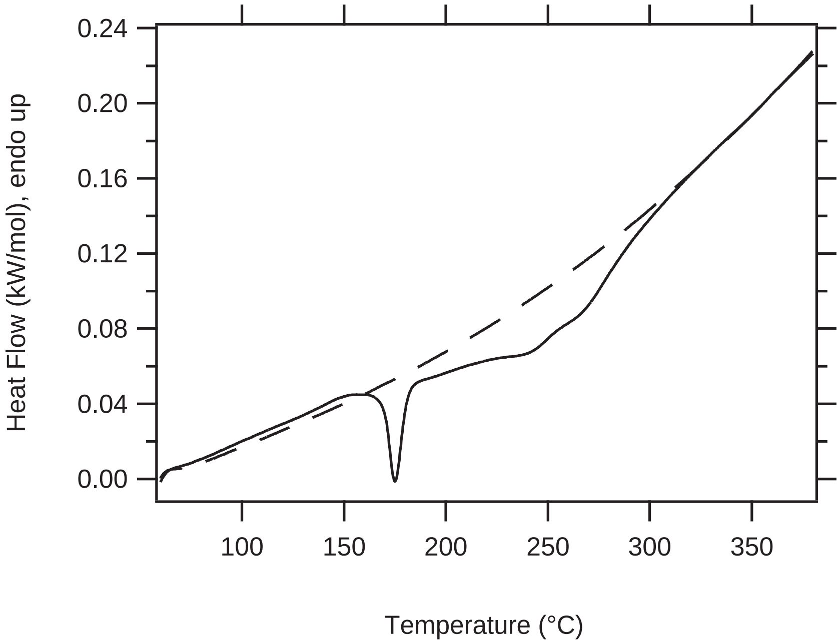

Figure 3.8: Solid: Heat flow $\dot{H}$ as a function of temperature for initially amorphous $Ge_2Sb_2Te_5$ (heating rate: 80 K/min). Dashed: Signal upon rerun (same heating rate). Sample pan material: Al.

Table 3.2 shows that the reduced glass transition temperature $T_{rg} = T_g/T_l$ is very low for all alloys, which categorizes them as *marginal glass formers* (see Chapter 1.1)[5]. It is this property that makes these materials so useful for *fast* phase change recording: As a consequence, the maximum crystal nucleation frequency and the maximum crystal growth velocity is high in the regime of the undercooled liquid[6]. This enables a *fast* recrystallization of amorphous marks. Interestingly, the time required for recrystallization of amorphous marks is larger for AgInSbTe than for $Ge_4Sb_1Te_5$ and $Ge_2Sb_2Te_5$ [14, 31]. This can be attributed to the slightly higher value of T_{rg} for AgInSbTe.

---

[5] In order to calculate T_{rg}, T_g was estimated by the peak crystallization temperature at heating rates of 80 K/min ($T_{c,p}^{(80)}$), as the heating rate dependence of the glass transition is often lower than the heating rate dependence of the crystallization temperature [30]. If T_g was estimated by $T_{c,p}^{(5)}$, T_{rg} would be even lower.

[6] see Appendix A

Table 3.4: Activation energy for crystallization E_A determined from Fig. 3.9. Literature values are given for comparison.

	$E_A^{(\mathrm{DSC})}$ (eV)	$E_A^{(\mathrm{lit.})}$ [a] (eV)
AgInSbTe	3.11 ± 0.16	3.03 ± 0.17
$Ge_4Sb_1Te_5$	3.83 ± 0.31	3.48 ± 0.12
$Ge_2Sb_2Te_5$	2.46 ± 0.14	2.24 ± 0.11

[a] from Refs. [19, 33, 26, 34, 13, 24]

3.4 Activation energy for crystallization

Delayed crystallization at higher heating rates (Table 3.1) is due to the fact that crystallization is a thermally activated activated process. Therefore, it is a function of *both* temperature *and* time. For $\dot{T} =$ const, the heating rate dependence of the crystallization temperature $T_{c,p}$ is given by the *Kissinger equation* [32]:

$$\boxed{\frac{\dot{T}}{T_{c,p}^2} = C \cdot \exp(-\frac{E_A}{k_B T_{c,p}})} \qquad (3.2)$$

where E_A is the *effective activation energy for crystallization* and C is a constant. E_A was determined by plotting $\ln(\dot{T}/T_{c,p}^2)$ versus $1/T_{c,p}$. The straight lines in Fig. 3.9 exhibit a slope of $-E_A/k_B$. The results for E_A are listed in Table 3.4. Within the range of error, they agree with results found in several studies [19, 33, 26, 34, 13, 24], though they are slightly higher. Apart from the reduced amount of data points, this discrepancy could also result from a slightly temperature dependent activation energy: the literature values result from measurements at heating rates lower than 10 K/min.

$Ge_4Sb_1Te_5$ exhibits the highest activation energy E_A. It is therefore most stable against crystallization. The facts that its crystallization temperature is highest (Table 3.1) points in the same direction. $Ge_2Sb_2Te_5$ is the least stable against crystallization: it exhibits the lowest activation energy and the lowest crystallization temperature.

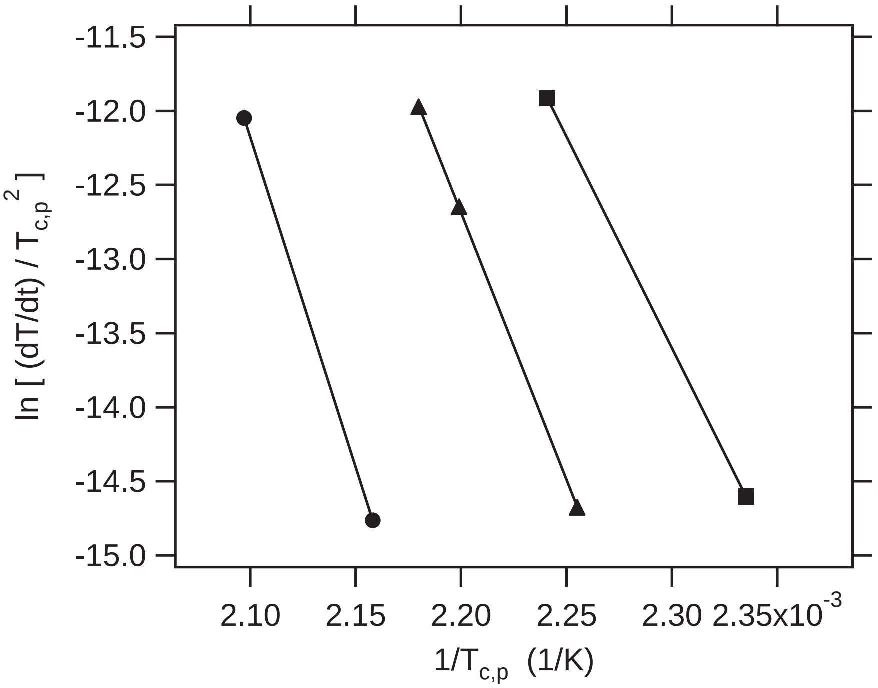

Figure 3.9: Kissinger plot from which the activation energy E_A of the amorphous to crystalline transformation at $T_{c,p}$ is determined (for $Ge_2Sb_2Te_5$: amorphous to *cubic state* transformation). Triangles: AgInSbTe; circles: $Ge_4Sb_1Te_5$; squares: $Ge_2Sb_2Te_5$.

3.5 Heat capacity measurements

The heat capacity of the Te alloys was measured applying the following technique: Holding a sample at a constant temperature T_0 and then suddenly heating it with a constant heating rate $\dot{T} > 0$ results in a step in heat flow $\Delta\dot{H}$ given by

$$\Delta\dot{H} \equiv \dot{H}_{\dot{T}>0} - \dot{H}_{T=T_0} = C_p(T_0) \cdot \dot{T}. \tag{3.3}$$

The quantity $\dot{H}_{T=T_0}$ has to be subtracted out because the device is only able to measure $\dot{H}$ with respect to an unknown baseline. If the sequence described in Eq. (3.3) is repeated several times at different temperatures, it is possible to measure the heat capacity $C_p(T)$ of the sample fragments as a function of temperature. An example curve for AgInSbTe is shown in Fig. 3.10 for $T \leq 300\,^{\circ}\mathrm{C}$. Measurements for the other two alloys look qualitatively similar.

Figures 3.11–3.13 display the molar heat capacity as a function of temperature. In all three figures, the data below 200 °C were measured for the *crystalline* (and not for the *amorphous*) state. For all alloys, the heat capacity of the crystalline state is larger than the classical Dulong-Petit value of $C_p = 3R = 3N_A k_B$, most likely as a result of the excitation of chemical disorder or point defects. The data in the crystalline state were approximated by using a polynomial fitting function of second order.

Due to the relatively low melting temperature of AgInSbTe (Table 3.2), the heat capacity C_p of the *liquid* could be measured above the liquidus temperature T_l of this alloy. The difference in heat capacity between the liquid and the crystal at the melting temperature $\Delta C_{p,lc}(T_m)$ is rather large. The data in the liquid state were extrapolated linearly into the regime of the undercooled liquid where no direct experimental data exist (Fig. 3.11). This extrapolation was performed under three constraints:

1. The fit to the liquid specific heat data had to remain within the error bars of the measurements.
2. The integral

$$\Delta H_{lc}(T) = H_l(T) - H_c(T) = \Delta H_f + \int_{T_m}^{T} \Delta C_{p,lc}(T')dT'$$

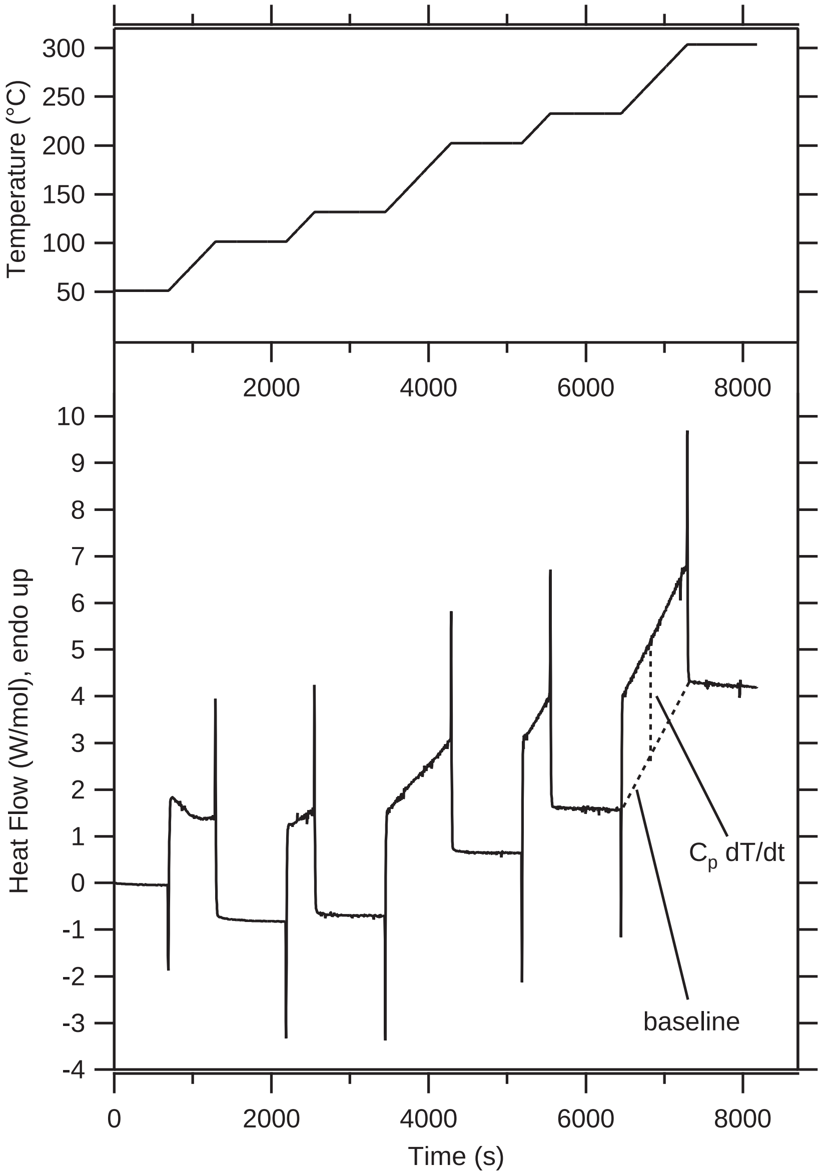

Figure 3.10: Heat capacity measurement for AgInSbTe. A temperature dependent baseline has to be subtracted out. The data correspond entirely to the *crystalline* state, i. e. the sample was heated above the crystallization temperature before the start of the measurement. $\dot{T} = 5\,\mathrm{K/min}$ for all heating intervals. Sample pan material: Al.

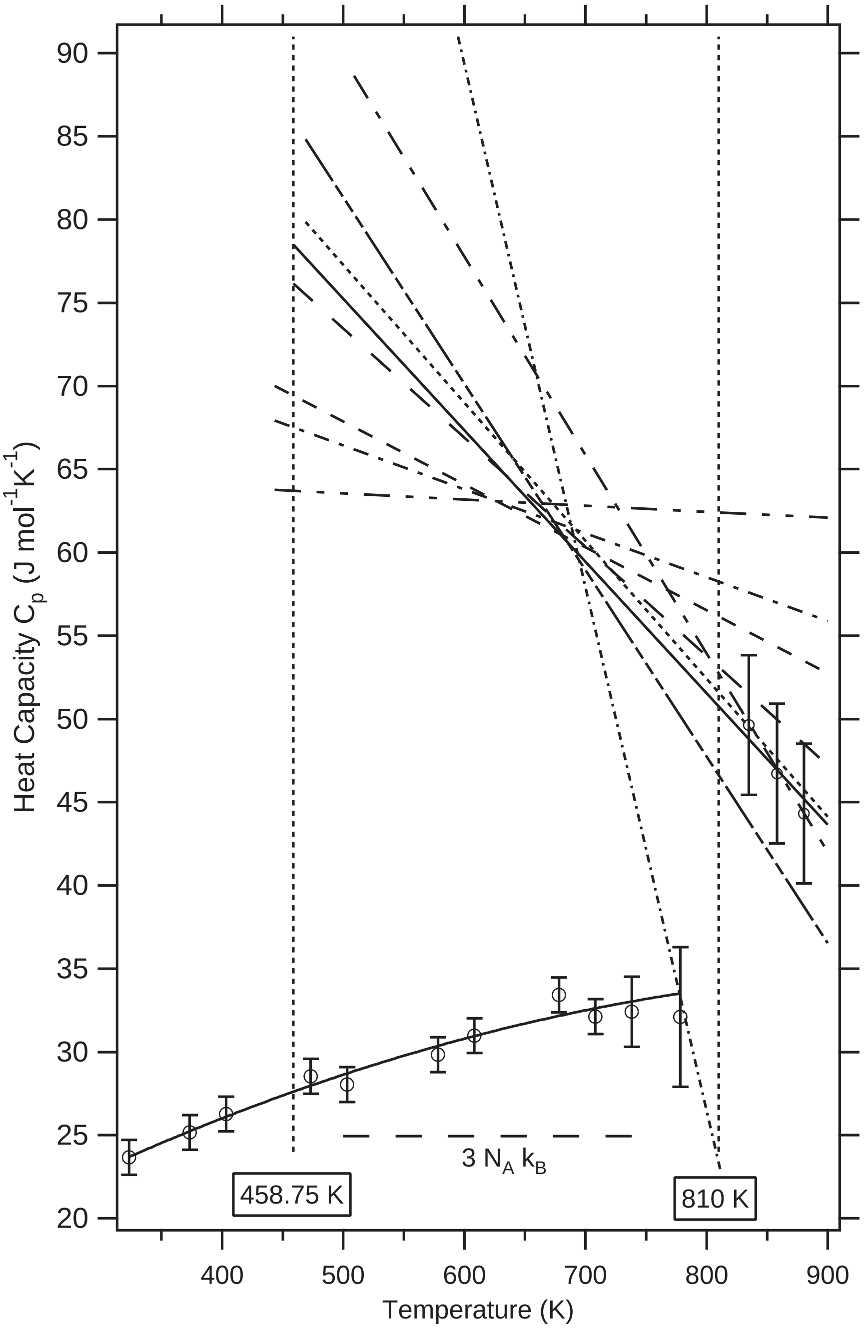

Figure 3.11: Molar heat capacity for AgInSbTe. The extrapolation lines into the regime of the undercooled liquid are based on values for T_g and T_k given in Table 3.5 and on constraints discussed in the text.

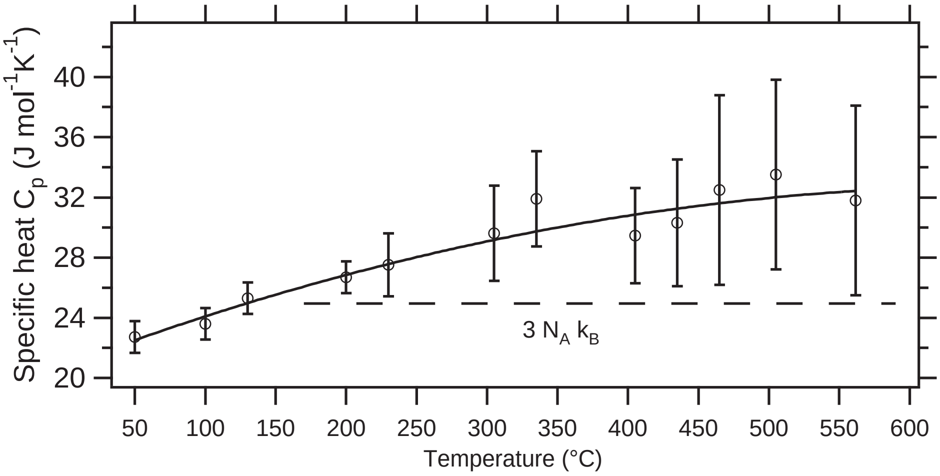

Figure 3.12: Molar heat capacity for $Ge_4Sb_1Te_5$.

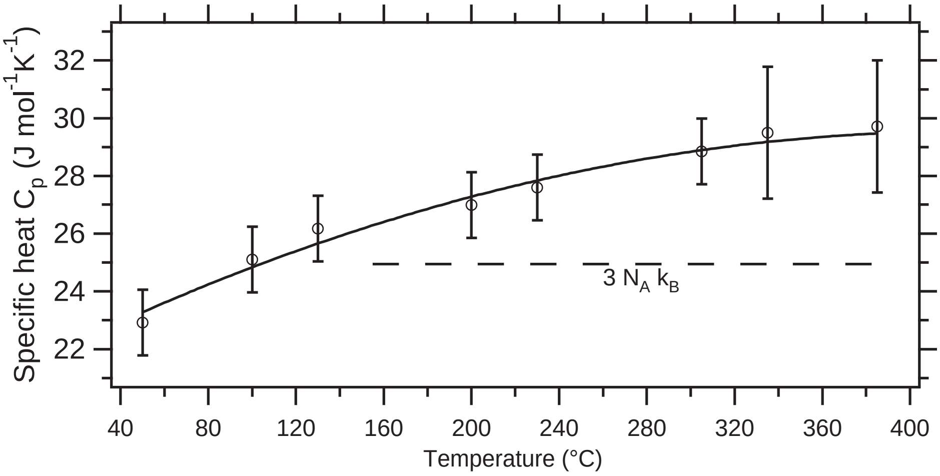

Figure 3.13: Molar heat capacity for $Ge_2Sb_2Te_5$.

[Eq. (1.2)] had to adopt a value of $\Delta H_{lc}(T_g) = \Delta H_c = 4.2\,\mathrm{kJ\,mol^{-1}}$ (Table 3.3) at the glass transition temperature[7]. The *peak* temperature in the melting signal $T_m = 537\,°\mathrm{C} = 810\,\mathrm{K}$ (Table 3.2) was chosen for the lower boundary of this integral.

3. The integral

$$\Delta S_{lc}(T) = S_l(T) - S_c(T) = \Delta S_f + \int_{T_m}^{T} \frac{\Delta C_{p,lc}(T')}{T'} dT'$$

[Eq. (1.5)] had to become zero at the Kauzmann temperature T_k (see Chapter 1.3): $\Delta S_{lc}(T_k) = 0$, slightly below the glass transition temperature.

Although the Kauzmann temperature T_k and the glass transition temperature T_g are not known, the range of choices is fortunately quite limited. The fits displayed in Fig. 3.11 are based on values for T_k and T_g given in Table 3.5. Line 1 and 2 assume a glass transition temperature equal to the peak crystallization temperature measured at heating rate of 80 K/min: $T_g = T_{c,p}^{(80)} = 185.6°\mathrm{C} = 458.75\,\mathrm{K}$ (Table 3.1). Line 1 fits the heat capacity data very well. However, T_k is expected to be *below* T_g (see Chapter 1.3). Line 2 assumes the lowest value for T_k allowed by the error bars of the liquid heat capacity at the same value for T_g. This results in a difference of 1.19 K between T_g and T_k, which is still rather small. However, due to the fact that T_g could be slightly higher than $T_{c,p}^{(80)}$, the fit of line 2 is still of good quality. Lines 3 and 4 assume a value for T_g, which is 10 K higher than $T_{c,p}^{(80)}$. Line 4 fits the data very well; and line 3 ($T_k = T_g$) results in a fit, which is just outside the error bars of the liquid heat capacity. Lines 5 and 6 assume T_g to be 50 K above the measured value for $T_{c,p}^{(80)}$. The fit of line 5 is very poor, but line 6 fits the data very well. Lines 7, 8 and 9 assume $T_g = T_{c,p}^{(5)} = 170.3°\mathrm{C} = 443.45\,\mathrm{K}$ and are all poor fits as they do not remain within the error bars of the measurement. In summary, the fits of lines 1 and 2 exhibit the best resemblance with the measured data, as lines 3, 4, 5 and 6 assume values for T_g, which differ too much from the crystallization temperature: As already discussed in

---

[7] Due to the fact that the glass transition temperature T_g was *not* observed below the crystallization temperature T_c (Chapter 3.3), the difference in enthalpy between the amorphous and crystalline phase is approximately equal at T_g and at T_c: $H_{lc}(T_g) = H_{lc}(T_c)$ (see Fig. 1.2).

Table 3.5: Various values assumed for the glass transition temperature T_g and the Kauzmann temperature T_k for AgInSbTe. The fits shown in Figs. 3.11, 3.15, 3.16 and 3.17 are based on these assumptions. The numbers of the lines are assigned to their appearance in Fig. 3.14.

Line number	T_g (K)	T_k (K)	$T_g - T_k$ (K)
Line 1	458.75	458.75	0.00
Line 2	458.75	457.56	1.19
Line 3	468.75	468.75	0.00
Line 4	468.75	466.54	2.21
Line 5	508.75	508.75	0.00
Line 6	508.75	499.94	8.81
Line 7	443.45	443.45	0.00
Line 8	443.45	442.08	1.37
Line 9	443.45	438.92	4.53

Chapter 3.3, T_g is usually not much higher than $T_{c,p}$. Therefore, the choices for T_g and T_k are limited. This also underlines the choice of the value for $T_g = T_{c,p}^{(80)}$ in Table 3.2.

Figures 3.15, 3.16 and 3.17 display respectively the temperature dependence of the difference in enthalpy, entropy and Gibbs free energy calculated from the fits to the liquid specific heat. Fortunately, the fits do not differ significantly from each other except for the lowest temperatures. Only line 5 misbehaves, but this is due to its unsatisfactory fit to the heat capacity data. The difference in Gibbs free energy was calculated from Eq. (1.11) and may be useful in future calculations of the crystal nucleation frequency [Eq. (8.8)] or the crystal growth velocity [Eq. (8.10)].

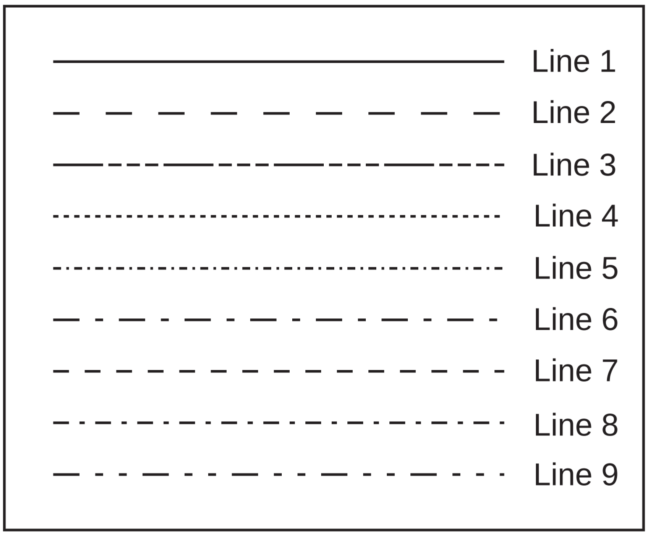

Figure 3.14: Legend for the fits in Figs. 3.11, 3.15, 3.16 and 3.17. The fits are defined in Table 3.5.

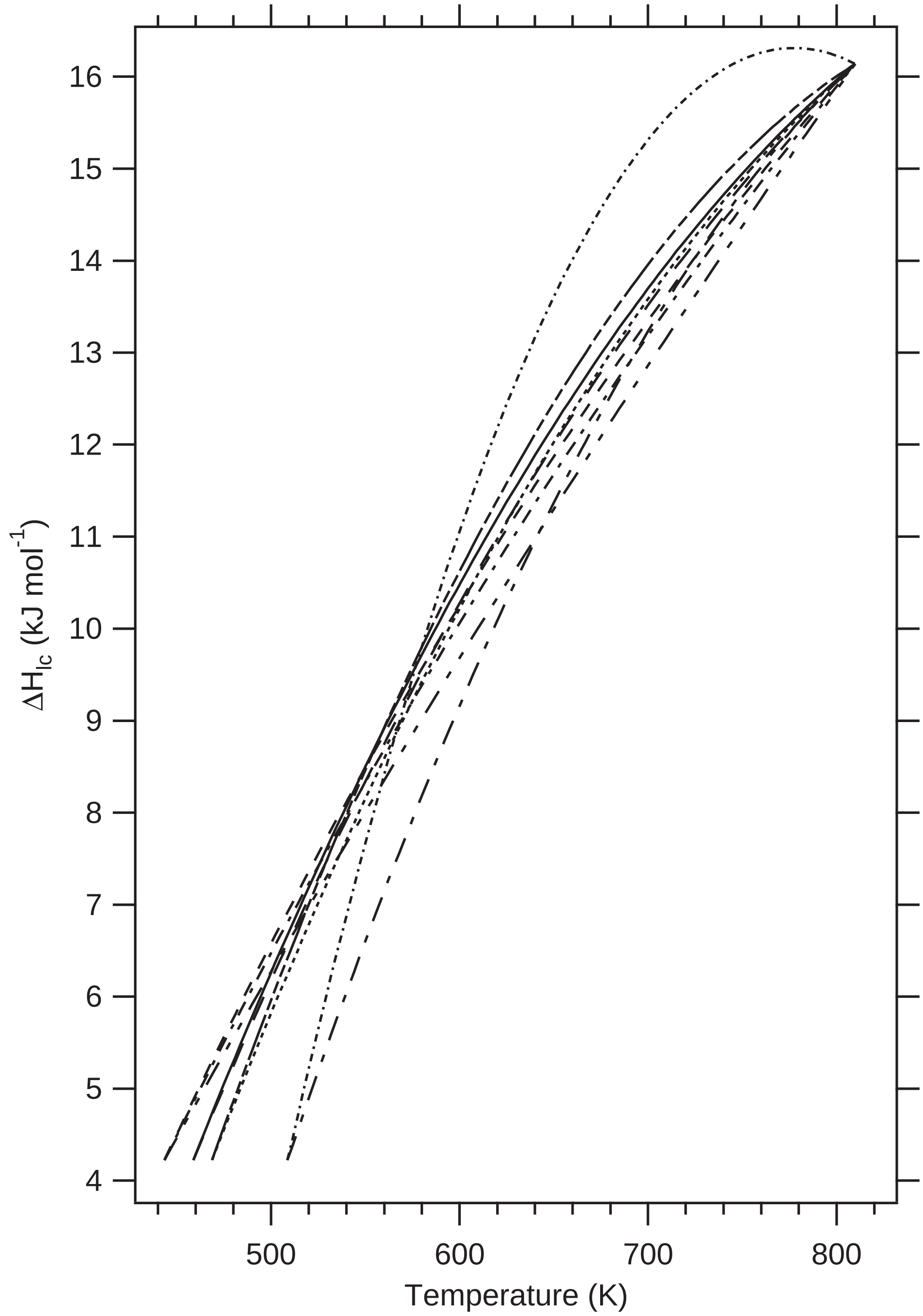

Figure 3.15: Calculation of the difference in molar enthalpy ΔH_{lc} between the undercooled liquid and the crystalline phase of AgInSbTe, based on the fits to the liquid specific heat shown in Fig. 3.11.

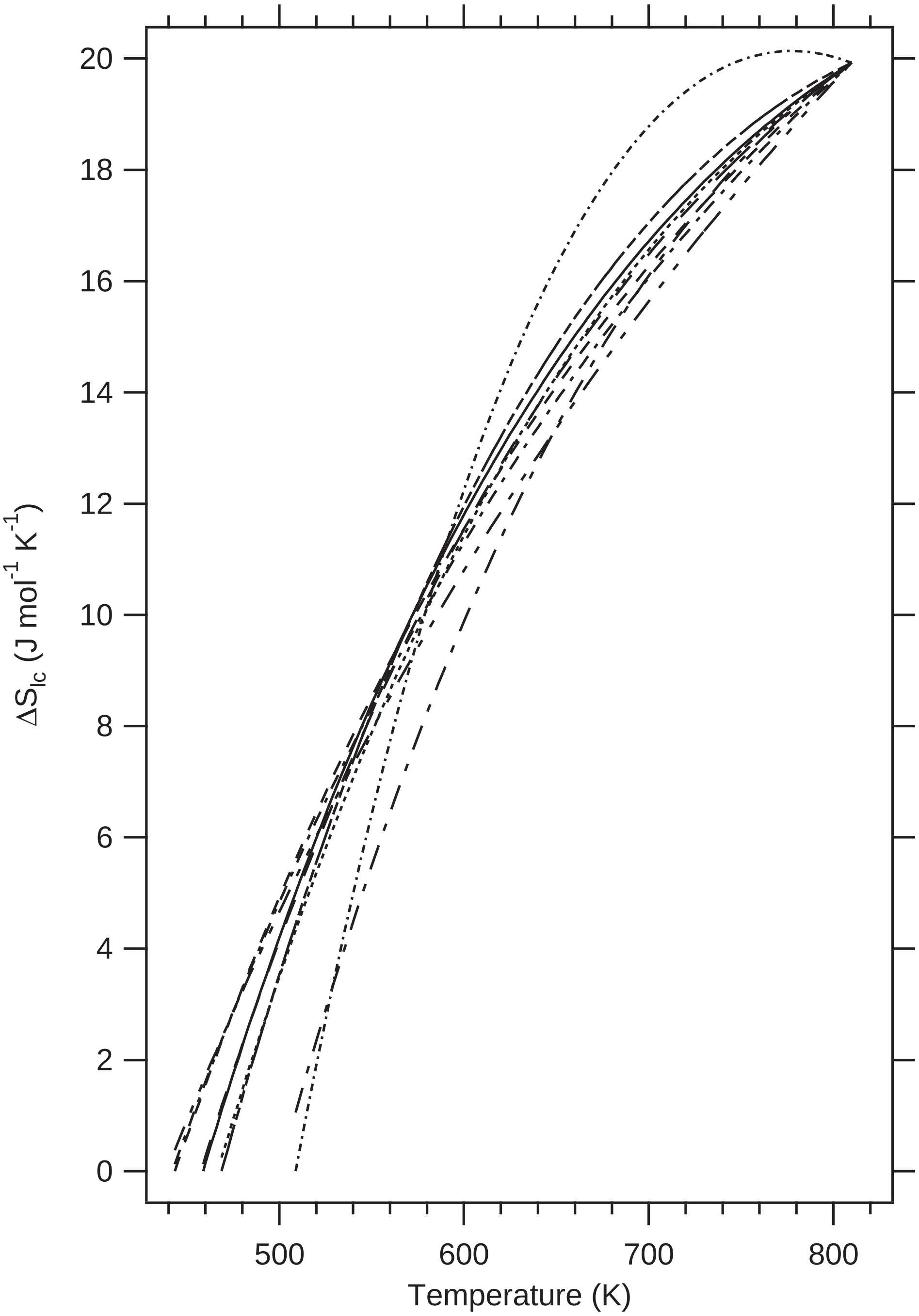

Figure 3.16: Calculation of the difference in molar entropy ΔS_{lc} between the undercooled liquid and the crystalline phase of AgInSbTe, based on the fits to the liquid specific heat shown in Fig. 3.11.

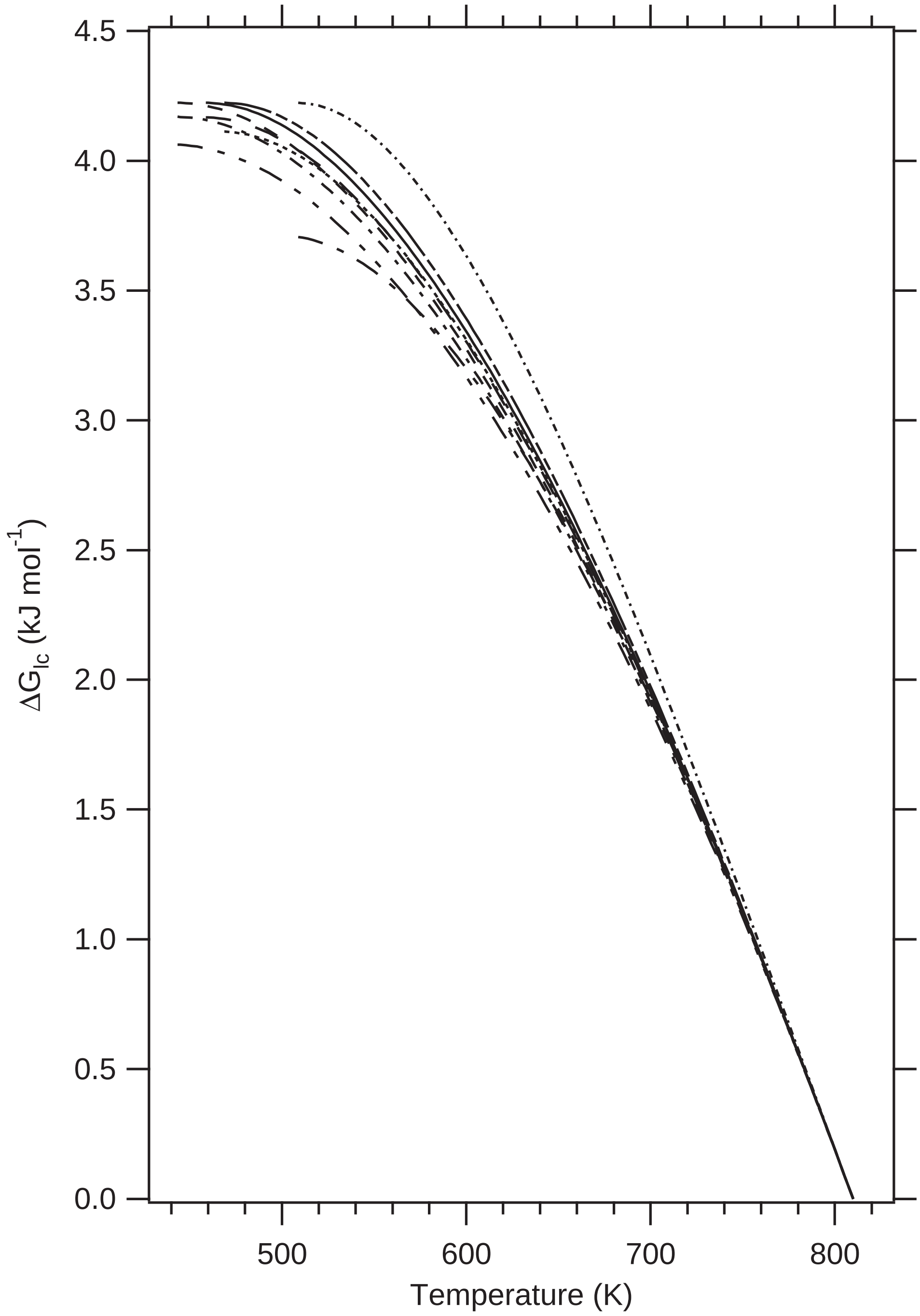

Figure 3.17: Calculation of the difference in molar Gibbs free energy ΔG_{lc} between the undercooled liquid and the crystalline phase of AgInSbTe, based on the fits to the liquid specific heat shown in Fig. 3.11.

Conclusions Part I

1. The entropy of fusion ΔS_f of AgInSbTe and $Ge_2Sb_2Te_5$ is large, indicating a qualitative change in bond type between the crystalline and the liquid/amorphous phases.
2. The melting point, the crystallization temperature, and the heat of crystallization of the three Te alloys were determined. The crystallization temperature is lowest for $Ge_2Sb_2Te_5$ and the melting point is lowest for AgInSbTe.
3. Amorphous AgInSbTe and $Ge_4Sb_1Te_5$ crystallize over a small temperature range to a single phase, which is stable up to the solidus temperature T_s. The crystallization of $Ge_2Sb_2Te_5$ is followed by a phase transformation in the crystalline state, which causes overlap between the thermal signals of the two processes.
4. The activation energy for crystallization E_A was determined from the measurement of the crystallization temperature as a function of heating rate. $Ge_2Sb_2Te_5$ was found to exhibit the lowest activation energy.
5. No thermal signal of a glass transition was observed below the crystallization temperatures at heating rates between 5 K/min and 80 K/min.
6. The ratio of the estimated glass transition temperature T_g to the liquidus temperature T_l is around 0.5. These alloys can therefore be classified as marginal glass formers.
7. The difference in specific heat, enthalpy, entropy and Gibbs free energy between liquid and crystalline AgInSbTe was estimated based on specific heat measurements on the crystalline (below the melting point) and liquid phases (above the melting point).

Part II

Mechanical analysis of thin amorphous chalcogenide films used for optical data storage

Chapter 4

Theoretical background

4.1 Mechanical deformation of matter

When a force F is applied to a body, it generally undergoes a deformation. If the body is stretched by *equal* and *opposite* tensile and axial forces F (Fig. 4.1a), the deformation is called the *axial strain* ϵ, which is defined as the ratio of change in length Δl and the original length l_0. The body is in a state of *stress*, which is defined as the applied force per unit surface A, on which the force acts. The deformation is said to be *elastic* if the body changes back to its original shape when the force is removed. On the other hand, if the body *permanently* changes its shape (i. e. if the body does *not* change back to its original shape after removing the force), the body was deformed *plastically.*

In order to sustain mechanical equilibrium, *internal* stresses must act on an arbitrary plane, which is revealed by a section through the body (Fig. 4.1b). The internal stress can be thought to be divided in a normal component σ_n and an in-plane component τ. The latter is called the *shear stress*[1].

Fig. 4.2 shows the effect of the application of a shear stress τ to a body. The body is distorted by a *shear strain* γ, which is defined as the ratio of Δx and thickness d.

---

[1] For a more detailed definition of stress and strain in terms of second rank tensors see Chapter 5.2.

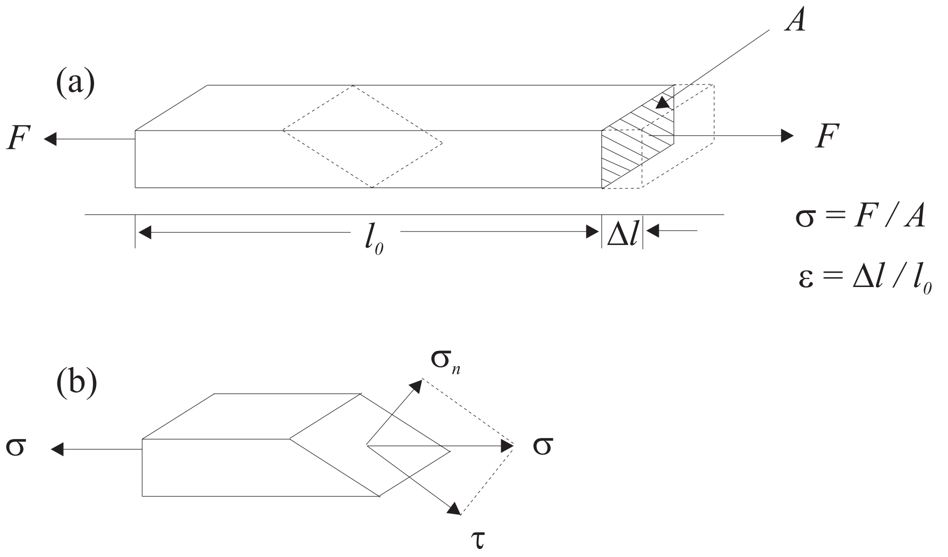

Figure 4.1: Matter in a state of stress. (a) Tensile axial force F applied to a body inducing a strain ϵ. (b) Arbitrary section revealing the normal component of the stress σ_n and the shear stress τ.

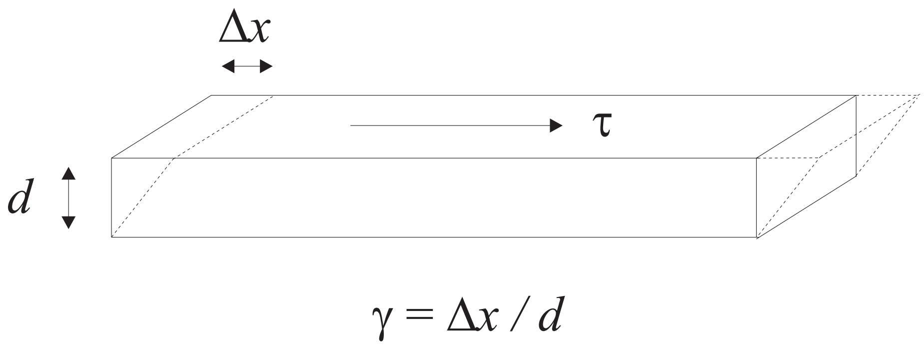

Figure 4.2: Distortion of a body due to a shear stress τ.

4.2 The shear viscosity

A quantitative measure of the 'hardness' of a liquid or an amorphous solid is the *shear viscosity* η (hereafter viscosity). It is defined as the resistance to an applied shear stress τ causing a body to flow plastically by a shear strain rate $\dot{\gamma}$ and permanently change its shape [35]:

$$\boxed{\tau = \eta \cdot \dot{\gamma}}. \tag{4.1}$$

Figure 4.3 qualitatively shows the temperature dependence of the viscosity η for a liquid. If the liquid is cooled below the melting temperature T_m, the viscosity increases *discontinuously* by several orders of magnitude in case of crystallization. If crystallization can be avoided, the liquid is being undercooled and its viscosity rises quickly but *continuously.* The temperature dependence of the viscosity in the regime of the liquid and the undercooled liquid can in general be approximated by the *Fulcher-Vogel-Equation* [36, 37, 4]:

$$\boxed{\eta_{eq}(T) = \eta_0 \cdot \exp\left(\frac{A}{T - T_0}\right)}, \tag{4.2}$$

where η_0 and A are constants. The temperature T_0 is close to the *Kauzmann temperature* T_k defined in Chapter 1.3: When perfect order in the undercooled liquid occurs, viscous flow is impossible due to the absence of flow defects (see Chapter 4.3). Therefore the viscosity must go to infinity around T_k.

Upon undercooling, the liquid remains in internal equilibrium up to the glass transition temperature T_g. It is configurationally frozen here and the viscosity rises less quickly upon further cooling (Fig. 4.3) [38, 39]. Figure 4.3 shows two different isoconfigurational states [(a) fast cooling, (b) slow cooling]. Due to structural relaxation, which is indicated by the arrows, the viscosity increases with time continuously below T_g: the glass tries to approach its equilibrium structure (c), which would be obtained by cooling infinitively slowly. Overheating a glass quickly above the glass transition temperature (Fig. 4.3) results in a *decrease* of the viscosity with time due to structural relaxation.

Most undercooled liquids undergo their glass transition when their viscosity approaches a value on the order of $10^{12}\,\mathrm{Pa\,s}$ [1]. According to Eq. (4.1) a body with a viscosity of that order exhibits less than 1% strain upon the application of a stress of 100 kPa for 1 day. At sufficiently low temperatures ($T \ll T_g$), glasses seem to show

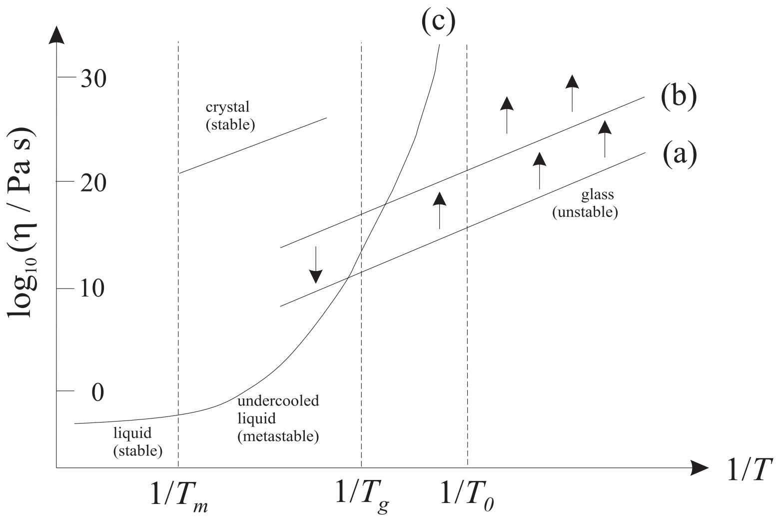

Figure 4.3: Viscosity η in various stability regimes: stable equilibrium above T_m, metastable equilibrium below T_m and instable isoconfigurational states below T_g. (a) Fast cooling. (b) Slow cooling. (c) Cooling infinitively slowly (equilibrium). Curve (c) is described by the Fulcher-Vogel-Equation (4.2).

no apparent permanent change in their shape any more on experimental time scales. Macroscopically, they are solid. However, at elevated temperatures below T_g, the glass is able to flow within experimental time scales and the viscosity can be measured by stress relaxation experiments.

For comparison, literature viscosity values of some liquids at 30 ℃ are: water, $8.0 \cdot 10^{-4}$ Pa s; glycerin, $6.3 \cdot 10^{-3}$ Pa s; glucose, $6.6 \cdot 10^{10}$ Pa s [40].

4.3 Models for viscous flow

Viscous flow in glasses is attributed to irreversible *shear rearrangements*, which occur at specific sites or *flow defects* of concentration n_f [41, 42, 39, 43, 44]. In *metallic* glasses, these flow defects are assumed to be *free volume fluctuations* [2, 45, 46, 4] and in *covalently* bonded glasses *dangling bonds* [47, 48]. Upon the application of a shear stress τ [Fig. 4.2, Eq. (4.1)], the induced macroscopic shear strain rate $\dot{\gamma}$ is given by [44, 7]

$$\dot{\gamma} = \omega_f \cdot \gamma_0 \cdot \nu_0 \cdot n_f. \tag{4.3}$$

ν_0 is the rearranging volume, γ_0 is the total shear strain of the rearrangement and ω_f is the net jump frequency for the thermally activated microscopic shear rearrangement. Rate theory yields [44]

$$\omega_f = k_f \cdot \sinh\left(\frac{\gamma_0 \cdot \nu_0 \cdot \tau}{k_B T}\right). \tag{4.4}$$

k_B is Boltzmann's constant and k_f the *rearrangement frequency*, which is the rate at which the rearrangement occurs at $\tau = 0$. k_f is assumed to be thermally activated:

$$k_f = k_f^0 \cdot \exp\left(-\frac{Q_{iso}}{k_B T}\right), \tag{4.5}$$

where k_f^0 is called the *attempt frequency* and Q_{iso} the *isoconfigurational activation energy*. Therefore,

$$\dot{\gamma} = k_f \cdot \gamma_0 \cdot \nu_0 \cdot n_f \cdot \sinh\left(\frac{\gamma_0 \cdot \nu_0 \cdot \tau}{k_B T}\right). \tag{4.6}$$

For a small shear stress τ a Taylor approximation yields

$$\sinh\left(\frac{\gamma_0 \cdot \nu_0 \cdot \tau}{k_B T}\right) \approx \frac{\gamma_0 \cdot \nu_0 \cdot \tau}{k_B T}, \tag{4.7}$$

and by comparison with Eq. (4.1):

$$\eta = \frac{k_B T}{(\gamma_0 \cdot \nu_0)^2 \cdot k_f \cdot n_f}. \tag{4.8}$$

Therefore, for a small shear stress τ the viscosity η is stress independent. In this regime, viscous flow is commonly said to be *Newtonian*. Each isoconfigurational path in Fig. 4.3 can be assigned a specific *constant* flow defect concentration n_f . The temperature dependence of η in these paths is therefore Arrhenius:

$$\boxed{\eta = \frac{k_B T}{(\gamma_0 \cdot \nu_0)^2 \cdot k_f^0 \cdot n_f} \cdot \exp\left(\frac{Q_{iso}}{k_B T}\right)}; \tag{4.9}$$

the slope of each isoconfigurational path in Fig. 4.3 is therefore equal to Q_{iso}/k_B.

4.4 Models for structural relaxation

A flow defect concentration that *decreases* with time can account for the *increase* of the viscosity with time for $T < T_g$ [Eq. (4.9)]. For $T =$const, three simple relaxation models have been proposed [42, 39, 7, 44, 47, 35, 41, 48]:

$$\dot{n}_f = -k_{r,1} \cdot (n_f - n_{eq}) \tag{4.10a}$$

$$\dot{n}_f = -k_{r,2} \cdot (n_f - n_{eq})^2 \tag{4.10b}$$

$$\dot{n}_f = -k_{r,3} \cdot n_f (n_f - n_{eq}) \tag{4.10c}$$

k_r is called the *rate equation constant* and is assumed to be thermally activated:

$$k_r = k_r^0 \cdot \exp\left(-\frac{Q_{rel}}{k_B T}\right) \tag{4.11}$$

Eqs. (4.10a)–(4.10c) predict $\dot{n}_f = 0$ if $n_f = n_{eq}$, where $n_{eq} \equiv n_{f,eq}$ is the defect concentration of the equilibrium structure at the corresponding temperature. Quadratic terms in n_f describe *flow defect annihilation* by the interaction of *two* defects. In metallic glasses, this was interpreted by the recombination of two free volume fluctuations [2]. In covalently bonded glasses, this was interpreted by the recombination of two dangling bonds [48, 47]. First order terms in n_f describe annihilation of defects at the site of a *single* defect. Therefore, Eq. (4.10a) is said to be based on *unimolecular* and Eq. (4.10b) on *bimolecular* relaxation kinetics. Equation (4.10c) assumes 'intermediate' kinetics.

For structural relaxation far below the glass transition temperature T_g, i. e. far away from equilibrium, the flow defect concentration n_f is in general several orders of magnitude higher than the equilibrium concentration n_{eq}. Therefore,

$$(n_f - n_{eq}) \approx n_f. \tag{4.12}$$

In this approximation unimolecular relaxation kinetics are described by

$$\dot{n}_f = -k_{r,1} \cdot n_f \tag{4.13a}$$

and bimolecular relaxation kinetics by

$$\dot{n}_f = -k_{r,2} \cdot n_f^2. \tag{4.13b}$$

The solutions of Eqs. (4.13a) and (4.13b) are respectively

$$n_f(t) = n_0 \cdot \exp(-k_r t) \tag{4.14a}$$

and

$$n_f(t) = \frac{n_0}{1 + n_0 k_r t}. \tag{4.14b}$$

$n_0 \equiv n_{f,0}$ is the flow defect concentration at $t = 0$. In order to obtain an analytical expression for the viscosity η as a function of time for $T =$const, the following relation is used, which is obtained from Eq. (4.9):

$$n_f(t) \cdot \eta(t) = n_0 \cdot \eta_0 \qquad (T = \text{const}). \tag{4.15}$$

η_0 is the viscosity at $t = 0$. Therefore, far away from metastable equilibrium, the viscosity is described by

$$\eta(t) = \eta_0 \cdot \exp(k_r t) \tag{4.16a}$$

in the unimolecular model and

$$\eta(t) = \eta_0 + n_0 \eta_0 k_r t = \eta_0 + kt \tag{4.16b}$$

in the bimolecular model, where

$$k := n_0 \eta_0 k_r = \text{const} \tag{4.17}$$

is defined for convenience. The unimolecular model yields a viscosity that increases *exponentially* with time and the bimolecular model one that increases *linearly* with time, $\dot{\eta} = k$.

However, for structural relaxation close to the glass transition temperature T_g, the flow defect concentration n is on the order of n_{eq}. Therefore, n_{eq} can no longer be neglected. The solutions of Eqs. (4.10a)–(4.10c) are then respectively

$$\begin{aligned} n_f(t) &= n_{eq} + (n_0 - n_{eq}) \cdot \exp(-k_r t) \\ &\quad \text{(unimolecular)} \end{aligned} \tag{4.18a}$$

$$\begin{aligned} n_f(t) &= \frac{n_0 + k_r n_{eq}(n_0 - n_{eq}) \cdot t}{1 + k_r (n_0 - n_{eq}) \cdot t} \\ &\quad \text{(bimolecular)} \end{aligned} \tag{4.18b}$$

$$\begin{aligned} n_f(t) &= \frac{n_0 n_{eq}}{n_0 + (n_{eq} - n_0) \cdot \exp(-k_r n_{eq} t)} \\ &\quad \text{('intermediate').} \end{aligned} \tag{4.18c}$$

Expressions for the viscosity can be obtained by using Eq. (4.15):

$$\eta(t) = \frac{\eta_{eq}}{1+\left(\frac{\eta_{eq}}{\eta_0}-1\right)\cdot\exp(-k_r t)} \quad \text{(unimolecular)} \tag{4.19a}$$

$$\eta(t) = \frac{\left(\frac{\eta_{eq}-\eta_0}{\eta_{eq}}\right)\cdot kt+\eta_0}{1+\left(\frac{\eta_{eq}-\eta_0}{\eta_{eq}^2}\right)\cdot kt} \quad \text{(bimolecular)} \tag{4.19b}$$

$$\eta(t) = \eta_{eq}-(\eta_{eq}-\eta_0)\cdot\exp\left(-\frac{k}{\eta_{eq}}t\right) \quad \text{('intermediate')}, \tag{4.19c}$$

where the equilibrium viscosity η_{eq} corresponds to the equilibrium curve described by the Fulcher-Vogel-Equation [Eq. (4.2)] and Fig. 4.3(c). The definition of k [Eq. (4.17)] still applies here, but it cannot be interpreted as a viscosity increase rate $\dot{\eta}$ any more. For $\eta_{eq}\to\infty$, Eq. (4.19a) trends towards Eq. (4.16a). In the same way, both Eqs. (4.19b) and (4.19c) trend towards Eq. (4.16b) for $\eta_{eq}\to\infty$.

The temperature dependence of k in Eqs. (4.16b), (4.19b) and (4.19c) can be computed using Eqs. (4.9), (4.11), (4.15) and (4.17):

$$k = \frac{k_B T}{(\gamma_0\cdot\nu_0)^2}\cdot\frac{k_r^0}{k_f^0}\cdot\exp\left(\frac{Q_k}{k_B T}\right), \tag{4.20}$$

where

$$\boxed{Q_k = Q_{iso}-Q_{rel}}. \tag{4.21}$$

According to Eq. (4.20), k exhibits Arrhenius temperature dependence.

Chapter 5

Experimental details

5.1 Sample preparation

Phase change films of composition $Ge_4Sb_1Te_5$, $Ge_2Sb_2Te_5$ and $Ag_{0.055}In_{0.065}Sb_{0.59}Te_{0.29}$ were sputtered onto (100) silicon (Si) and (0001) sapphire (Al_2O_3) substrates[1]. These substrates were chosen because their elastic constants are (a) well known and (b) extremely stable upon annealing, which is important to obtain reliable data in mechanical measurements[2].

The sputter parameters were given in Chapter 2.2. Films of thicknesses between 200 nm and 1000 nm were sputtered. The exact thicknesses were determined by infrared spectroscopy and profilometry. For reasons, which will become clear later [Eq. (5.12)], the films could not be made too thin as this would have resulted in a bad signal-to-noise ratio in the stress measurement. For the same reason, the substrates had to be as thin as possible. However, as thinner substrates tend to break more easily and as they are also much more expensive, a compromise had to be made: 200 µm (Si) and 265 µm (Al_2O_3) substrates were chosen. Especially the Si substrates had to be handled very carefully as they tended to break easily. They were cleaved from polished 3-inch Si wafers along the (110) direction. The substrate geometry of both Si and Al_2O_3 was about 1 inch by 1/4 inch rectangle. The substrates were cleaned using distilled water

---

[1] For a more detailed characterization of these alloys see Chapter 2.1.

[2] In contrast to that, SiO_2 substrates could not be used for mechanical measurements: Due to the fact that SiO_2 substrates are amorphous, their elastic constants are unstable upon annealing due to structural relaxation.

and conventional dish washing liquid before sputtering onto them. Si substrates were identified by scratching a number on the unpolished back side with a diamond scribe. Al_2O_3 substrates were identified by storing them in different boxes. As determined from XRD measurements, the structure of the as-deposited films was amorphous [13, 14].

5.2 Stresses in thin films on substrates

Films constrained by a substrate are almost always mechanically stressed. There are various origins of stresses, including

- mismatch of lattice parameters of film and substrate
- volume change in the film due to phase transformations
- thermal effects (different thermal expansion coefficients of substrate and film).

The simple one-dimensional definitions of stress and strain (Chapter 4.1) are not sufficient to describe the state of stress in a film on a substrate. In a general *three-dimensional* state of stress, the stress and the strain are described by symmetrical *second rank tensors.* The stress tensor $\underline{\underline{\sigma}}$ is defined as [49, 50]

$$\underline{\underline{\sigma}} = \begin{pmatrix} \sigma_{11} & \tau_{12} & \tau_{13} \\ \tau_{12} & \sigma_{22} & \tau_{23} \\ \tau_{13} & \tau_{23} & \sigma_{33} \end{pmatrix} \tag{5.1a}$$

and the strain tensor $\underline{\underline{\epsilon}}$ as

$$\underline{\underline{\epsilon}} = \begin{pmatrix} \epsilon_{11} & \frac{1}{2}\gamma_{12} & \frac{1}{2}\gamma_{13} \\ \frac{1}{2}\gamma_{12} & \epsilon_{22} & \frac{1}{2}\gamma_{23} \\ \frac{1}{2}\gamma_{13} & \frac{1}{2}\gamma_{23} & \epsilon_{33} \end{pmatrix} . \tag{5.1b}$$

σ_{ii} and ϵ_{ii} are the *axial* stresses and strains respectively in the direction of the orthogonal coordinate axes. τ_{ij} and γ_{ij} are the shear stresses and the shear strains, respectively.

Stresses in *elastically isotropic* films (e. g. polycrystalline and amorphous films) on substrates, which are elastically isotropic *in* the substrate plane[3] can in general be

---

[3] (100) Si and (0001) Al_2O_3 substrates are elastically isotropic *in* the substrate plane.

assumed to be *biaxial.* This means that there is a constant stress σ *in* the film plane, whereas the stress *perpendicular* to the film plane vanishes. In this case the stress tensor $\underline{\underline{\sigma}}$ can be *represented* most simply if the orthogonal coordinate axes are chosen so that the x_3-axis points perpendicular to the film surface. For a biaxial stress, all shear stresses vanish in this representation ($\tau_{ij} = 0$) . The remaining elements are $\sigma_{11} = \sigma_{22} = \sigma$ and $\sigma_{33} = 0$.

5.2.1 Elastic behavior

For elastically isotropic material, Hooke's law [49, 50] can be applied, which relates the tensors of stress $\underline{\underline{\sigma}}$ and strain $\underline{\underline{\epsilon}}$ in elastic deformation. This law states

$$\begin{aligned}
\epsilon_{11} &= \frac{\sigma_{11}}{E} - \nu\frac{\sigma_{22}}{E} - \nu\frac{\sigma_{33}}{E} && \text{(5.2a)}\\
\epsilon_{22} &= \frac{\sigma_{22}}{E} - \nu\frac{\sigma_{11}}{E} - \nu\frac{\sigma_{33}}{E} && \text{(5.2b)}\\
\epsilon_{33} &= \frac{\sigma_{33}}{E} - \nu\frac{\sigma_{11}}{E} - \nu\frac{\sigma_{22}}{E} && \text{(5.2c)}
\end{aligned}$$

$$\gamma_{ij} = \frac{1}{G}\tau_{ij}. \qquad \text{(5.2d)}$$

E is *Young's modulus*, ν *Poisson's ratio* and G the *rigidity modulus* of the material. G can be expressed in terms of E and ν,

$$G = \frac{E}{2(1+\nu)}, \qquad \text{(5.3)}$$

which is a consequence of the fact that the elastic properties of elastically isotropic material can be completely described by *two* independent constants.

In the case of a biaxial stress σ in an elastically isotropic film Eqs. (5.2) simplify if the orientation of the basis is chosen as described above:

$$\begin{aligned}
\epsilon := \epsilon_{11} = \epsilon_{22} &= \frac{1-\nu}{E} \cdot \sigma && \text{(5.4a)}\\
\epsilon_{33} &= -\frac{2\nu}{E} \cdot \sigma = -\frac{2\nu}{1-\nu} \cdot \epsilon && \text{(5.4b)}\\
\gamma_{ij} = \tau_{ij} &= 0 && \text{(5.4c)}
\end{aligned}$$

This yields *Hooke's law for biaxial stress*

$$\boxed{\sigma = Y \cdot \epsilon}, \qquad \text{(5.5)}$$

where

$$\boxed{Y = \frac{E}{1-\nu}} \tag{5.6}$$

is called the *biaxial (elastic) modulus* of the film. ϵ is the *biaxial strain.*

5.2.2 Plastic behavior (Viscous flow)

In amorphous films, the biaxial stress σ can relax *plastically* towards $\sigma = 0$ by viscous flow. If the film is constrained by a substrate, the total biaxial strain $\epsilon_{el} + \epsilon_{pl}$ is constant in time for $T =$ const. ϵ_{el} is the biaxial elastic component and ϵ_{pl} the biaxial plastic component of the strain. Differentiation with respect to the time yields

$$\dot{\epsilon}_{el} + \dot{\epsilon}_{pl} = 0. \tag{5.7}$$

$\dot{\epsilon}_{el}$ can be determined from Eq. (5.5):

$$\dot{\epsilon}_{el} = \frac{\dot{\sigma}}{Y_f} \tag{5.8}$$

A derivation of $\dot{\epsilon}_{pl}$ is more complicated. As already mentioned, viscous flow occurs if shear stresses are present [Eq. (4.1)]. However, the magnitude of the shear stresses depend on the orientation of the basis (compare with Fig. 4.1). Furthermore, according to the spectral theorem of linear algebra, the basis can *always* be chosen in such a way that all shear stresses vanish, i. e. that the stress tensor $\underline{\underline{\sigma}}$ becomes diagonal. However, a physical law like the occurrence of viscous flow must be independent of the choice of basis orientation. In order to solve this problem, von Mises' definition of the *equivalent stress* and the *equivalent strain* is applied [50]: If plastic flow is caused by *combined*[4] stresses inducing *combined* plastic strain rates, an equivalent stress σ_{eq} and an equivalent plastic strain rate $\dot{\epsilon}_{eq}$ can be derived. In a hypothetical tensile test, the *uniaxial* stress σ_{eq} would induce a *uniaxial* plastic strain rate of $\dot{\epsilon}_{eq}$. Von Mises showed that

$$\sigma_{eq} = \sqrt{\frac{1}{2}[(\sigma_{22}-\sigma_{33})^2 + (\sigma_{33}-\sigma_{11})^2 + (\sigma_{11}-\sigma_{22})^2] + 3(\tau_{23}^2 + \tau_{13}^2 + \tau_{12}^2)} \tag{5.9a}$$

---

[4] 'Combined' means that all six independent tensor components [Eqs. (5.1a) and (5.1b)] are allowed to be unequal to zero.

$$\dot{\epsilon}_{eq} = \sqrt{\frac{2}{9}[(\dot{\epsilon}_{22} - \dot{\epsilon}_{33})^2 + (\dot{\epsilon}_{33} - \dot{\epsilon}_{11})^2 + (\dot{\epsilon}_{11} - \dot{\epsilon}_{22})^2] + \frac{1}{3}(\dot{\gamma}_{23}^2 + \dot{\gamma}_{13}^2 + \dot{\gamma}_{12}^2)}. \tag{5.9b}$$

The biaxial plastic strain rate $\dot{\epsilon}_{pl}$ as a function of biaxial stress σ and viscosity η can be obtained if a pure biaxial stress σ and a pure shear stress τ are found, which result in the same equivalent stress σ_{eq} and equivalent strain rate $\dot{\epsilon}_{eq}$:

(1) Pure biaxial stress

- $\sigma_{11} = \sigma_{22} =: \sigma$
- $\epsilon_{11} = \epsilon_{22} =: \epsilon_{pl}$ and $\epsilon_{33} = -2\epsilon_{pl}$,

with all other components of the stress tensor $\underline{\underline{\sigma}}$ and the strain tensor $\underline{\underline{\epsilon}}$ being zero. From Eq. (5.9) it follows $\sigma_{eq} = \sigma$ and $\dot{\epsilon}_{eq} = 2\dot{\epsilon}_{pl}$.

(2) Pure shear stress

- $\tau_{12} =: \tau$
- $\gamma_{12} =: \gamma$,

with all other components of the stress tensor $\underline{\underline{\sigma}}$ and the strain tensor $\underline{\underline{\epsilon}}$ being zero. From Eq. (5.9) it follows $\sigma_{eq} = \sqrt{3}\tau$ and $\dot{\epsilon}_{eq} = \frac{\dot{\gamma}}{\sqrt{3}}$.

Therefore, in combination and by additionally using Eq. (4.1),

$$\eta = \frac{\tau}{\dot{\gamma}} \overset{(2)}{=} \frac{\sigma_{eq}}{3\dot{\epsilon}_{eq}} \overset{(1)}{=} \frac{\sigma}{6\dot{\epsilon}_{pl}}$$

or

$$\dot{\epsilon}_{pl} = \frac{\sigma}{6\eta} \tag{5.10}$$

Substituting Eqs. (5.8) and (5.10) into Eq. (5.7) yields

$$\boxed{\frac{\sigma}{6\eta} + \frac{\dot{\sigma}}{Y_f} = 0}. \tag{5.11}$$

Eq. (5.11) describes viscous flow in a thin amorphous film constrained by a substrate upon the application of a *biaxial* stress σ for $T =$const.

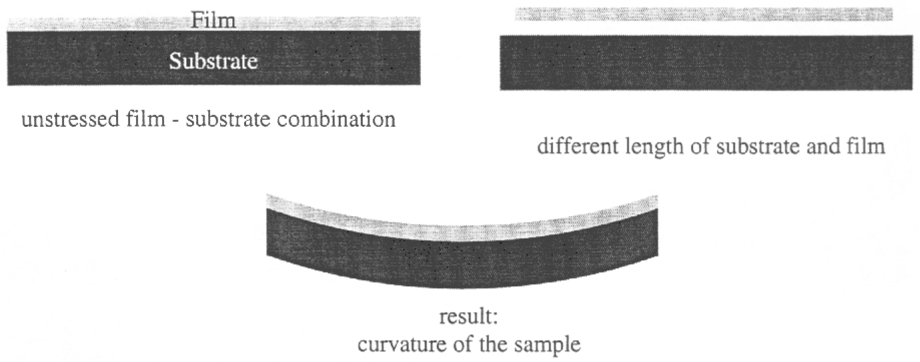

Figure 5.1: Sample curvature induced by a tensile film stress. From [51].

5.2.3 Sample curvature and Stoney Equation

A biaxial stress in a thin film constrained by a substrate induces a sample curvature. This is illustrated in Fig. 5.1: A totally unstressed film does not induce any substrate curvature (a). In a 'Gedanken experiment', the film is now removed from the substrate and made 'shorter' than the substrate (b). This could be obtained by heating up film and substrate and "using" their different thermal expansion coefficients. In order to 'fix' the film to the substrate again, it has to be 'pulled apart' in order to adapt its area to the substrate area. The result is a tensile stress in the film which induces a sample curvature (c). A compressive stress in the film induces the opposite curvature (Fig. 5.2).

Stoney [52] derived a relation between film stress σ and sample curvature κ:

$$\boxed{\sigma = \frac{1}{6} \cdot Y_s \cdot \frac{d_s^2}{d_f} \cdot (\kappa - \kappa_0), \qquad (d_f \ll d_s)}, \tag{5.12}$$

where Y_s is the biaxial elastic modulus of the *substrate*, and d_s and d_f are substrate and film thicknesses respectively. The sample curvature is defined as $\kappa = \frac{1}{R}$, where R is the radius of curvature of the sample (Fig. 5.2). κ_0 is the curvature of the bare substrate before film deposition. Stoney's equation is only valid for 'thin' films: $d_f \ll d_s$. It should be pointed out that the elastic properties of the *film* do not contribute to this formula.

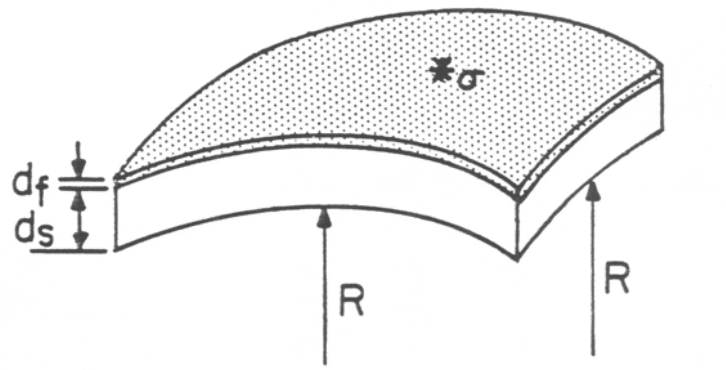

Figure 5.2: Sample curvature induced by a compressive film stress. For the special case of a *biaxial* stress the two indicated radii of curvature R are equal. From [47].

5.2.4 Viscosity measurements

Viscous flow in a thin film constrained by a substrate can be observed experimentally by stress relaxation experiments. For $T =$const, the viscosity η is obtained by substituting Stoney's Equation [Eq. (5.12)] into Eq. (5.11):

$$\boxed{\eta(t) = -\frac{Y_f}{6} \cdot \frac{\kappa(t) - \kappa_0}{\dot{\kappa}(t)}}. \tag{5.13}$$

Eq. (5.13) shows the important fact that only three quantities have to be measured experimentally in order to determine the viscosity η:

1. the biaxial modulus Y_f of the film
2. the curvature $\kappa(t)$ as a function of time at a constant temperature
3. the curvature κ_0 of the bare substrate.

The values for Y_s, d_s and d_f, which are required for the determination of the stress σ [Eq. (5.12)], are *not* required for the determination of the viscosity η. These quantities cancel out by substituting Eq. (5.12) into Eq. (5.11). Therefore, errors in the determination of Y_s, d_s and d_f do not propagate to the error of the viscosity.

5.3 Experimental Setup

A wafer curvature setup as described by Nix [53] was employed in order to measure stresses in the phase change films. This setup is based on an optical laser scanning technique, which monitors the radius of curvature of a sample *in-situ* during annealing. Due to the fact that the measurements were performed at both Harvard University and RWTH Aachen, two slightly different setups were employed.

5.3.1 Setup at Harvard University

The apparatus was constructed by A. Witvrouw [47] and is shown schematically in Fig. 5.3. The main components are a vacuum chamber, a sample furnace, optics for measuring substrate curvature (laser, lens and mirrors) and a computer for data acquisition (not shown). The sample is placed inside the vacuum chamber and rests on two sapphire knife-edge supports which are about 1 cm apart. The vacuum chamber is evacuated by a mechanical and a diffusion pump to 10^{-5} Torr and backfilled with a helium-hydrogen-mixture (95.01% helium and 4.99% hydrogen) to 17 kPa overpressure. Before the helium flows into the chamber, it passes through an oxygen getter (Ti at 800℃) in order to keep oxygen away from the inside of the vacuum chamber. This extensively suppresses oxidation in the chamber at elevated temperatures. The helium leaves the chamber at a second valve, which results in a steady-state helium flow through the chamber and a high thermal uniformity inside the chamber during the measurement. The sample inside the chamber can be heated up by the sample furnace. The surrounding helium heats the sample from both top and bottom, which minimizes temperature gradients in the sample. The temperature is measured by four different thermocouples, which measure the helium temperature about 2 mm away from the sample. This allows a continuous monitoring of the thermal uniformity of the helium around the sample. The entire vacuum chamber is continuously water-cooled. This accelerates the cooling process after annealing. If the furnace is switched off, the basic temperature of the chamber is 12 ℃. The laser beam passes a lens, a translating prism, a mirror and a window at the top of the chamber. The beam is reflected at the sample towards a null detector which moves in two dimensions to find the center of the reflected beam. The laser scans across the sample in 9 steps. On the sample, these

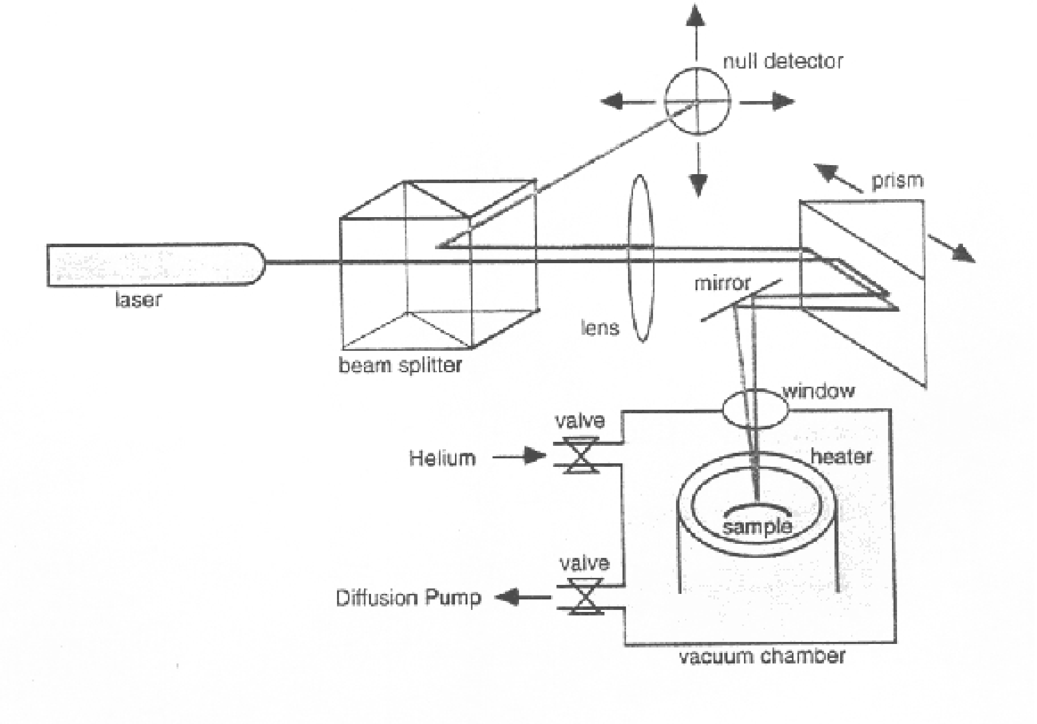

Figure 5.3: Wafer Curvature Setup (Harvard): The sample surface is optically scanned by a laser *in situ* during annealing. This gives information about the sample curvature. From [35].

steps are about 1 mm apart. The sample curvature is evaluated from the positions of prism and detector during these 9 steps. These positions are recorded by the computer. The entire procedure takes about 30 seconds. Immediately afterwards, the curvature is measured again.

5.3.2 Setup at the RWTH Aachen

This setup was constructed by T. Pedersen, P. Aretz and R. Drese. It works similarly to the setup described in Chapter 5.3.1 and was already described in detail in [51]. Important differences are:

1. The sample is heated in vacuum ($< 10^{-4}$ mbar) by heat radiation: Two heat radiators are placed inside the vacuum chamber approximately 8 cm above the sample.

2. Temperature gradients in the sample are minimized by placing the sample on top of a copper plate, which is larger than the sample itself. Therefore, the heat of the radiators is also absorbed by the copper plate, which additionally heats the sample from the bottom due to the high thermal conductivity of copper.

3. The temperature is measured by only one thermocouple, which is fixed on a reference sample on top of the copper plate next to the sample.

4. The detector is only one-dimensional. It is a position-sensitive detector, which is not able to move. This kind of detector exhibits an advantage and a disadvantage in contrast to the null detector described in Chapter 5.3.1: The advantage is that the sample curvature can be measured about ten times quicker, i. e. in about 3 seconds. This is due to the fact that the null detector needs some time for moving. Therefore, about ten times more data points can be recorded within a given time window. The disadvantage is that the detector is not able to compensate for a change in the direction of reflection *orthogonal* to the detector slit. This implies the risk that the laser beam does not hit the detector any more in the course of the measurement. Therefore, the measurement has to be supervised continuously in order to adapt the tilting angle of the copper plate manually if necessary. In case the measurement is very sensitive towards the stress baseline, the measurement has to be repeated.

5. The detector is also able to measure the reflectivity of the sample. This is especially an advantage for the study of phase change films as they undergo a reflectivity change upon crystallization (see Chapter 7).

6. In contrast to the setup at Harvard, the chamber is not water cooled. As a consequence, cooling times below about 100 ℃ are significantly longer (below 100 ℃, the chamber takes about one hour to cool down to room temperature).

Chapter 6

Results and discussion: Stresses in the amorphous phase

6.1 Elastic Constants

The biaxial moduli Y_f of the phase change films were determined by measurements of stress versus temperature using the wafer curvature setup: If no plastic flow occurs, a change in biaxial film stress $\Delta\sigma$ with temperature T is induced by the difference in linear coefficients of thermal expansion of the film α_f and the substrate α_s (*'thermal stress'*) [54]:

$$\boxed{\underbrace{\frac{\Delta\sigma}{\Delta T}}_{\text{measure}} = \underbrace{Y_f}_{\text{unknown}} \cdot (\underbrace{\alpha_s}_{\text{known}} - \underbrace{\alpha_f}_{\text{unknown}})}. \tag{6.1}$$

The linear coefficient of thermal expansion (CTE) at constant pressure is defined as

$$\alpha = \frac{1}{l} \cdot \frac{dl}{dT}, \tag{6.2}$$

where l is the length of the material. If the CTE α_s of the substrate is known, a measurement of $\frac{\Delta\sigma}{\Delta T}$ on this substrate is still not sufficient for the determination of Y_f due to the additional unknown α_f. Therefore, *two* different substrates with *two* different known values for α_s are needed in order to solve for the two unknowns Y_f and α_f. This method additionally determines α_f. (100) silicon (Si) and (0001) sapphire (Al_2O_3) substrates were chosen for that purpose. $\frac{\Delta\sigma}{\Delta T}$ was measured for all three phase change films on both Si and Al_2O_3 substrates. Literature values for the biaxial moduli of the substrates were used [55, 56]: $Y_s = 180.5\,\mathrm{GPa}$ (Si) and $Y_s = 609.0\,\mathrm{GPa}$ (Al_2O_3). Figures 6.1–6.3 show some results for silicon substrates. By convention, positive stresses are *tensile* and negative stresses *compressive*. $\frac{\Delta\sigma}{\Delta T}$ of the amorphous films was measured for $T \leq 100\,^\circ\mathrm{C}$. Before the measurement, the samples were annealed at 100 °C for about two days in order to eliminate viscous flow during the measurements. During this annealing process, the film stress relaxed completely. Reversible behavior was observed upon subsequent cooling and heating in the amorphous phase in the temperature interval of [12 °C, 100 °C]. The slope $\frac{\Delta\sigma}{\Delta T}$ was determined by a linear fitting procedure. For silicon substrates, a fitting interval of [20 °C, 100 °C] was used and for Al_2O_3 substrates an interval of [40 °C, 100 °C]. $\frac{\Delta\sigma}{\Delta T}$ was observed to be independent of heating rate as expected: heating (cooling) rates of −3, −2, −1, −0.5, 0.5, 1, 2 and 3 K/min were applied. Results for $\frac{\Delta\sigma}{\Delta T}$ from several samples, different cooling/ heating-cycles and different heating rates were averaged using the number of data points (which is related to the heating rate) as a weighting factor. Results are listed in Table 6.1.

After about four or five thermal cycles in the amorphous phase, the sample was further heated up in order to crystallize the film completely. At the crystallization temperature, there was a large stress increase due to densification in the film (Figs. 6.1–6.3). The crystallization temperatures correspond approximately to the results obtained from DSC measurements in Part I of this thesis (Table 3.1). The amount of stress increase is discussed in more detail in Chapter 7.

After the stress increase, the stress relaxes *plastically* as this evolution is *irreversible* (Figs. 6.1–6.3). Further thermal cycling in the crystalline phase yields reversible (i. e. elastic) behavior again. However, the temperature dependence of the thermal stress is higher for the crystalline phase. $\frac{\Delta\sigma}{\Delta T}$ could also be determined for the crystalline phase by a linear fitting procedure and by averaging the results from several samples, thermal cycles and different heating rates. For *silicon* substrates, fitting intervals of [20 °C, 160 °C], [20 °C, 120 °C] and [20 °C, 140 °C] were used for $Ge_4Sb_1Te_5$, $Ge_2Sb_2Te_5$ and AgInSbTe, respectively. For Al_2O_3 substrates, a fitting interval of [40 °C, 100 °C] was chosen for all three alloys in the crystalline phase. Within all these intervals the slope was constant but outside it was not (Figs. 6.1–6.3). This is due to temperature dependent thermal expansion coefficients of both film and substrate.

Film thickness decreases upon crystallization of 9.0 % ($Ge_4Sb_1Te_5$), 6.5 % ($Ge_2Sb_2Te_5$)

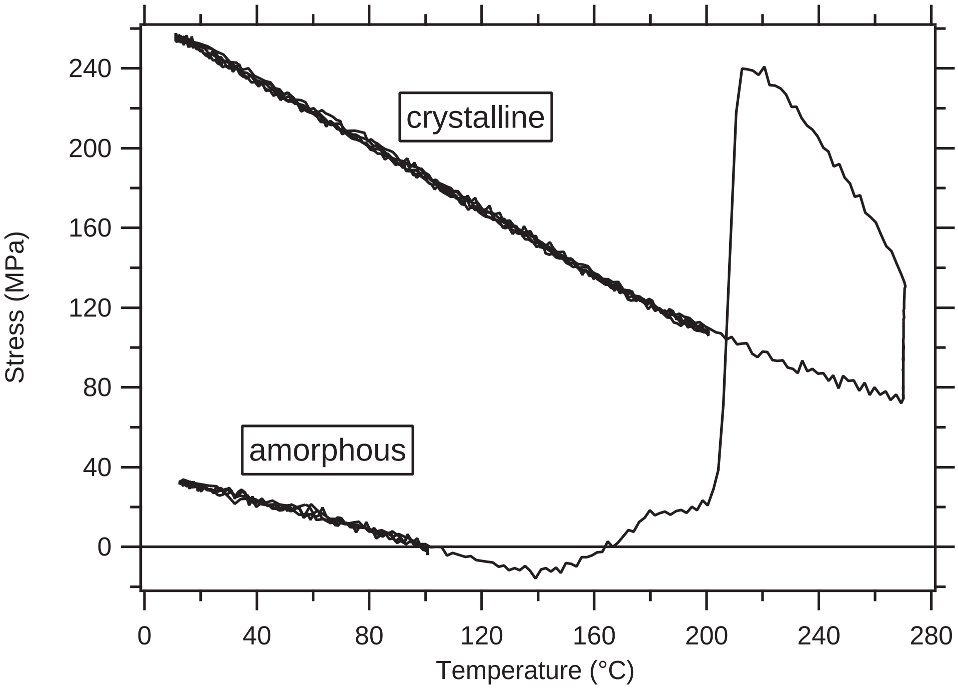

Figure 6.1: Reversible thermal cycling of $Ge_4Sb_1Te_5$ in both amorphous and crystalline state. At the crystallization temperature, a large stress increase occurs due to densification in the film. Annealing time at 270 ℃: 45 min. Film thickness: 725 nm. Substrate: Si. Wafer Curvature Setup: Harvard. Sample number: '4-415-43'.

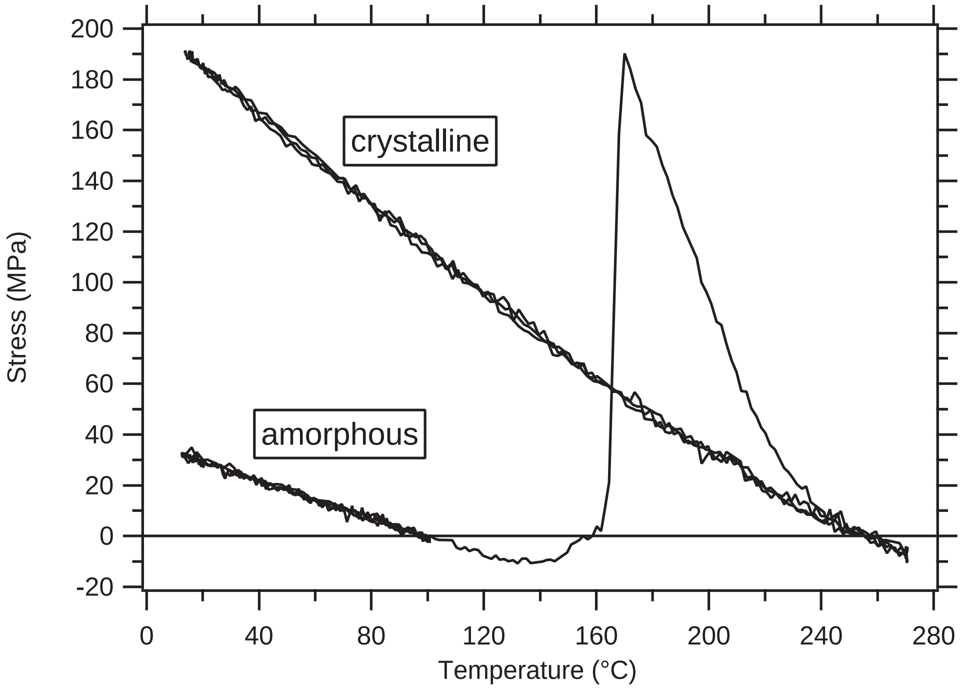

Figure 6.2: Reversible thermal cycling of $Ge_2Sb_2Te_5$. Annealing time at 270 ℃: 15 min. Film thickness: 965 nm. Substrate: Si. Wafer Curvature Setup: Harvard. Sample number: '4-225-36'.

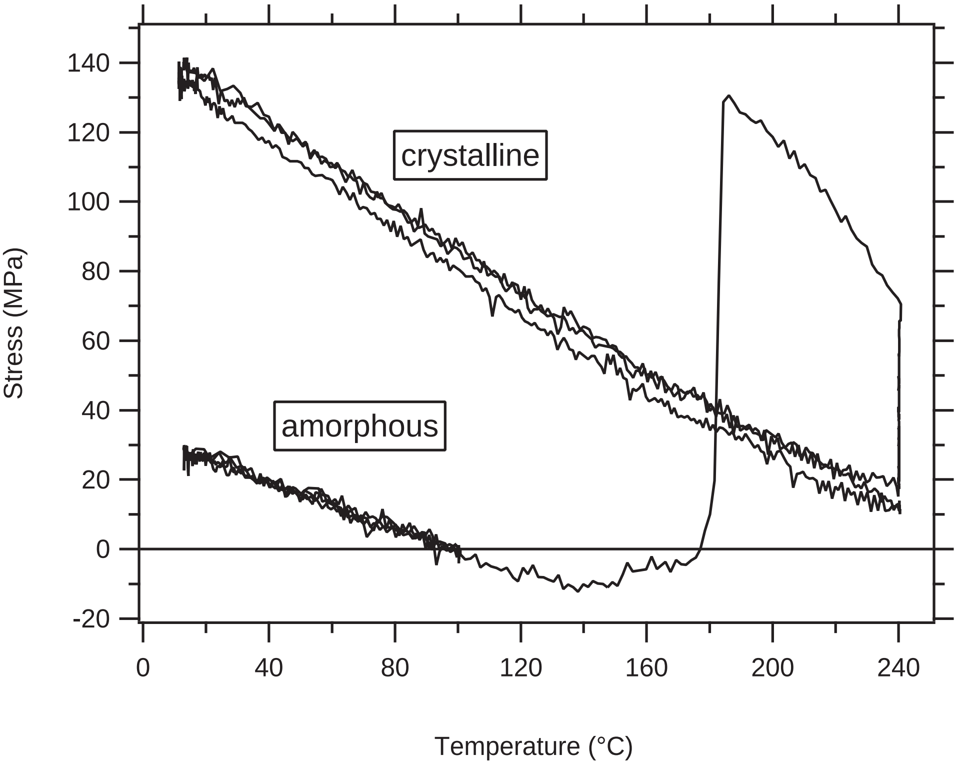

Figure 6.3: Reversible thermal cycling of AgInSbTe. Annealing time at 240 °C: 60 min. Film thickness: 850 nm. Substrate: Si. Wafer Curvature Setup: Harvard. Sample number: '9-ag-38'.

Table 6.1: Measured slope $\Delta\sigma/\Delta T$, calculated biaxial modulus Y_f and linear coefficient of thermal expansion α_f for three Te alloys for both the amorphous and the crystalline state. The fitting intervals for the slopes $\Delta\sigma/\Delta T$ are given in the text. Y_f and α_f were determined for a temperature interval of [40 ℃, 100 ℃]. $\Delta\sigma/\Delta T$ exhibits very small errors due to the fact that it is an average value obtained from several samples and measurements. As-deposited film thicknesses: 725 nm ($Ge_4Sb_1Te_5$), 965 nm ($Ge_2Sb_2Te_5$) and 850 nm (AgInSbTe).

		$\left(\frac{\Delta\sigma}{\Delta T}\right)^{(\mathrm{Si})}$ (MPa K^{-1})	$\left(\frac{\Delta\sigma}{\Delta T}\right)^{(\mathrm{Al_2O_3})}$ (MPa K^{-1})	Y_f (GPa)	α_f (10^{-6} K^{-1})
$Ge_4Sb_1Te_5$	amorphous	-0.375 ± 0.001	-0.281 ± 0.008	33.9 ± 5.8	14.0 ± 1.9
	crystalline	-0.895 ± 0.001	-0.723 ± 0.010	62.4 ± 10.8	17.2 ± 2.3
$Ge_2Sb_2Te_5$	amorphous	-0.384 ± 0.001	-0.307 ± 0.008	27.6 ± 4.7	16.8 ± 2.6
	crystalline	-0.971 ± 0.001	-0.846 ± 0.009	45.2 ± 8.2	24.4 ± 3.8
AgInSbTe	amorphous	-0.332 ± 0.001	-0.303 ± 0.011	10.5 ± 2.2	34.4 ± 12.9
	crystalline	-0.672 ± 0.001	-0.609 ± 0.012	22.6 ± 4.8	32.6 ± 7.5

and 5.5 % (AgInSbTe) as determined from x-ray reflectivity (XRR) measurements [19, 20, 13] had to be considered in order to evaluate the stress correctly for the crystalline phase. Results for $\Delta\sigma/\Delta T$ of the crystalline phase are also listed in Table 6.1. For all alloys and both substrates, $|\Delta\sigma/\Delta T|$ of the crystalline phase is more than two times higher than for the amorphous phase. Slopes on Si are slightly higher than slopes on Al_2O_3.

Equation (6.1) was used in order to determine Y_f and α_f for both amorphous and crystalline phase (Table 6.1):

$$Y_f = \frac{\left(\frac{\Delta\sigma}{\Delta T}\right)^{(\mathrm{Si})} - \left(\frac{\Delta\sigma}{\Delta T}\right)^{(\mathrm{Al_2O_3})}}{\alpha_s^{(\mathrm{Si})} - \alpha_s^{(\mathrm{Al_2O_3})}} \tag{6.3a}$$

$$\alpha_f = \frac{\alpha_s^{(\mathrm{Al_2O_3})} \cdot \left(\frac{\Delta\sigma}{\Delta T}\right)^{(\mathrm{Si})} - \alpha_s^{(\mathrm{Si})} \cdot \left(\frac{\Delta\sigma}{\Delta T}\right)^{(\mathrm{Al_2O_3})}}{\left(\frac{\Delta\sigma}{\Delta T}\right)^{(\mathrm{Si})} - \left(\frac{\Delta\sigma}{\Delta T}\right)^{(\mathrm{Al_2O_3})}} \tag{6.3b}$$

The following literature values [57] for the CTE of the substrates were used: $\alpha_s^{(\mathrm{Si})} = (2.90\pm0.30)\cdot10^{-6}\mathrm{K}^{-1}$ and $\alpha_s^{(\mathrm{Al_2O_3})} = (5.67\pm0.35)\cdot10^{-6}\mathrm{K}^{-1}$. The values correspond to a temperature of 70 ℃ and the errors consider the fact that these CTEs are temperature dependent inside the fitting interval.

Y_f is a factor of about two higher for the crystalline phases than for the amorphous phases. In general, higher biaxial moduli for the crystalline phases are expected due to the fact that it is easier to displace some of the atoms in the random network of the amorphous phase. However, a factor of two is quite uncommon. α_f of amorphous and crystalline phase are of similar magnitude, which is indeed expected for all kind of glass formers [5]. It should be pointed out that $Ge_4Sb_1Te_5$ exhibits the largest Y_f and the smallest α_f for both amorphous and crystalline phase. On the other hand side, AgInSbTe exhibits the smallest Y_f and the largest α_f. A general rule of thumb states that the elastic modulus *increases* and the CTE *decreases* with *increasing* melting temperature T_m. This also applies for the Te alloys studied here (compare Table 3.2).

In order to discuss the results more thoroughly, *Grüneisen's law* [12] is applied:

$$\boxed{\frac{\alpha^* \cdot B}{C_V} = \gamma}. \tag{6.4}$$

α^* is the *volume* CTE, which is three times larger than the *linear* CTE α defined in Eq (6.2):

$$\alpha^* = \frac{1}{V} \cdot \left(\frac{\partial V}{\partial T}\right)_p = 3\alpha \tag{6.5}$$

The *bulk modulus* B is the inverse of the isothermal compressibility κ_T:

$$B = \frac{1}{\kappa_T} = -V\left(\frac{\partial p}{\partial V}\right)_T \tag{6.6}$$

B can be expressed as a function of the biaxial modulus Y and Poisson's ratio ν:

$$B = \frac{1}{3} \cdot Y \cdot \frac{1-\nu}{1-2\nu}. \tag{6.7}$$

ν was assumed to be 0.30 ± 0.05, a value typical for many materials including chalcogenides. C_V is the heat capacity per volume of the body at constant volume. According to Chapter 3.5, it can be approximated by the classical Dulong-Petit value in the temperature range of interest, e. g. for $Ge_4Sb_1Te_5$:

$$C_V = 3 \cdot k_B \cdot \rho \cdot \frac{4+1+5}{4 \cdot M_{Ge} + 1 \cdot M_{Sb} + 5 \cdot M_{Te}}, \tag{6.8}$$

where ρ is the mass density of $Ge_4Sb_1Te_5$ and M the atomic mass of the corresponding element. The different densities of the amorphous and the crystalline phase had to be

Table 6.2: Grüneisen constant γ for both amorphous and crystalline state for three Te alloys determined from stress versus temperature measurements.

	γ (amorphous)	γ (crystalline)
$Ge_4Sb_1Te_5$	0.62 ± 0.25	1.29 ± 0.53
$Ge_2Sb_2Te_5$	0.62 ± 0.27	1.38 ± 0.60
AgInSbTe	0.49 ± 0.34	0.96 ± 0.52

considered as the phase change material densifies during crystallization[1]. γ is called the *Grüneisen constant*[2] and typically adopts a value in the range of 1 to 3. γ was evaluated for both the amorphous and the crystalline phase. An error of 10% was assumed for the heat capacity C_V. According to Table 6.2, the values of γ for the crystalline states agree well to Grüneisen's law as they are in the range of 1 to 3. However, γ for the amorphous phase seems to be quite low for all alloys. This reflects the fact that the biaxial moduli of the amorphous phases are unusually low.

6.2 Viscous flow

6.2.1 Stress relaxation

The wafer curvature setup was also employed to measure the sample curvature $\kappa(t)$ as a function of time at various annealing temperatures T: Apart from Y_f, $\kappa(t)$ is also needed for the determination of the viscosity η [Eq. (5.13)]. Due to the fact that the biaxial modulus Y_s for Al_2O_3 is about three times larger than for Si, measurements with Al_2O_3 substrates are expected to result in a much lower signal-to-noise-ratio than measurements with Si substrates [Eq. (5.12)]. Attempts were made to measure $\kappa(t)$ on Al_2O_3 substrates but the result was indeed unsatisfactory: the signal-to-noise ratio was too low. Therefore, all results presented hereafter result from measurements on

---

[1] The densities for both amorphous and crystalline phase were determined by x-ray reflectivity (XRR) measurements. Within range of error the density increase coincides well with the film thickness decrease mentioned above for all three alloys. [19, 20, 13]

[2] Grüneisen constants for various materials are: Fe (2.10), Co (1.95), Ni (2.00), Cu (1.96), Al (2.17), K (1.25), Pt (2.54), W (1.62), Ag (2.40), Pd (2.23).

Si substrates only.

Figs. 6.4–6.6 show some results. In order to obtain more physical insight, the stress $\sigma(t)$ [which was computed using Eq. (5.12)] rather than the curvature $\kappa(t)$ is plotted here as a function of time. However, it is pointed out again, that the *absolute* values for the stress σ are *not* needed for the evaluation of the viscosity [Eq. (5.13)].

Generally, the stress relaxation curves look very similar for all three phase change materials. The initial stress observed at 12 ℃ is a sum of the deposition stress and the thermal stress induced upon cooling from room temperature to 12 ℃ [Eq. (6.1)]. Typically, the initial stress at 12 ℃ was slightly negative (about -2 MPa) for $Ge_4Sb_1Te_5$ and $Ge_2Sb_2Te_5$ and slightly positive (about 4 MPa) for AgInSbTe. By comparison with Table 6.1, the deposition stress at room temperature ($\sim$ 22 ℃) can therefore be estimated to -6 MPa for $Ge_4Sb_1Te_5$ and $Ge_2Sb_2Te_5$ and +1 MPa for AgInSbTe. However, it should be mentioned that these numbers might depend strongly on the age of the sample: the samples used for the stress relaxation experiments described below were typically more than two months old.

A negative film stress increase (i. e. a compressive stress) is induced by increasing the temperature from 12 ℃ to the first annealing temperature [thermal stress, Eq. (6.1)]. Upon annealing the sample at a constant temperature, the stress relaxes. Heating the sample to the next annealing temperature induces thermal stress again. The baseline κ_0 or $\sigma_{base} = \frac{1}{6} Y_s \frac{d_s^2}{d_f} \kappa_0$ [Eq. (5.12)] was obtained by using it as a *fitting parameter* at the highest annealing temperature[3]. In order to obtain precise results for the fitting parameter σ_{base}, the annealing time at the highest annealing temperature was longer than at lower temperatures. Attempts were made to obtain the baseline by stripping off the film after having performed the stress relaxation measurement using nitric acid (HNO_3) and *measuring* the curvature κ_0 of the bare substrate. These measured baselines, however, were often inconsistent with the stress relaxation data: in many cases they would have implied either a stress relaxation over the baseline or a stress relaxation too far away from the baseline. Probably the entire setup was very sensitive to opening the chamber and replacing the sample. Another possibility is that the thickness of an oxidation layer on the backside of the substrate could have been increased

---

[3] For details about the fitting procedure see Chapter 6.2.2.

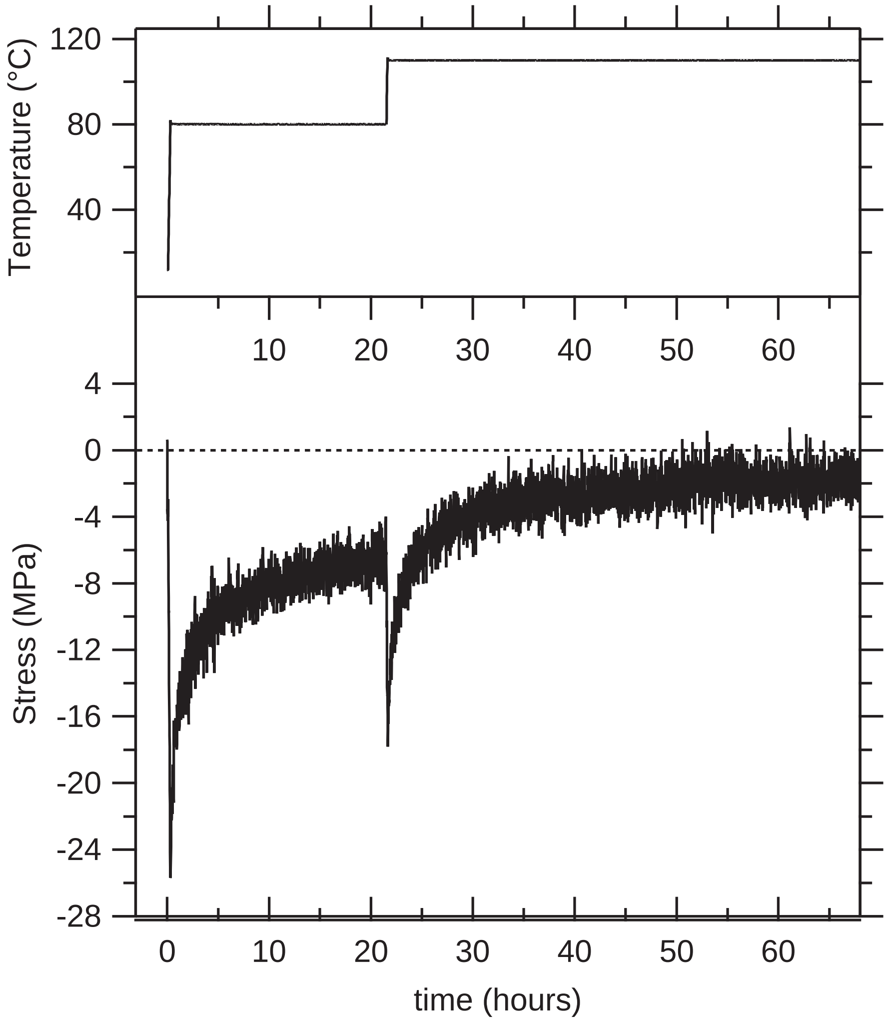

Figure 6.4: Stress relaxation for $Ge_4Sb_1Te_5$ as a function of time. Film thickness: 725 nm. Substrate: Si. Wafer Curvature Setup: Harvard. For comparison with Table 6.4, this sample is numbered '7-415-08'.

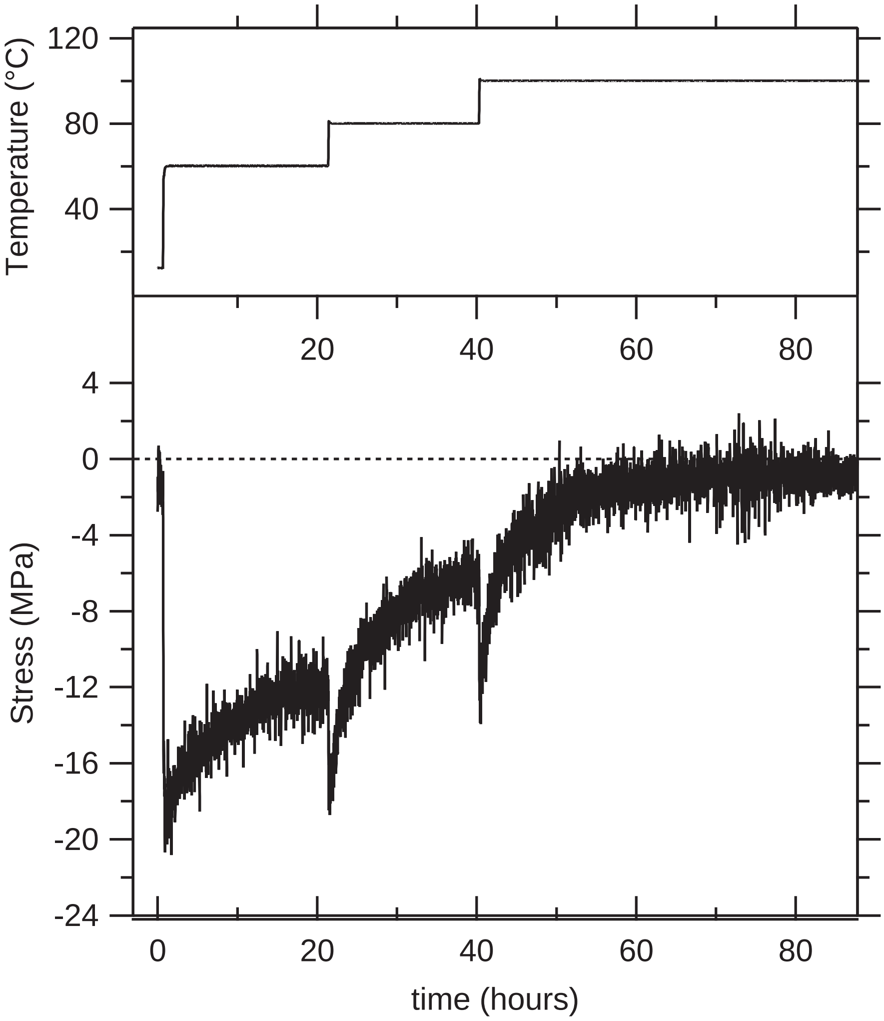

Figure 6.5: Stress relaxation for $Ge_2Sb_2Te_5$ as a function of time. Film thickness: 965 nm. Substrate: Si. Wafer Curvature Setup: Harvard. For comparison with Table 6.4, this sample is numbered '4-225-36'.

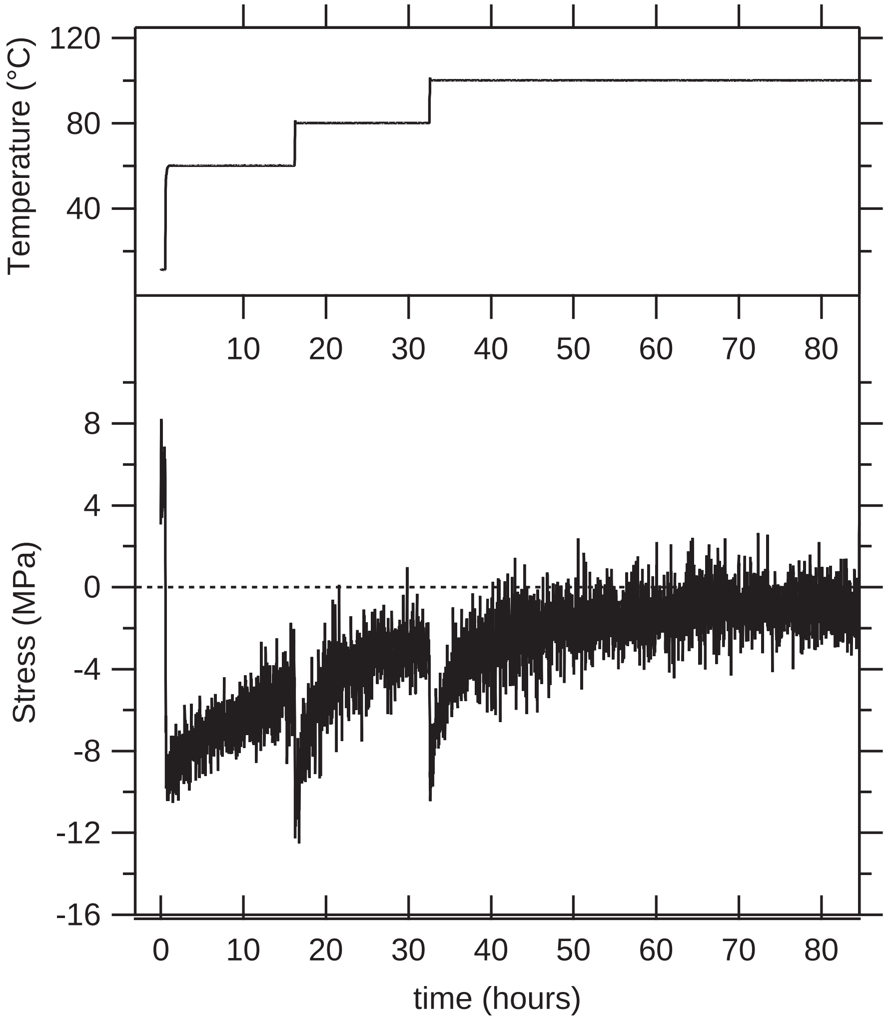

Figure 6.6: Stress relaxation for AgInSbTe as a function of time. Film thickness: 850 nm. Substrate: Si. Wafer Curvature Setup: Harvard. For comparison with Table 6.4, this sample is numbered '9-ag-38'.

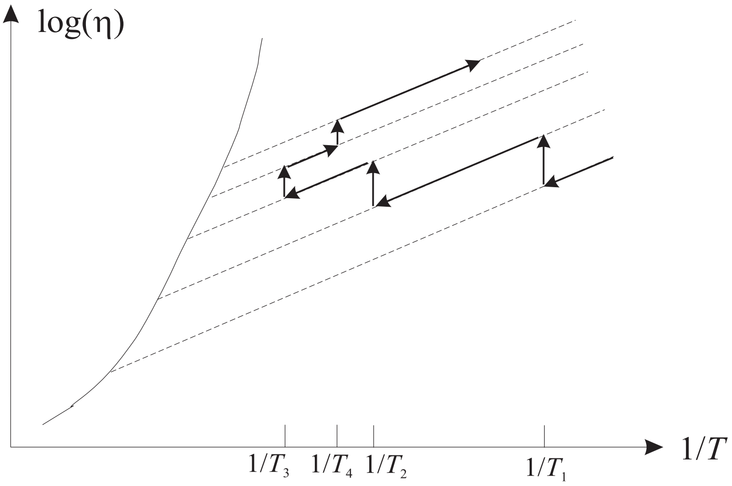

Figure 6.7: Qualitative tracking of the viscosity evolution during a typical stress relaxation experiment as shown in Figs. 6.4–6.6. In this graph, the annealing temperatures could be exemplary $T_1 = 60$°C, $T_2 = 90$°C, $T_3 = 110$°C and $T_4 = 100$°C. Upon annealing the viscosity increases due to structural relaxation. If structural relaxation during heating-up to the next annealing temperature is neglected, the viscosity changes along the isoconfigurational states (dashed). At T_4 the viscosity is already too high to observe stress relaxation within experimental time windows. The solid curve corresponds to the equilibrium viscosity $\eta_{eq}(T)$ of the undercooled liquid [Eq. (4.2)].

by the nitric acid, which may have changed the substrate curvature[4]. As the viscosity depends *very sensitively* on the choice of the baseline κ_0 [Eq. (5.13)], the only way to produce useful data was using κ_0 as a fitting parameter at the highest temperature.

The signal-to-noise ratio is lowest for AgInSbTe due to two different facts:

1. The deposition stress of AgInSbTe is positive.
2. The thermal stress $|\frac{\Delta\sigma}{\Delta T}|$ for AgInSbTe is lower than for $Ge_4Sb_1Te_5$ and $Ge_2Sb_2Te_5$ (see Table 6.1).

As a consequence of (1.) and (2.), the amount of compressive stress induced upon heating-up is lowest for AgInSbTe.

Attempts were also made to observe stress relaxation at a temperature T_4 if the sample was annealed *before* at a temperature $T_3 > T_4$ (both temperatures lower than

---

[4] Nitric acid is an oxidizing acid.

the glass temperature T_g determined in Chapter 3.3.) As a result, *no* stress relaxation could be observed at T_4 not even after two days. An explanation for this phenomenon is given in Fig. 6.7, which displays qualitatively the viscosity evolution for a stress relaxation experiment as shown in Figs. 6.4–6.6: Stress relaxation occurs at the annealing temperatures of T_1, T_2 and T_3, accompanied by structural relaxation (i. e. viscosity increase). If the sample is cooled down from T_3 to T_4, the viscosity is already too high to observe stress relaxation within experimental time windows. Therefore, the sample was 'used-up' and could not be used for further stress relaxation experiments. Hence, in order to use a given sample most 'effectively', the sequence of the annealing temperatures had to be taken into account: Stress relaxation had to be measured *first* at the lowest and *last* at the highest annealing temperature, as shown in Figs. 6.4–6.6. Additionally, a meaningful difference between the annealing temperatures had to be chosen. The choice of the annealing temperatures was determined by three points of view:

1. For temperatures below a certain *minimum* annealing temperature T_{min}, stress relaxation cannot be observed within experimental time windows due to the fact that the viscosity is too high.
2. Annealing the sample at elevated temperatures involves the risk of crystallization.
3. The smaller the difference between the annealing temperatures is, the more annealing temperatures are available for one sample. On the other hand, the larger the difference is, the more thermal stress can be induced upon heating to the next annealing temperature and therefore the better is the stress relaxation signal.

After having performed a few test measurements, it turned out that

1. Stress relaxation was only possible to observe for temperatures of 60 °C or higher.
2. In order to minimize crystallization, no annealing temperature higher than 120 °C ($Ge_4Sb_1Te_5$) and 110 °C ($Ge_2Sb_2Te_5$ and AgInSbTe) were applied. No effects ascribable to the onset of crystallization could be observed for these annealing temperatures: For instance, upon cooling down the thermal stress was measured. A partly crystallized sample would have been identified by its higher thermal stress (Table 6.1). Apart from that, crystallization can also be identified by the

stress increase (Figs. 6.1–6.3). Additionally, the wafer curvature setup in Aachen would have measured an increase in the reflectivity signal.

3. The most meaningful difference between two annealing temperatures turned out to be about 20 ℃ or 30 ℃. In this case, a sufficient amount of thermal stress could be induced in order to get a useful signal, and about two or three annealing runs could be measured on each sample (Figs. 6.4–6.6).

A heating rate on the order of 5 K/min was applied during heating to the next annealing temperature.

6.2.2 Viscosity and structural relaxation

The simplest model for viscous flow assumes a time independent viscosity and therefore neglects structural relaxation. Of course, this model is expected to disagree with the experiment, but it gives some important basic insight. Solving Eq. (5.11) yields for $\eta = \text{const}$

$$\sigma(t) = \sigma_0 \cdot \exp\left(-\frac{Y_f}{6\eta}t\right) \tag{6.9a}$$

or

$$\ln\left(\frac{\sigma(t)}{\sigma_0}\right) = -\frac{Y_f}{6\eta}t, \tag{6.9b}$$

where σ_0 is the initial stress at $t = 0$. Therefore, a time independent viscosity implies that $\ln\left(\frac{\sigma(t)}{\sigma_0}\right)$ decreases linearly with time. Figure 6.8 shows a logarithmic representation of Fig. 6.5 at $T = 80$ ℃. Plots for the other temperatures and for $Ge_4Sb_1Te_5$ and AgInSbTe are not shown but look qualitatively similar. According to Fig. 6.8, the slope $\mid \Delta\ln(\frac{\sigma(t)}{\sigma_0})/\Delta t \mid$ is not constant in time but it *decreases* with time. This implies a viscosity that *increases* with time due to structural relaxation [Eq. (6.9b)]. According to Fig. 4.3 a viscosity that increases with time implies that the annealing temperature T is still lower than the glass transition temperature T_g. This is indeed expected if the results presented in Chapter 3.3 are taken into account. For $T > T_g$ the viscosity would be *decreasing* with time.

In order to obtain absolute values for the viscosity, a fitting procedure had to be applied to the stress relaxation data presented in Figs. 6.4– 6.6 or Fig. 6.8. Fitting functions were obtained by solving Eq. (5.11) using physically reasonable models for a

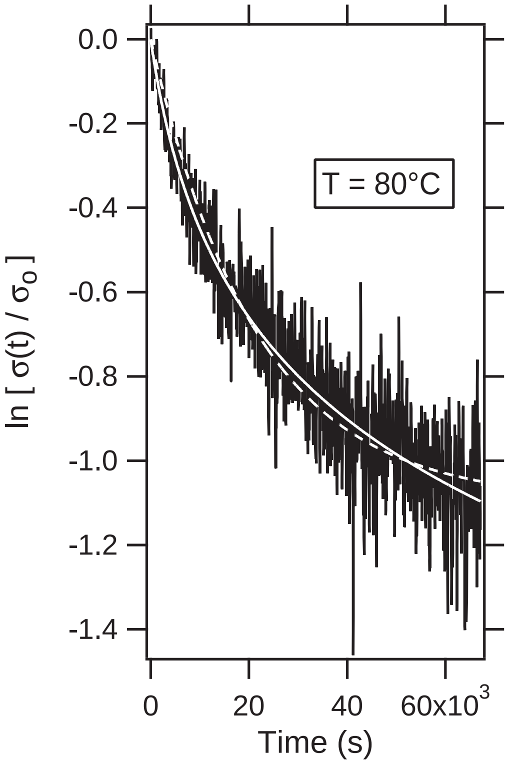

Figure 6.8: Logarithmic plot of Fig. 6.5 for $T = 80$ ℃. The decreasing slope in the data implies a viscosity, which is increasing with time. The data are fitted with a bimolecular [solid line, Eq. (6.10b)] and a unimolecular [dashed line, Eq. (6.10a)] relaxation equation. The fitting parameters for the bimolecular process are $\eta_0 = (5.74 \pm 0.56) \cdot 10^{13}\,\mathrm{Pa\,s}$ and $k = \dot{\eta} = (1.13 \pm 0.03) \cdot 10^{10}\,\mathrm{Pa}$. For the unimolecular process they are $\eta_0 = (9.00 \pm 0.20) \cdot 10^{13}\,\mathrm{Pa\,s}$ and $k_r = (4.66 \pm 0.08) \cdot 10^{-5}\,\mathrm{s}^{-1}$. The errors of the fitting parameters do *not* include the error of the biaxial modulus of the film Y_f (see Figs. 6.9 and 6.10 and the discussion in the text). The bimolecular process fits the data slightly better ($\chi^2_{bimol}/\chi^2_{unimol} = 0.94$).

time-dependent viscosity [i. e. Eqs. (4.16) and (4.19)]. This yielded

a) using $\eta(t)$ from Eq. (4.16a) (i. e. *unimolecular* relaxation *far away* from equilibrium)

$$\ln\left(\frac{\sigma(t)}{\sigma_0}\right) = -\frac{Y_f}{6k_r\eta_0}\left[1-\exp\left(-k_r t\right)\right], \tag{6.10a}$$

b) using $\eta(t)$ from Eq. (4.16b) (i. e. *bimolecular* relaxation *far away* from equilibrium)

$$\ln\left(\frac{\sigma(t)}{\sigma_0}\right) = -\frac{Y_f}{6k}\ln\left(1+\frac{k}{\eta_0}t\right), \tag{6.10b}$$

c) using $\eta(t)$ from Eq. (4.19a) (i. e. *unimolecular* relaxation *close to* equilibrium)

$$\ln\left(\frac{\sigma(t)}{\sigma_0}\right) = -\frac{Y_f}{6\eta_{eq}}\left\{t+\frac{\eta_{eq}-\eta_0}{k_r\eta_0}\cdot\left[1-\exp(-k_r t)\right]\right\}, \tag{6.10c}$$

d) using $\eta(t)$ from Eq. (4.19b) (i. e. *bimolecular* relaxation *close to* equilibrium)

$$\ln\left(\frac{\sigma(t)}{\sigma_0}\right) = -\frac{Y_f}{6}\cdot\left\{\frac{1}{k}\cdot\ln\left[1+\left(\frac{1}{\eta_0}-\frac{1}{\eta_{eq}}\right)\cdot kt\right]+\frac{t}{\eta_{eq}}\right\}, \tag{6.10d}$$

e) and using $\eta(t)$ from Eq. (4.19c) (i. e. *'intermediate'* relaxation *close to* equilibrium)

$$\ln\left(\frac{\sigma(t)}{\sigma_0}\right) = -\frac{Y_f}{6k}\cdot\ln\left\{1+\left[\exp\left(\frac{k}{\eta_{eq}}t\right)-1\right]\cdot\frac{\eta_{eq}}{\eta_0}\right\}. \tag{6.10e}$$

Fitting parameters are η_0, η_{eq}, k, k_r, σ_0 and the baseline $\sigma_{base} = \frac{1}{6}Y_s\frac{d_s^2}{d_f}\kappa_0$. The latter is not included in Eqs. (6.10a)–(6.10e). There are *four* fitting parameters in Eqs. (6.10a) and (6.10b). In contrast, Eqs. (6.10c), (6.10d) and (6.10e) exhibit *five* fitting parameters, as the equilibrium viscosity η_{eq} is an additional one.

The stress relaxation data were fitted for all annealing temperatures applied and all samples investigated. Equations (6.10a)–(6.10e) were used as fitting functions. A data analysis program based on the method of least squares was employed [21]. However, σ_{base} was only used as a fitting parameter at the *highest* annealing temperature of each sample. Subsequently, the result for σ_{base} was used as a fixed baseline for the fits to the stress data at lower temperatures. Figure 6.8 shows the fits obtained from Eqs. (6.10a) and (6.10b). The latter equation fitted the data slightly better than the former. These two fits differ only slightly ($\chi^2_{bimol}/\chi^2_{unimol} = 0.94$) because the viscosity is increasing with time only very slowly. The fit obtained from Eq. (6.10c) ended up exactly on top of the fit obtained from Eq. (6.10a). (This means, that the same fitting parameters η_0,

k_r and σ_0 were obtained in both cases.) In the same way, the fits obtained from both Eq. (6.10d) and (6.10e) ended up exactly on top of the fit obtained from Eq. (6.10b). (The same fitting parameters were obtained for η_0, k and σ_0 in all three cases.) The fitting parameters for the equilibrium viscosity η_{eq} were extremely large (several orders of magnitude higher than the initial viscosity η_0). Therefore, the equilibrium fits were mathematically *identical* to the non-equilibrium fits: For $\eta_{eq} \rightarrow \infty$, Eq. (6.10d) trends towards Eq. (6.10a). In the same way, both Eqs. (6.10d) and (6.10e) trend towards Eq. (6.10b) for $\eta_{eq} \rightarrow \infty$. Hence, it can be concluded that the glass is still far away from equilibrium. For the case of the bimolecular equation [Eq. (6.10b)], *parts* of the data were fitted *additionally* for comparison. This yielded approximately the same fitting parameters k and η_0, which confirms the fact that Eq. (6.10b) indeed fits the data correctly.

The procedure described in the last paragraph was performed for all annealing temperatures, all samples and all three Te alloys. The result was always the same: the bimolecular equation [Eq. (6.10b)] was found to fit the data slightly better than the unimolecular equation [Eq. (6.10a)]; and the equilibrium equations [Eq. (6.10c)–(6.10e)] could not reduce the χ^2 and yielded the same fitting parameters. Fitting parts of the curve always yielded approximately the same fitting parameters η_0 and k if Eq. (6.10b) was used. *Due to this overall consistency it can be concluded that structural relaxation is bimolecular rather than unimolecular for all three alloys, i. e. the viscosity increases linearly with time.* In fact, the observation of *bimolecular* relaxation kinetics was reported in several studies on other amorphous materials [7, 41, 44, 47, 48, 35]. However, it remains an open question how the recombining flow defects look like. According to [30], they are probably a 'mixture' of dangling bonds and free volume fluctuations.

It can also be concluded that the annealing temperatures applied for the stress relaxation experiments are still far below the glass transition temperature, which is also confirmed by the DSC measurements (Chapter 3.3).

Due to the fact that structural relaxation is bimolecular and far away from equilibrium, the fitting parameter k can be interpreted as a constant viscosity increase rate $\dot{\eta}$ [Eqs. (4.16b) and (4.17)]. Therefore, $k \equiv \dot{\eta}$ hereafter. $\dot{\eta}$ is the *only specific* quantity that can be used to describe the viscosity quantitatively. In contrast, the fitting parameter for the initial viscosity η_0 is *not* a specific quantity for the corresponding alloy at the corresponding temperature because it depends on the choice of the zero point of time t_0: the viscosity is increasing with time continuously. $\dot{\eta}$ is expected to exhibit Arrhenius temperature dependence [Eqs. (4.20) and (4.21)]. Figure 6.9 displays the fitting parameter $\dot{\eta}$ as a function of annealing temperature. Results were taken from several measurements and different samples. Each connected 'group' of one to four points result from the same sample. As $\dot{\eta}$ is proportional to the biaxial modulus of the film Y_f in these measurements [like all other parameters which describe the viscosity, see Eq. (5.13)], an uncertainty in Y_f only induces a constant shift of the entire 'material group'[5] in the *logarithmic* plot. Hence, error bars, which include uncertainties in Y_f, are not assigned to each data point but are plotted at the right side of the graph next to the material group. On the other hand, errors in the fitting parameter $\dot{\eta}$ are obviously different for each data point. However, due to the logarithmic representation of the data these error bars are smaller than the plotted points in Fig. 6.9 and are therefore not shown. Curves that describe different groups within one material group are obviously expected to lie on top of each other as a unique function $\dot{\eta}(T)$ is expected for each phase change material. In Fig. 6.9 this is not the case; each sample behaved slightly differently.

The viscosity increase rate $\dot{\eta}$ is highest for $Ge_4Sb_1Te_5$ and lowest for AgInSbTe at all temperatures. However, this difference in $\dot{\eta}$ is not apparent in Figs. 6.4–6.6: these stress relaxation curves look rather similar for all three alloys. Taking a look at Eq. (6.10b) reveals the solution: The 'real' quantities, which describe the shape of the stress relaxation curves *in these experiments*, are the *ratios* $Y_f/\dot{\eta}$ and $\dot{\eta}/\eta_0$ rather than the values η_0 and $k = \dot{\eta}$ themselves. Stress relaxation in Figs. 6.4–6.6 looks roughly similar because the *ratios* $Y_f/\dot{\eta}$ and $\dot{\eta}/\eta_0$ are similar for all three alloys. Due to the fact that Y_f is highest (lowest) for $Ge_4Sb_1Te_5$ (AgInSbTe) [Table 6.1], the parameters $\dot{\eta}$ and η_0 are also highest (lowest) for this alloy[6]. However, there is no exact scaling between $\dot{\eta}$ and Y_f: According to Table 6.1, Y_f for $Ge_4Sb_1Te_5$ and $Ge_2Sb_2Te_5$ are rather similar. In contrast, $\dot{\eta}$ of $Ge_4Sb_1Te_5$ is more than two times higher than for $Ge_2Sb_2Te_5$ (Fig. 6.9).

---

[5] All data points, which result from the same phase change material are called 'material group' hereafter. All data points, which result just from one sample are called 'group'.

[6] The values for η_0 are discussed in Chapter 6.2.3

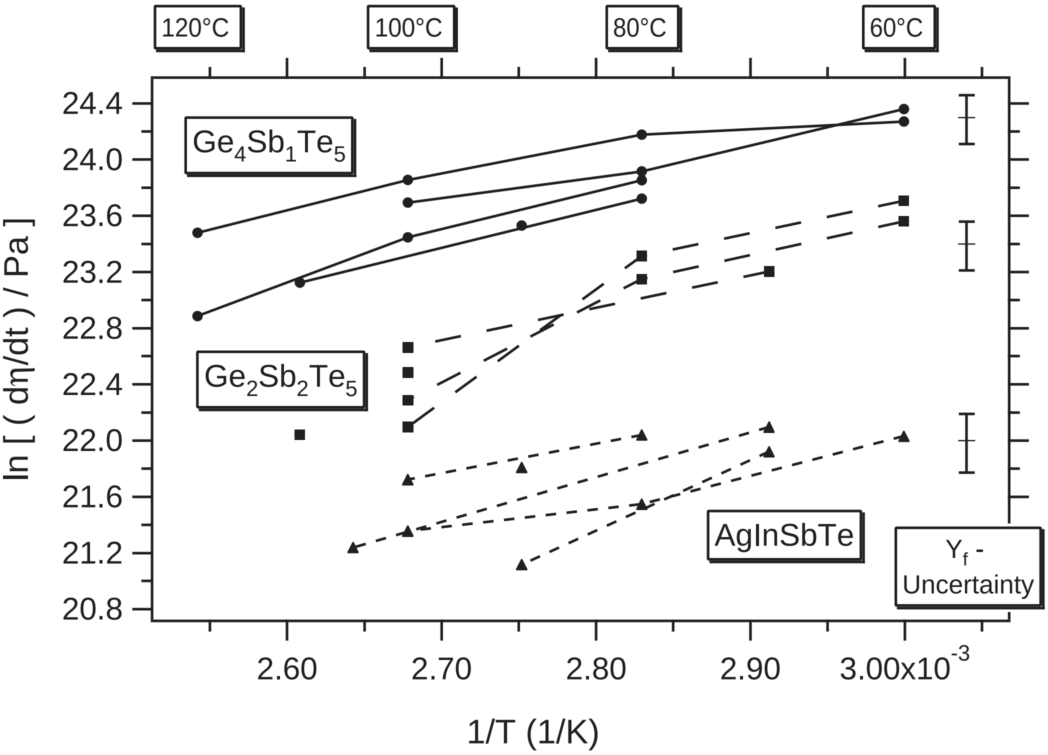

Figure 6.9: Fitting parameter $\dot{\eta}$ as a function of temperature in Arrhenius representation for three Te alloys. Each connected group of points originate from the same sample. The solid lines (circles) represent $Ge_4Sb_1Te_5$, the dashed lines (squares) $Ge_2Sb_2Te_5$ and the dotted lines (triangles) AgInSbTe. The error bars at the right side of the graph correspond to the error in the biaxial modulus of the film Y_f.

Table 6.3: Fitting parameters A and $Q_{\dot{\eta}}$ for the viscosity increase rate $\dot{\eta}$ in Fig. 6.9 [fitting function: Eq. (6.11a)]. The errors of the fitting parameters A *do* include the error of the biaxial modulus of the film Y_f. In contrast, the values for $Q_{\dot{\eta}}$ (including their errors) are *independent* of Y_f (see the discussion in the text).

	A	$Q_{\dot{\eta}}$ (eV)
$Ge_4Sb_1Te_5$	16.84 ± 1.34	0.22 ± 0.04
$Ge_2Sb_2Te_5$	11.66 ± 1.51	0.35 ± 0.04
AgInSbTe	15.57 ± 2.27	0.19 ± 0.06

The relation between $\ln(\dot{\eta})$ and $1/T$ is roughly linear for each connected group of points (each sample)[7]. Hence, the temperature dependence of $\dot{\eta}$ is Arrhenius, as predicted by Eqs. (4.20) and (4.21). The linear fitting procedure

$$\ln\left(\frac{\dot{\eta}}{\mathrm{Pa}}\right) = A + Q_{\dot{\eta}} \cdot \frac{1}{k_B T} \tag{6.11a}$$

($Q_k \equiv Q_{\dot{\eta}}$ hereafter) was applied to each material group in Fig. 6.9. Comparing with Eq. (4.20), the parameter A is given by

$$A = \ln\left(\frac{1}{\mathrm{Pa}} \cdot \frac{k_B T}{(\gamma_0 \nu_0)^2} \cdot \frac{k_r^0}{k_f^0}\right). \tag{6.11b}$$

The fitting parameters A and $Q_{\dot{\eta}}$ are given in Table 6.3. The activation energy $Q_{\dot{\eta}}$ is on the same order of magnitude for all three phase change materials, though it is slightly higher for $Ge_2Sb_2Te_5$.

6.2.3 Isoconfigurational Activation Energy

Figure 6.10 displays the initial and the final viscosity for three annealing temperatures of $T_1 = 60\,°\mathrm{C}$, $T_2 = 80\,°\mathrm{C}$ and $T_3 = 100\,°\mathrm{C}$ for one sample per phase change material. This allows a tracking of the viscosity evolution with time over the duration of the entire

---

[7] There is not enough data to claim a non-linear relation for sure. A simple linear approximation is the best that can be done here.

experiment (compare with Fig 6.7). Similar to Fig. 6.9, an uncertainty in Y_f only leads to a shift of the entire group in the logarithmic plot, therefore the corresponding error bars are mapped next to the group. Due to the logarithmic representation, the errors of the fitting quantities (initial and final viscosity) are much smaller than the plotted points and are therefore not shown.

When the sample is heated from T_1 to T_2 or from T_2 to T_3 the film viscosity undergoes two *simultaneous* developments:

(a) isoconfigurational change (viscosity *decrease*), i. e. a change along the straight lines in Figs. 4.3 or 6.7

(b) structural relaxation (viscosity *increase*).

If no structural relaxation occurred during heating-up, the slope of the straight lines (as indicated in Fig. 6.10) would be equal to Q_{iso}/k_B. However, structural relaxation during heating-up has to be considered and the numbers obtained from these slopes have to be corrected. This was achieved by a computer simulation [35, 47, 48], which takes into account *both* the isoconfigurational change (a) *and* structural relaxation (b) during heating-up: The heating process was simulated by splitting it in intervals a_i and b_i (Fig. 6.11). The duration of interval i, which includes both path a_i and b_i, is Δt. During path a_i, the change in the viscosity is given by

$$\eta(t) \rightarrow \eta(t) \cdot \exp\left[\frac{Q_{iso}}{k_B} \cdot \left(\frac{1}{T(t+\Delta t)} - \frac{1}{T(t)}\right)\right]. \tag{6.12a}$$

During path b_i the viscosity change is

$$\eta(t) \rightarrow \eta(t) + \dot{\eta}(T(t+\Delta t)) \cdot \Delta t. \tag{6.12b}$$

Therefore, the total viscosity change during the time interval Δt is obtained by combining Eqs. (6.12a) and (6.12b):

$$\eta(t+\Delta t) = \eta(t) \cdot \exp\left[\frac{Q_{iso}}{k_B} \cdot \left(\frac{1}{T(t+\Delta t)} - \frac{1}{T(t)}\right)\right] + \dot{\eta}(T(t+\Delta t)) \cdot \Delta t. \tag{6.13}$$

The function $T(t)$ during heating-up was monitored by the computer, which was connected to the wafer curvature setup. $\dot{\eta}(T)$ is known from Eq. (6.11a) and Table 6.3. Q_{iso} was handled as a fitting parameter in order to match the *measured* viscosities

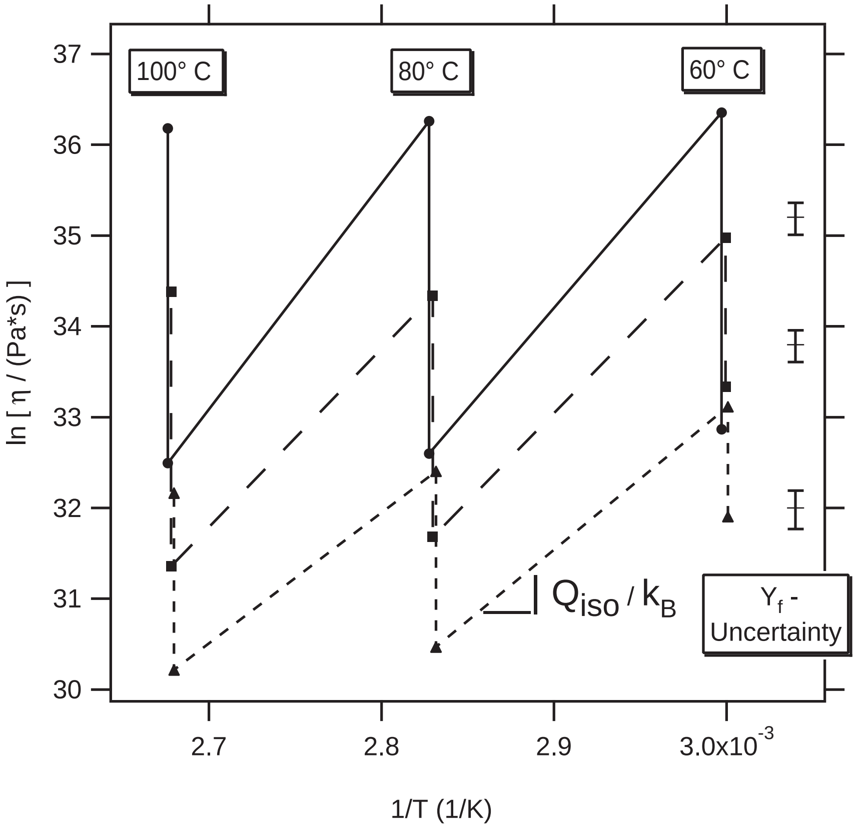

Figure 6.10: Arrhenius plot of initial and final viscosity for three different annealing temperatures of $T_1 = 60\,°\mathrm{C}$, $T_2 = 80\,°\mathrm{C}$ and $T_3 = 100\,°\mathrm{C}$. The duration of the annealing runs was between one and two days. For comparison with Fig. 6.5 and Table 6.4, the sample numbers are '2-415-24' ($Ge_4Sb_1Te_5$, solid line, circles) , '4-225-36' ($Ge_2Sb_2Te_5$, dashed line, squares) and '8-ag-37' (AgInSbTe, dotted line, triangles). The slope of the line connecting the final viscosity at T_1 (T_2) with the initial viscosity at T_2 (T_3) is equal to the isoconfigurational activation energy Q_{iso}/k_B if structural relaxation during heating-up is neglected. This slope (i. e. Q_{iso}) is highest for $Ge_4Sb_1Te_5$ and lowest for AgInSbTe. The error bars at the right side of the graph correspond to the error in the biaxial modulus of the film Y_f.

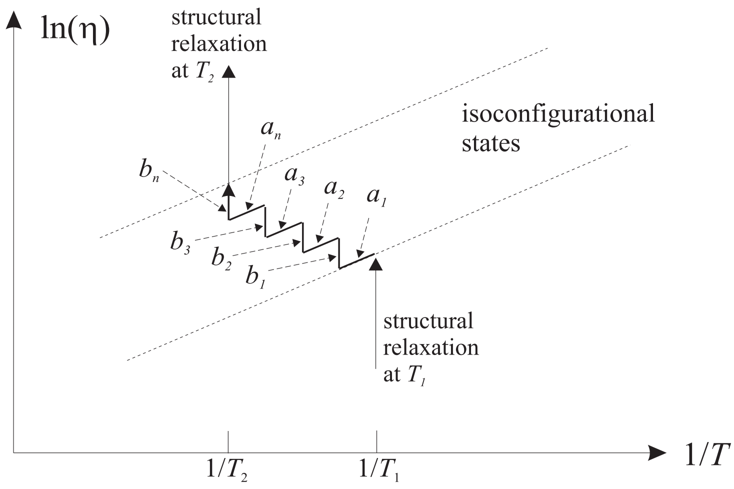

Figure 6.11: *Simultaneous* isoconfigurational viscosity change and structural relaxation during heating-up from T_1 to T_2 is approximated in a computer simulation by *successively* considering isoconfigurational change (a_i) and structural relaxation (b_i) during short time intervals.

at the beginning and the end of each heating-up process. The length of the fitting interval Δt was decreased until no change in the fitting parameter Q_{iso} was observed any more.

Table 6.4 shows the results for several samples. The correction for Q_{iso} due to structural relaxation during heating-up was of order of 0.1 eV for all samples and temperatures. Therefore, isoconfigurational change is still the dominant mechanism upon heating-up. The samples marked with an asterisk ($*$) were measured using the wafer curvature setup in Aachen. The other samples were measured in Harvard. According to Table 6.4, the samples measured in Aachen exhibit a viscosity, which is about an order of magnitude lower than the viscosity of the samples measured in Harvard. This is interesting because it shows once again the important connection between structural relaxation and sample aging: At the date of the measurement, the samples measured in Aachen were about one or two days old. In contrast, the samples measured in Harvard were several months old, due to the fact that they were prepared in Aachen. Due to the low viscosity of the samples measured in Aachen, the stress relaxation experiments could be performed much quicker: An annealing time of only a few hours was already sufficient in order to obtain a usable stress relaxation signal. In contrast, annealing times of more than one day had to be applied in Harvard in order to obtain a usable signal.

Q_{iso} was assumed to be temperature independent[8], which is also theoretically expected from Eq. (4.9). Average values for Q_{iso} from all samples and temperatures are shown in Table 6.5. The ratio $\frac{Q_{iso}}{k_B T_m}$ (T_m is the peak melting temperature from Table 3.2) is roughly equal for all materials. Table 6.5 also shows the activation energy Q_{rel} of the rate equation constant k_r, obtained from Eq. (4.21). Q_{rel} also roughly scales with T_m. The scaling of Q_{iso} and Q_{rel} with T_m is interesting: In solid state physics many processes are thermally activated and exhibit activation energies, which scale with the melting temperature T_m.

6.2.4 Simulation of the viscosity evolution upon heating-up of an as-deposited sample

The knowledge of $\dot{\eta}(T)$ and Q_{iso} (Table 6.3 and 6.5) makes it possible to perform a simulation of the viscosity evolution upon heating-up of an as-deposited amorphous sample from room temperature to the peak crystallization temperature $T_{c,p}$, which takes into account the isoconfigurational change and the structural relaxation during heating. The simulation is based on Eq. (6.13). As the initial viscosity at room temperature is not known, and as it also depends on the age of the sample due to structural relaxation, it was varied over several orders of magnitude. Figures 6.12–6.14 show the results. The simulations are based on a *linearly increasing* viscosity according to the results of Table 6.3. Equilibrium effects close to the glass transition temperature T_g had to be neglected. Below about 100 ℃, the viscosity decreases over several orders of magnitude upon heating-up. In this temperature range, structural relaxation seems to be negligible, so that the viscosity change is isoconfigurational. Above around 100 ℃, structural relaxation becomes important and the viscosity adopts roughly a constant value, i. e. it decreases only slightly upon further heating. Obviously, the viscosity evolution above 100 ℃ depends on the heating rate $\dot{T}$: a higher heating rate allows less time for structural relaxation, and the viscosity is lower. Figure 6.15 displays the value of the viscosity $\eta_c := \eta(T_{c,p})$ at the peak crystallization temperature[9] $T_{c,p}$ as a

---

[8] There is not enough data available to claim a temperature dependence.

[9] From Table 3.1

Table 6.4: Isoconfigurational activation energy Q_{iso} for three amorphous Te alloys, determined during heating-up (heating rate $\dot{T}$) by matching the *measured* viscosity η_1 at the *end* of anneal run at temperature T_1 and the *measured* viscosity η_2 at the *beginning* of anneal run at T_2.

Sample	T_1 (℃)	η_1 (Pa s)	T_2 (℃)	η_2 (Pa s)	$\dot{T}$ (K min^{-1})	Q_{iso} (eV)
(a) $Ge_4Sb_1Te_5$						
7-415-08	80	$1.5 \cdot 10^{15}$	110	$2.4 \cdot 10^{13}$	5	1.68
3-415-32	80	$4.4 \cdot 10^{14}$	100	$2.9 \cdot 10^{13}$	3	1.67
	100	$3.0 \cdot 10^{14}$	120	$2.0 \cdot 10^{13}$	3	1.81
2-415-24	60	$6.1 \cdot 10^{15}$	80	$1.4 \cdot 10^{14}$	3	2.00
	80	$5.6 \cdot 10^{15}$	100	$1.3 \cdot 10^{14}$	3	2.20
	100	$5.2 \cdot 10^{15}$	120	$9.4 \cdot 10^{13}$	2	2.53
4-415-43	60	$3.7 \cdot 10^{15}$	80	$1.1 \cdot 10^{14}$	5	1.86
	80	$2.2 \cdot 10^{15}$	100	$1.1 \cdot 10^{14}$	5	1.75
9-415-47	70	$1.9 \cdot 10^{15}$	100	$2.4 \cdot 10^{13}$	5	1.92
(b) $Ge_2Sb_2Te_5$						
3-225-23	60	$3.6 \cdot 10^{15}$	80	$1.0 \cdot 10^{14}$	2	1.85
	80	$2.1 \cdot 10^{15}$	100	$7.6 \cdot 10^{13}$	3	1.91
4-225-36	60	$1.6 \cdot 10^{15}$	80	$5.7 \cdot 10^{13}$	4	1.75
	80	$8.2 \cdot 10^{14}$	100	$4.1 \cdot 10^{13}$	4	1.72
6-225-46	70	$1.1 \cdot 10^{15}$	100	$1.8 \cdot 10^{13}$	5	1.59
(c) AgInSbTe						
9-ag-38	80	$2.3 \cdot 10^{14}$	100	$1.4 \cdot 10^{13}$	5	1.63
8-ag-37	60	$2.4 \cdot 10^{14}$	80	$1.7 \cdot 10^{13}$	5	1.38
	80	$1.2 \cdot 10^{14}$	100	$1.3 \cdot 10^{13}$	5	1.30
1-ag-45	70	$2.0 \cdot 10^{14}$	90	$1.5 \cdot 10^{13}$	5	1.44
16-ag-90 (∗)	70	$3.3 \cdot 10^{13}$	105	$1.0 \cdot 10^{12}$	5	1.26
17-ag-91 (∗)	70	$1.8 \cdot 10^{13}$	90	$3.4 \cdot 10^{12}$	5	0.97

Table 6.5: Average values for the isoconfigurational activation energy Q_{iso} for the viscosity η and the activation energy Q_{rel} of the rate equation constant k_r, and melting temperatures T_m determined from differential scanning calorimetry measurements (Table 3.2).

	Q_{iso} (eV)	Q_{rel} (eV)	T_m (℃)	$\frac{Q_{iso}}{k_B T_m}$	$\frac{Q_{rel}}{k_B T_m}$
$Ge_4Sb_1Te_5$	1.94 ± 0.09	1.72 ± 0.13	685 ± 5 [a]	23.4 ± 1.3	20.8 ± 1.7
$Ge_2Sb_2Te_5$	1.76 ± 0.05	1.42 ± 0.09	621 ± 5	22.9 ± 0.8	18.4 ± 1.3
AgInSbTe	1.33 ± 0.09	1.14 ± 0.15	537 ± 5	19.0 ± 1.4	16.3 ± 2.3

[a] This number was estimated from Ref. [23].

function of heating rate[10] as obtained from the computer simulation. The viscosity η_c is inversely proportional to the heating rate $\dot{T}$ due to the *linear* viscosity increase with time (bimolecular relaxation kinetics). A heating rate, which is twice as large allows only half as much time for structural relaxation and therefore results in a viscosity value, which is a factor of two lower[11]. $Ge_4Sb_1Te_5$ (AgInSbTe) exhibits the largest (smallest) values for η_c because its viscosity increase rate $\dot{\eta}$ is largest (smallest).

---

[10] The heating rate dependence of the peak crystallization temperature $T_{c,p}$ had to be considered here [Eq. (3.2)].

[11] The heating rate dependence of $T_{c,p}$ did not affect this result. This is due to the fact that the viscosity approaches a roughly constant value above about 100 ℃. Therefore, a shift in $T_{c,p}$ obtained from Eq. (3.2) affects the magnitude of η_c only very slightly.

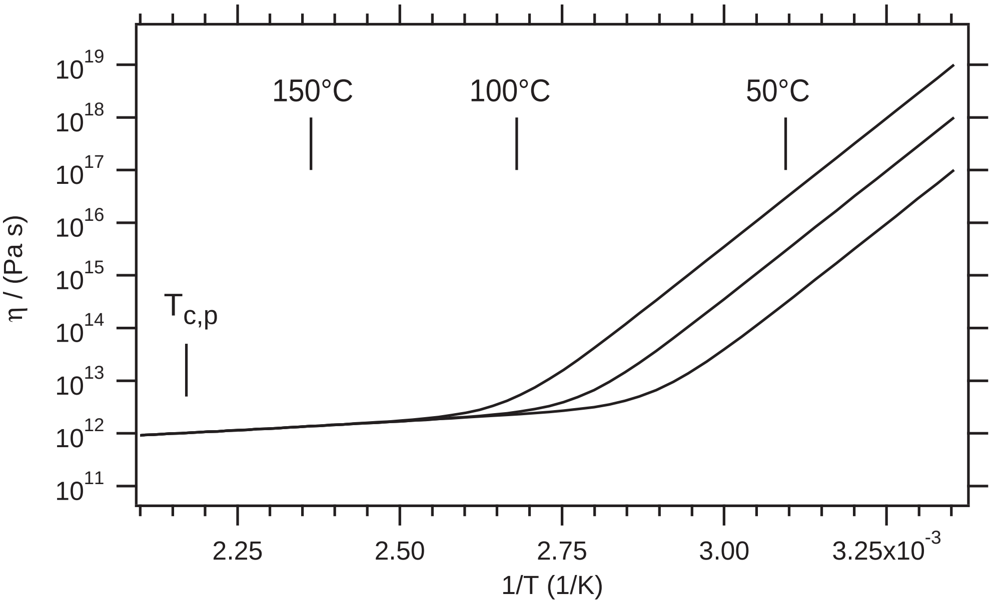

Figure 6.12: Computer simulation of the viscosity evolution of an as-deposited $Ge_4Sb_1Te_5$ thin film upon heating-up (3 K/min). At the crystallization temperature $T_{c,p}$, the value for the viscosity is independent of the value assumed for the initial viscosity at room temperature.

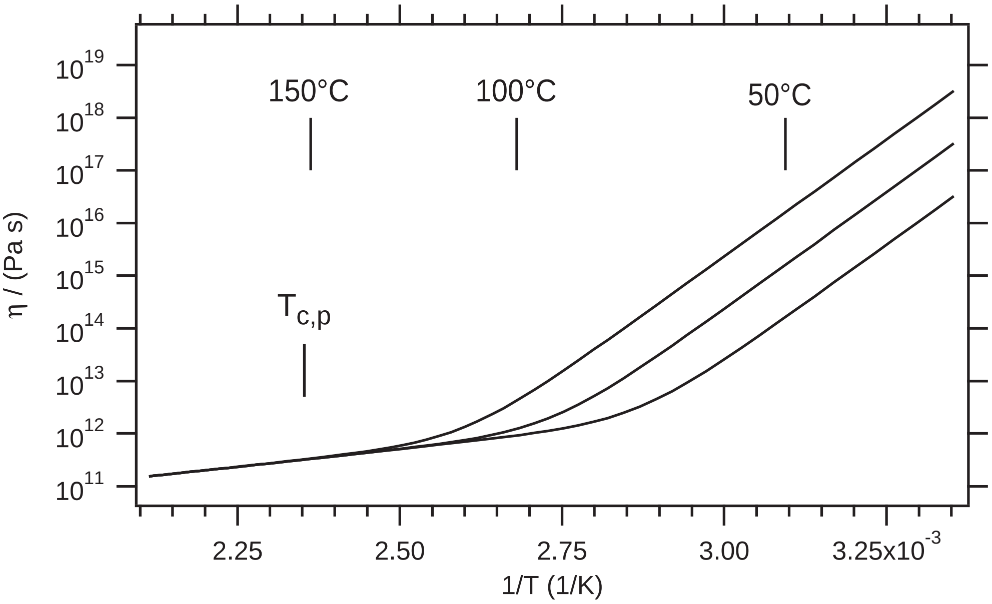

Figure 6.13: Computer simulation of the viscosity evolution of an as-deposited $Ge_2Sb_2Te_5$ thin film upon heating-up (3 K/min).

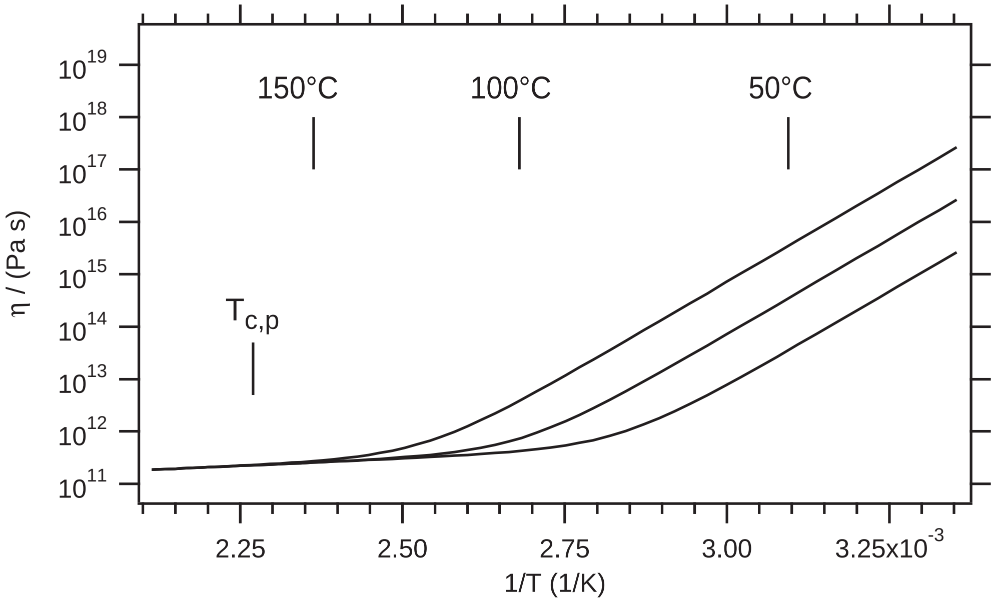

Figure 6.14: Computer simulation of the viscosity evolution of an as-deposited AgInSbTe thin film upon heating-up (3 K/min).

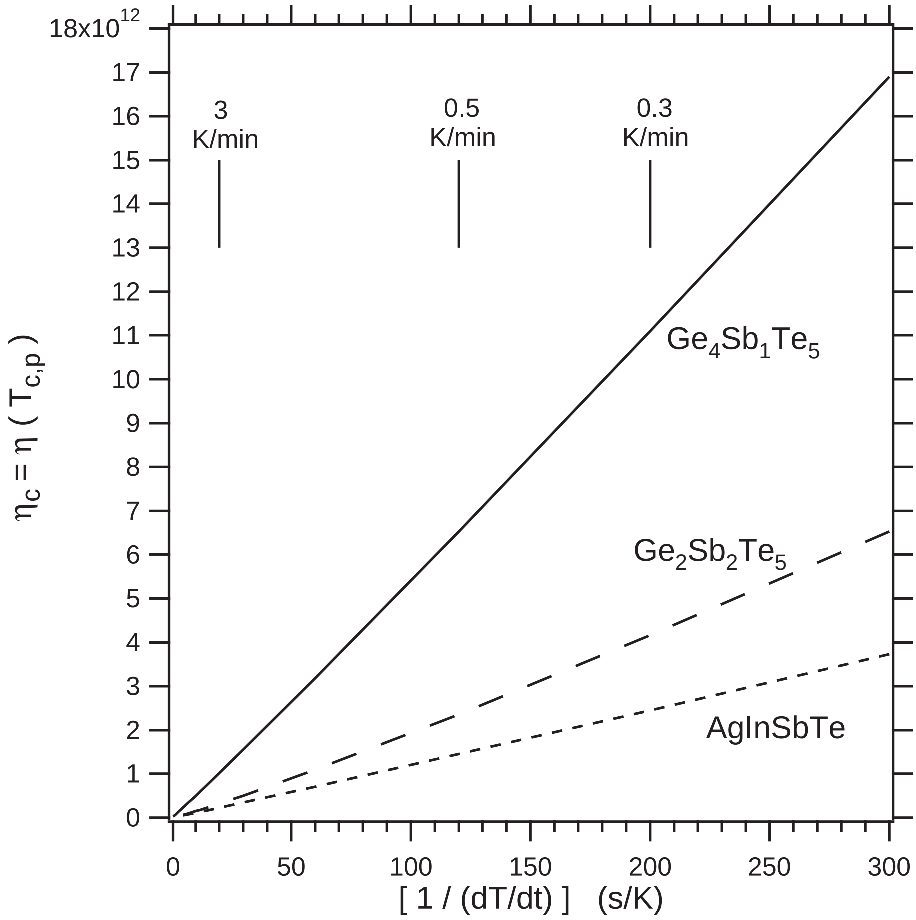

Figure 6.15: Viscosity $\eta_c := \eta(T_{c,p})$ at the peak crystallization temperature $T_{c,p}$ as a function of heating rate $\dot{T}$ for $Ge_4Sb_1Te_5$ (smooth), $Ge_2Sb_2Te_5$ (dashed) and AgInSbTe (dotted), obtained from a computer simulation. $T_{c,p}$ as a function of heating rate is known from DSC measurements (Table 3.1) and from the activation energy of crystallization (Table 3.4).

Chapter 7

Results and discussion: Stresses upon crystallization

7.1 Experimentally observed stress and reflectivity increase

As already mentioned in Chapter 6.1, crystallization of the as-deposited amorphous films is accompanied by a large stress increase, which is due to the fact that the film densifies upon crystallization. This *density increase* $\frac{\Delta\rho}{\rho} > 0$ induces a *film volume decrease* $\frac{\Delta V}{V} < 0$. As the film is constrained by the substrate, a *film thickness decrease* $\epsilon_{zz,\text{total}} < 0$ is the consequence. This film thickness decrease has been measured in x-ray reflectivity (XRR) measurements [19, 20, 13]. Results are given in Table 7.1. Within range of error, $(-\epsilon_{zz,\text{total}})$ is equal to the density increase $\frac{\Delta\rho}{\rho}$, which is also obtained independently[1] from XRR measurements. Therefore, mass conservation is ensured. Due to the densification, a *tensile* stress upon crystallization is expected.

Figure 7.1 displays the stress as a function of temperature for a $Ge_2Sb_2Te_5$ sample. The heating rate was 20 K/min. Before looking at the stress increase $\Delta\sigma$ at the crystallization temperature more closely, the amorphous phase is discussed briefly. Two things affect the stress evolution *simultaneously* below about 180 ℃: thermal stress

---

[1] The technique of XRR measurements has been described in Ref. [58]: The density ρ of the film is obtained from the position of the angle of total reflectance. The film thickness is obtained from the angular distance of the maxima in the interference pattern.

[Eq. (6.1)] and viscous flow [Eq. (5.11)]. For temperatures below about 120 ℃, the former effect dominates as the viscosity is still very high (Fig. 6.13). The relation between stress and temperature is linear in this regime according to Table (6.1). Between 120 ℃ and 180 ℃, the latter effect dominates due to the decreasing viscosity with increasing temperature (Fig. 6.13). The stress evolution upon heating below 180 ℃ was checked by a computer simulation based on Eqs. (6.1) and (5.11):

$$\sigma(t+\Delta t) = [\sigma(t) + Y_f(\alpha_s - \alpha_f)\dot{T}\Delta t] \cdot \exp\left(-\frac{Y_f \Delta t}{6\eta}\right) \tag{7.1}$$

The viscosity η upon heating was obtained from Fig. 6.13. The time interval Δt was decreased until no further change in the simulation curve was noticed any more. The simulation curve coincided approximately with the stress data below 180 ℃ (not shown).

For the other two alloys ($Ge_4Sb_1Te_5$ and AgInSbTe), the stress evolution below the crystallization temperature looks qualitatively similar and is therefore not shown. The computer simulation yielded a stress evolution, which coincided approximately with the measured stress data in the amorphous phase also for these two alloys.

The experimentally observed stress increase upon crystallization $\Delta\sigma_{\mathrm{exp}}$ is given in Table 7.1 for all three alloys (compare also with Figs. 6.1–6.3). In the crystalline phase (Fig. 7.1), no stress signal is visible that could originate from the cubic-to-hexagonal transformation (see Chapter 3.1.3).

Figure 7.1 also displays the sample reflectivity as a function of temperature. Upon crystallization, the reflectivity increases. However, above 340 ℃, the reflectivity decreases again, which is due to film evaporation. At 400 ℃, the film is completely evaporated. This is confirmed by three facts:

1. The reflectivity signal upon heating between 400 ℃ and 420 ℃ *and* upon cooling down (not entirely shown) is equal to the reflectivity signal of a pure Si wafer (i. e. a level of about 2.9).
2. The stress remained equal to zero upon cooling down from 420 ℃ to 30 ℃ (not entirely shown).
3. After opening the chamber and taking out the sample no film was left on the substrate.

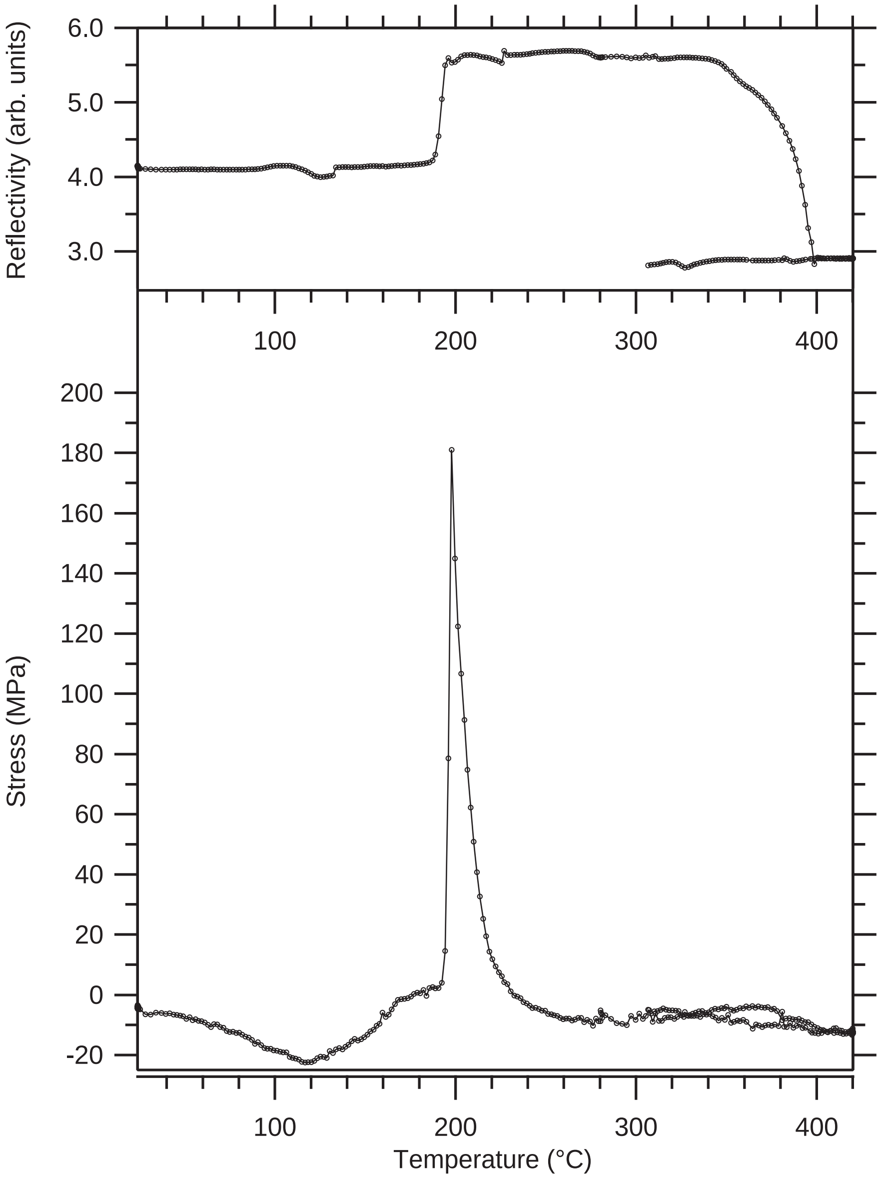

Figure 7.1: Stress and reflectivity as a function of temperature for $Ge_2Sb_2Te_5$. Heating and cooling rate: 20 K/min. Film thickness: 1000 nm. Substrate: 200 µm Silicon (cleaned before deposition). Wafer curvature setup: Aachen. Sample age: 1 hour.

Table 7.1: Crystallization of Te alloys: Film thickness decrease $\epsilon_{zz,\mathrm{total}}$ due to densification, experimentally observed stress increase $\Delta\sigma_{\mathrm{exp}}$, and theoretically estimated stress increase $\Delta\sigma_{\mathrm{elast}}$ for an *elastic* process.

	$\epsilon_{zz,\mathrm{total}}$ [a] (%)	$\Delta\sigma_{\mathrm{exp}}$ (MPa)	$\Delta\sigma_{\mathrm{elast}}$ [b] (MPa)	$\Delta\sigma_{\mathrm{elast}}$ [c] (MPa)
$Ge_4Sb_1Te_5$	-(9.0 ± 0.3)	240 ± 20	1640 ± 520	3020 ± 970
$Ge_2Sb_2Te_5$	-(6.5 ± 0.2)	190 ± 20	970 ± 310	1580 ± 520
AgInSbTe	-(5.5 ± 0.2)	130 ± 20	310 ± 110	670 ± 240

[a] from Refs. [19], [20] and [13]
[b] using the biaxial modulus Y_f of the *amorphous* phase
[c] using the biaxial modulus Y_f of the *crystalline* phase (Table 6.1)

Therefore, the film evaporated already more than 200 ℃ below the thermodynamic melting temperature (Table 3.2).

For the other two alloys ($Ge_4Sb_1Te_5$ and AgInSbTe), a reflectivity increase of the same order is observed upon crystallization. However, samples of these two alloys were not heated to temperatures higher than 270 ℃. Therefore, a statement on evaporation cannot be made for them.

The experimentally observed stress increase upon crystallization $\Delta\sigma_{\mathrm{exp}}$ (Table 7.1) is *independent* of *film thickness*, *substrate material* and *heating rate* for all three alloys. (Films with thicknesses between 70 nm and 1000 nm were measured. 200 µm Si substrates and 265 µm Al_2O_3 substrates were used. Heating rates between 0.2 K/min and 100 K/min were applied.) Furthermore, one obtains the same stress increase upon *isothermal*[2] crystallization.

7.2 Theoretically expected stress increase for an elastic process

In order to compare the experimentally observed stress increase $\Delta\sigma_{\mathrm{exp}}$ (Table 7.1) with the stress increase $\Delta\sigma_{\mathrm{elast}}$, which is theoretically expected for an *elastic* film volume

---

[2] This will be discussed in more detail in Chapter 7.4.2

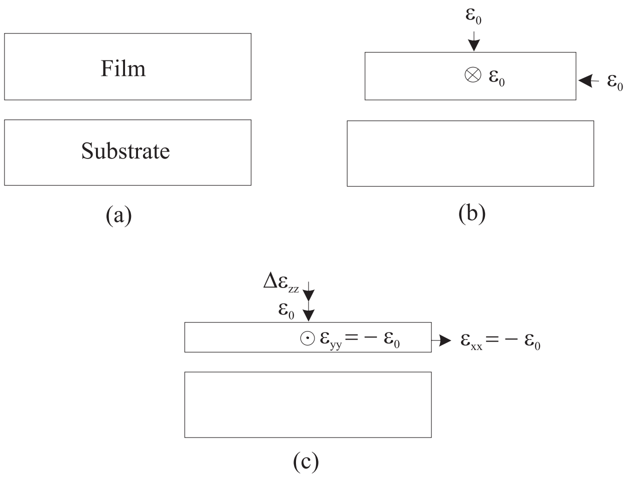

Figure 7.2: Gedanken experiment to calculate the elastic stress increase upon film densification. (a) The film is free of stress and is removed from the substrate. (b) The film densifies isotropically. (c) The film is strained biaxially in order to match the substrate area again.

change upon crystallization, a 'Gedanken experiment' is performed [59]: The film is thought to be removed from the substrate (Fig. 7.2 a). Upon crystallization, the density increases, which leads to an isotropic and elastic volume change (Fig. 7.2 b):

$$\frac{\Delta V}{V} = \text{trace}\ \underline{\underline{\epsilon}} = 3\epsilon_0, \qquad \text{where } \epsilon_0 < 0. \tag{7.2}$$

In order to fix the film to the substrate again, it has to be strained biaxially by $\epsilon_{xx} = -\epsilon_0 > 0$ in order to match the substrate area again (Fig. 7.2 c). The elastic stress $\Delta\sigma_{\text{elast}}$, which is necessary for this process, is obtained from Eq. (5.5):

$$\Delta\sigma_{\text{elast}} = Y_f \cdot \epsilon_{xx} = -Y_f \cdot \epsilon_0 > 0. \tag{7.3}$$

The *total* film thickness decrease in z-direction $\epsilon_{zz,\text{total}} < 0$ is a sum of the two components ϵ_0 and $\Delta\epsilon_{zz}$. The component $\Delta\epsilon_{zz}$ is due to lateral contraction upon straining and can be obtained from Eq. (5.4b):

$$\epsilon_{zz,\text{total}} = \epsilon_0 + \Delta\epsilon_{zz} = \epsilon_0 - \frac{2\nu}{1-\nu} \cdot \epsilon_{xx} = \left(1 + \frac{2\nu}{1-\nu}\right) \cdot \epsilon_0. \tag{7.4}$$

Combining Eqs. (7.3) and (7.4) yields the theoretically expected stress increase:

$$\Delta\sigma_{\text{elast}} = -Y_f \frac{1-\nu}{1+\nu} \epsilon_{zz,\text{total}}. \tag{7.5}$$

Even though Eq. (7.5) was derived based on a ’Gedanken experiment’, which assumes a complete *removal* of the film, it is still valid in general for a volume change of a film, which is *constrained* by a substrate: Generally, changes in physical quantities upon *elastic* (i. e. *reversible*) transformations only depend on the *initial* and the *final* state of the system and not on intermediate states. The ’Gedanken experiment’ is just an *alternative* process, which exhibits the same initial and final conditions. Therefore, Eq. (7.5) can be used to estimate the stress increase $\Delta\sigma_{\mathrm{elast}}$ expected for an elastic volume change. Poisson’s ratio was assumed to be $\nu = 0.30 \pm 0.05$, a value typical for many materials including chalcogenides. Due to the fact that Y_f differs between amorphous and crystalline state (Table 6.1), $\Delta\sigma_{\mathrm{elast}}$ was calculated for both the amorphous and the crystalline value for Y_f (Table 7.1). As a result, $\Delta\sigma_{\mathrm{elast}}$ was found to be significantly higher than the experimentally observed stress increase $\Delta\sigma_{\mathrm{exp}}$. Therefore, stress is expected to relax plastically *during* the crystallization process (i. e. *during* the period of stress increase). This is fair to assume because stress also relaxes plastically immediately *after* the crystallization process (Figs. 6.1–6.3).

Plastic stress relaxation during crystallization could result from viscous flow in the not yet crystallized *amorphous* phase as the *crystalline* phase is in general expected to be much more viscous: For instance, in Fig. 6.1 it can be seen, that upon annealing of the crystalline phase for 45 min at 270 ℃, the stress relaxation rate is very small compared to the rate of stress relief that occurs within about two minutes upon crystallization. This suggests that the inelastic stress increase $\Delta\sigma$ is accommodated by viscous flow in the amorphous and not in the crystalline phase.

7.3 Simulation of the stress increase: Viscous flow in the amorphous phase?

In order to find out if stress is relaxed by viscous flow in the amorphous phase upon crystallization, a computer simulation was performed. Figures 7.3(a) and 7.4(a) show the stress build-up for $Ge_4Sb_1Te_5$ and AgInSbTe under the assumption that the process occurs purely elastically. These curves were normalized with respect to the stress $\Delta\sigma_{\mathrm{elast}}$, which is expected upon elastic volume change (Table 7.1). The curves shown in Figs. 7.3(a) and 7.4(a) were obtained by integrating the exothermic crystallization peaks obtained from the DSC measurements (Figs. 3.1 and 3.3) at a heating rate of 5 K/min. [It was assumed that the stress-build-up for a purely elastic process is proportional to the already crystallized fraction f_c of the film ($0 \leq f_c \leq 1$).] Figures 7.3(b)–7.3(d) and 7.4(b)–7.4(d) show the results of the simulation, which takes into account the stress increase of Figs. 7.3(a) and 7.4(a) and stress relaxation due to viscous flow according to Eq. (5.11). A viscosity of

$$\eta = \eta_c \cdot (1 + 2.5 f_c + 14.1 f_c^2 + O(f_c^3)), \qquad f_c \ll 1 \tag{7.6}$$

was assumed. According to Einstein [60, 61], this effective viscosity η describes a mixture of a small volume fraction f_c of solid spherical particles equally distributed and surrounded by a medium of the viscosity η_c. The value for $\eta_c = \eta(T_{c,p})$ was obtained from the results presented in Fig. 6.15. The simulation curves were obtained by splitting the crystallization process in N small time intervals, each of length Δt. The stress σ_{plastic} at the time $t = i \cdot \Delta t$ (where $i = 1 ... N$) was computed by

$$\sigma_{\text{plastic}}(i \cdot \Delta t) = \{\sigma_{\text{plastic}}[(i-1) \cdot \Delta t] + \Delta\sigma_{\Delta t,\text{ elast}}\} \cdot \exp\left(-\frac{Y_f \Delta t}{6\eta}\right), \tag{7.7}$$

where η is the effective viscosity obtained from Eq. (7.6). $\Delta\sigma_{\Delta t,\text{ elast}}$ is the elastic stress increase during the time interval Δt, as obtained from Figs. 7.3(a) and 7.4(a). The stress could be computed recursively by setting $\sigma_{\text{plastic}}(t = 0) = 0$ as initial condition for $i = 1$. The length of the time interval Δt was decreased up to the point, where a further decrease did not affect the result any more.

The simulation yields that the time window of crystallization is not large enough for a significant stress relaxation by viscous flow in the amorphous phase. This becomes more obvious, if higher orders of f_c in Eq. (7.6) are considered [Figs 7.3(d) and 7.4(d)].

The simulations were also performed at heating rates of 80 K/min using the DSC peak measured at this heating rate as a reference curve for the elastic stress increase (not shown). The results were qualitatively the same: the amorphous phase could not relax the stress, either. Simulations for heating rates lower than 5 K/min could not be performed because no DSC data was available for these low rates. However, the same qualitative result is expected for extremely low heating rates: The time interval of crystallization

$$\Delta t_{\text{cryst}} = \frac{\Delta T_{\text{cryst}}}{\dot{T}} \tag{7.8}$$

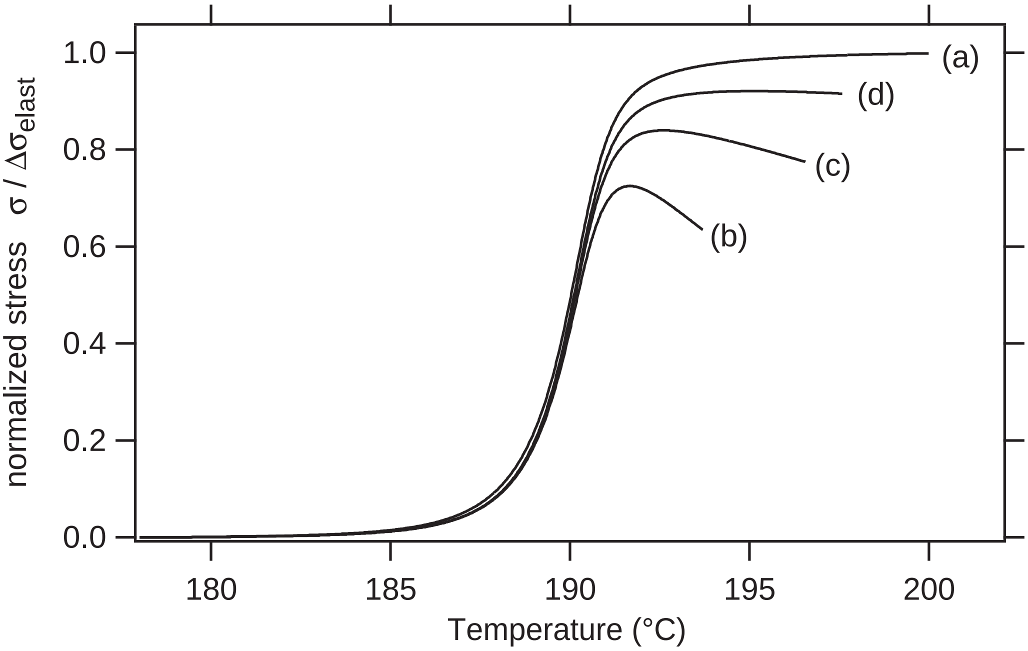

Figure 7.3: Stress increase at the crystallization temperature ($Ge_4Sb_1Te_5$, heating rate: 5 K/min). The stress is normalized with respect to the stress $\Delta\sigma_{\text{elast}}$, which would be observed for a purely elastic process (Table 7.1). (a) Elastic stress increase or crystallized fraction f_c, obtained from differential scanning calorimetry measurements. (b)–(d) Stress increase if viscous flow upon crystallization is considered. These curves are obtained by a computer simulation based on Eq. (7.7). The viscosity of the Einstein model was used for the simulation: (b) $\eta = \eta_c$ as obtained from Fig. 6.15, (c) $\eta = \eta_c \cdot (1 + 2.5 f_c)$, (d) $\eta = \eta_c \cdot (1 + 2.5 f_c + 14.1 f_c^2)$.

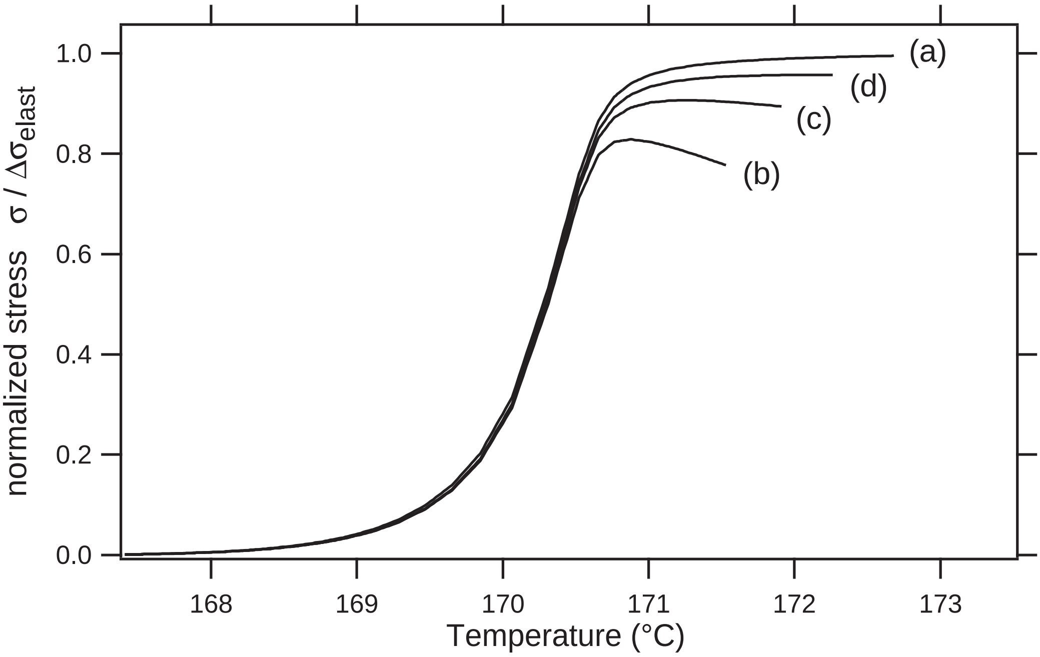

Figure 7.4: Stress increase at the crystallization temperature (AgInSbTe, heating rate: 5 K/min). For additional information see caption of Fig. 7.3.

is *inversely proportional* to the heating rate $\dot{T}$ if it is assumed that the temperature interval of crystallization $\Delta T_{\mathrm{cryst}}$ is independent of heating rate. According to Fig. 6.15, the viscosity η_c is *also inversely proportional* to $\dot{T}$. Therefore, the heating rate dependence cancels out in the exponent of Eq. (7.7) and the simulation always yields the same qualitative result independent of $\dot{T}$. It can be obtained from Table 3.1 that the temperature interval of crystallization $\Delta T_{\mathrm{cryst}}$ is *not* independent of heating rate but it *decreases* with *decreasing* heating rate. However, this does not affect the statement above: as a consequence the time interval $\Delta t_{\mathrm{cryst}}$ additionally decreases at small rates [Eq. (7.8)], which makes stress relaxation even more difficult.

A solution for the discrepancy between $\Delta\sigma_{\mathrm{exp}}$ and $\Delta\sigma_{\mathrm{elast}}$ could eventually be that the system simultaneously passes the glass transition upon crystallization. According to Fig. 4.3 the temperature dependence of the viscosity in the regime of the undercooled liquid is very strong (large equilibrium activation energy), and the viscosity of the amorphous/ liquid phase might be lowered by several orders of magnitude upon crystallization. In this case, stresses might be relaxed significantly in the regime of the undercooled liquid. However, if this was right, *isothermal* crystallization ($\dot{T} = 0$) should result in a *much larger* stress increase than *non-isothermal* crystallization ($\dot{T} > 0$): In isothermal experiments no simultaneous pass of the glass transition is possible (even the opposite: the viscosity increases due to structural relaxation). However, as already mentioned in Chapter 7.1, the *same* stress increase $\Delta\sigma_{\text{exp}}$ was observed in isothermal and non-isothermal experiments. Therefore, a pass of the glass transition during non-isothermal crystallization cannot explain the discrepancy between $\Delta\sigma_{\text{exp}}$ and $\Delta\sigma_{\text{elast}}$.

In summary, the computer simulations did *not* indicate that the amorphous phase relaxes stress upon crystallization by viscous flow for heating rates equal to and lower than 80 K/min. Therefore, the mechanism of stress relaxation upon crystallization remains an open question and needs further clarification. Possibly, the amorphous phase is able to relax stress by viscous flow more *efficiently* if an *inhomogeneous* stress distribution is assumed, which could originate from non-spherically and non-equally distributed crystallites. Exploring the geometry of crystallite distribution could clarify this in the future. Another possibility is that the stresses are relaxed by delamination of the film from the substrate. Chapter 7.4 provides an outlook and some additional information on the stress increase upon crystallization, which may help to clarify this issue in future works.

7.4 Outlook

7.4.1 Film crack and delamination

For *tensile* stresses, the yield stress for film delamination (peeling off) is higher than the yield stress for film crack [62]. Therefore, the film can only delaminate (peel off) from the substrate upon crystallization if it cracked *first* (film crack induces film delamination). Obviously, film delamination induces stress relief. In contrast, film cracks only relief stresses in a very small volume fraction of the film. Therefore, cracks do *not* induce a macroscopically measurable sample curvature change or stress relief.

The yield stresses for film delamination and film crack are film thickness dependent. This is due to the fact that the stress σ is a quantity, which is *normalized* with respect to the area A, on which a force acts (Fig. 4.1). The total force F on the interface between the substrate and the film is therefore given by

$$F = \sigma \cdot d \cdot b, \tag{7.9}$$

where σ is the biaxial film stress, d the film thickness and b the 'width' of the film. Hence, for a *given* stress, the force on the interface increases with increasing film thickness. If the film is thick enough, there is enough force available on the interface to crack or even delaminate the film. Therefore, thicker films are expected to crack and delaminate more easily than thinner films for the same given stress.

This section is concerned with the question: Does the film crack or even delaminate upon crystallization, and how does this effect depend on the film thickness?

7.4.1.1 Thick films (1000 nm)

Cleaned Substrates This subsection will only deal with films deposited on Silicon substrates, which were carefully cleaned using conventionally dish washing liquid before film deposition.

Figure 7.5 shows the result of a stress versus temperature measurement for a $Ge_4Sb_1Te_5$ sample. The heating rate was 30 K/min. At 250 ℃, the power supply of the heat radiators was switched off in order to cool down the sample. After opening the sample chamber, film delamination was visible. Figure 7.6 shows microscopic pictures of this sample. Atomic force microscope (AFM) scans of the film surface yielded that there were really steps of 1000 nm height on the sample, i. e. the film pealed off the substrate partly. The darker regions in Fig. 7.6 correspond to the Si wafer and the brighter regions to the remnants of the film. Most cracks, especially the longest ones [Fig. 7.6(a)], run along the (100) direction of the Si wafer. In Fig. 7.5, a sudden stress and reflectivity decrease is visible upon cooling at about 100 ℃. Due to the fact that it is not possible to look at the sample *during* the measurement, the actual moment of film delamination is unknown. There are three possibilities:

1. The film already delaminates upon heating at the crystallization temperature[3] of about 220 ℃ and delaminates even further upon cooling at 100 ℃.

---

[3] The crystallization temperature seems to be very high here in comparison with the DSC results (Table 3.1), which is due to the fact that the temperature measurement of the wafer curvature setup is less exact at higher heating rates.

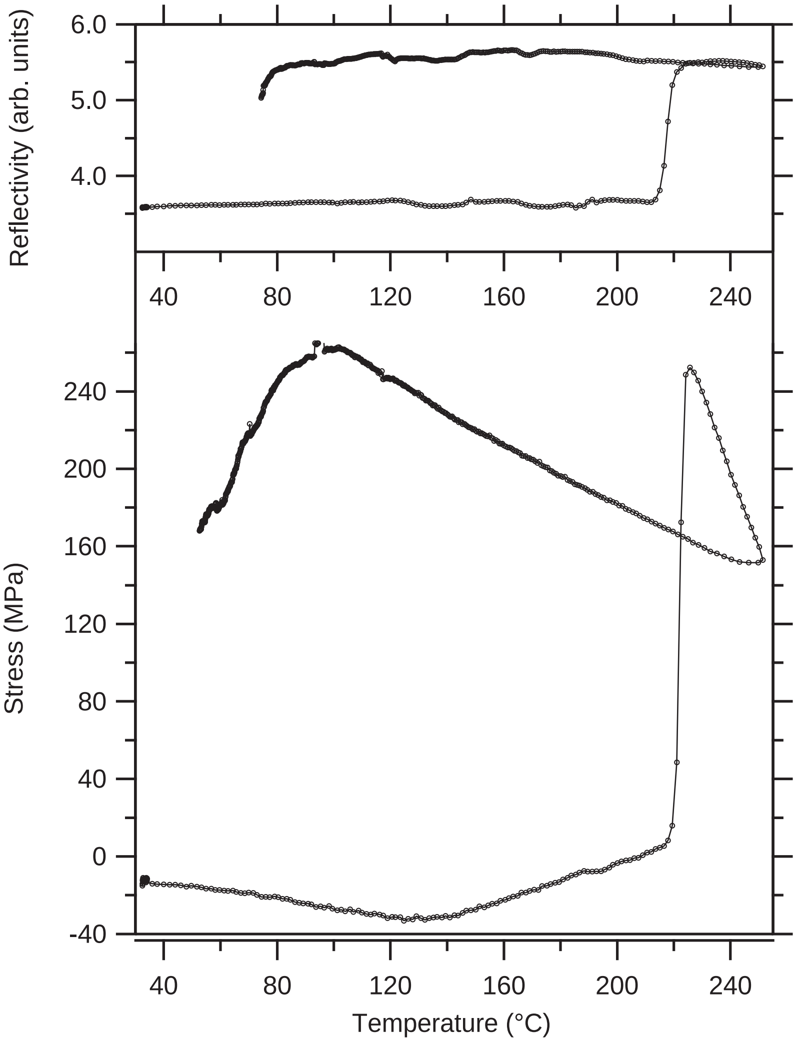

Figure 7.5: Stress and reflectivity as a function of temperature for $Ge_4Sb_1Te_5$. Heating rate: 30 K/min. At 250 °C, the heat radiators were switched off. Film thickness: 1000 nm. Substrate: 200 µm Silicon (cleaned before deposition). Wafer curvature setup: Aachen. Sample age: 4 hours.

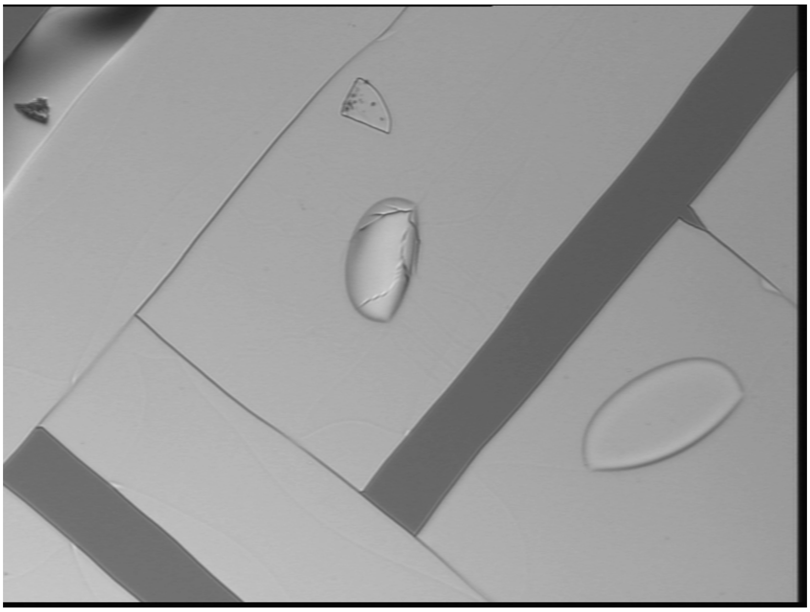

(a)

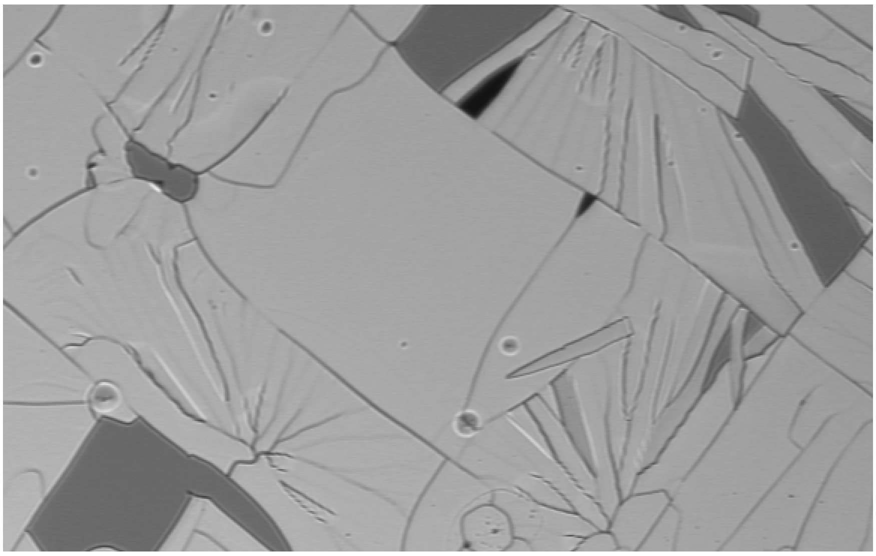

(b)

Figure 7.6: Microscopic pictures of the sample, whose stress versus temperature curve is shown in Fig. 7.5. Film delamination is visible. Picture sizes: 850 µm by 640 µm (a) and 650 µm by 410 µm (b).

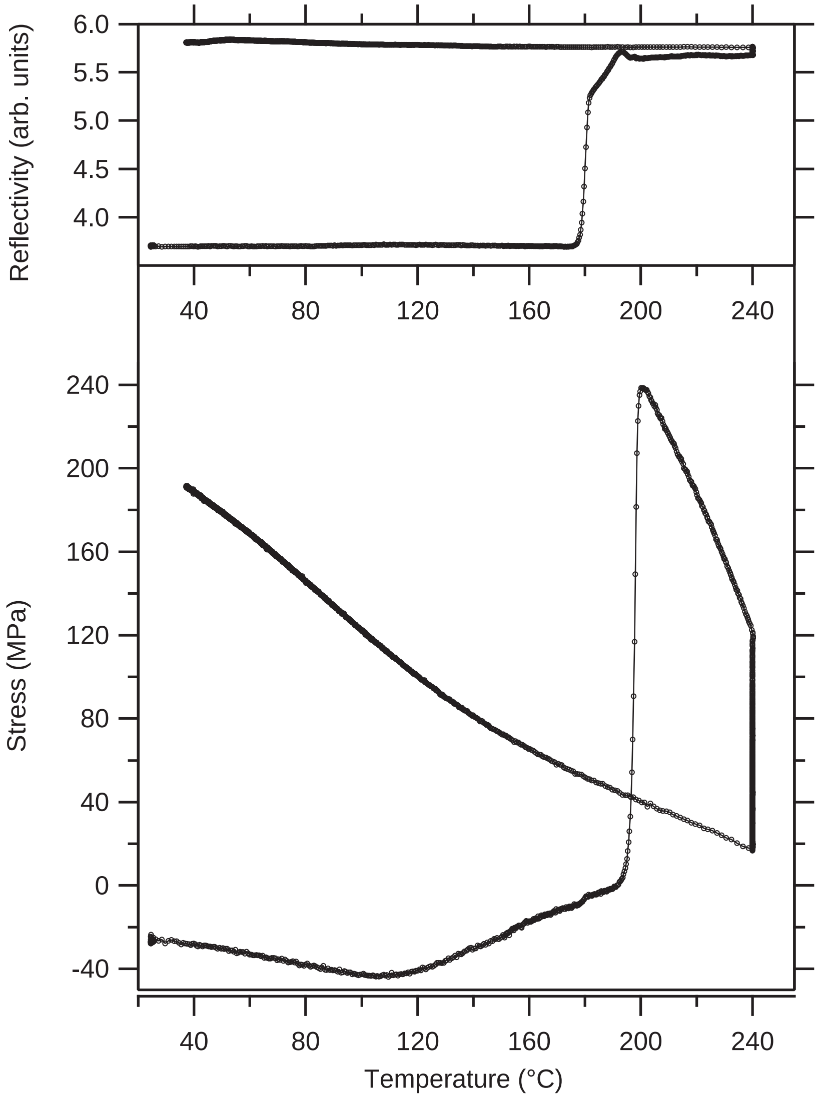

Figure 7.7: Stress and reflectivity as a function of temperature for $Ge_4Sb_1Te_5$. Heating rate: 10 K/min below 150 °C and 5 K/min above 150 °C. At 240 °C, the sample was annealed for 65 minutes and subsequently the heat radiators were switched off. Film thickness: 1000 nm. Substrate: 200 µm Silicon (cleaned before deposition). Wafer curvature setup: Aachen. Sample age: 5 days.

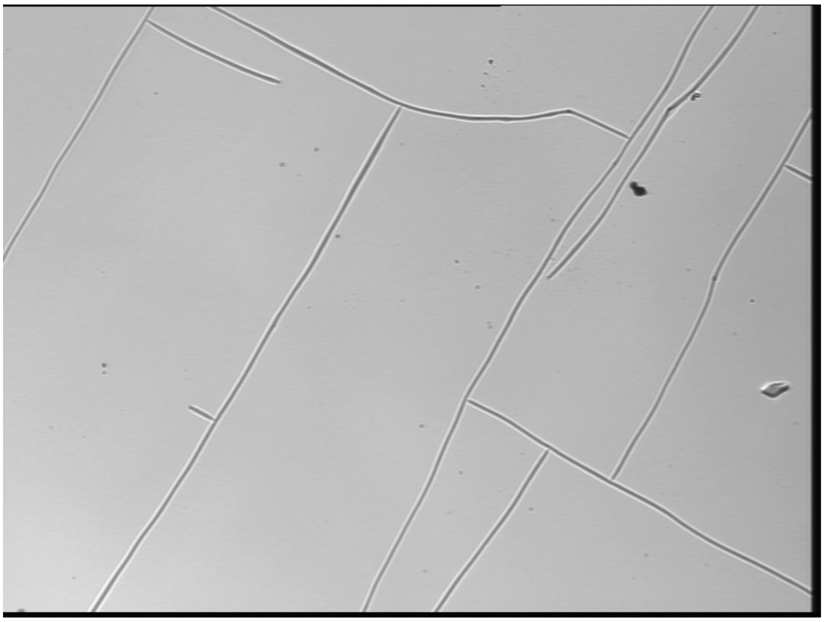

Figure 7.8: Microscopic pictures the sample, whose stress versus temperature curve is shown in Fig. 7.7. Picture size: 850 µm by 640 µm.

2. The film only *cracks* upon heating at the crystallization temperature and *delaminates* upon cooling at about 100 °C.
3. The film does *not* crack upon heating at the crystallization temperature and delaminates[4] upon cooling at about 100 °C.

In order to investigate this further, another measurement was performed (Fig. 7.7). At 240 °C, the sample was annealed for 65 minutes in order to relax a significant amount of stress. Subsequently, the power supply of the heat radiators was switched off. Due to the long annealing time at 240 °C, the stress did not reach the critical value of about 240 MPa upon cooling any more. After opening the chamber only cracks but no delamination were visible in the film (Fig. 7.8). These cracks again ran along the (100) direction of the Si wafer. The only possibility is that these cracks result from the stress increase at about 200 °C. Of course, film delamination cannot absolutely be excluded for the sample shown in Fig. 7.8: there could be some delamination, which is not visible under the microscope. However, if this is the case, the extent of delamination of this sample is much smaller than for the sample shown in Fig. 7.6.

---

[4] The yield stresses for crack formation and delamination are both temperature dependent.

As a conclusion, a ’thick’ film deposited on a carefully cleaned Si substrate *cracks* upon heating at the crystallization temperature and *delaminates* upon cooling at the moment, where the stress reaches a level of about 250 MPa again.

At this point it should be remarked, that the increase in reflectivity at the crystallization temperature for the sample shown in Fig. 7.7 occurs about 20 ℃ earlier than the stress increase. The discussion of this effect, which is due to sample aging, is postponed to Chapter 7.4.3.

Uncleaned Substrates This subsection will only deal with films deposited on Silicon wafers, which were *not* cleaned using dish washing liquid before film deposition. Dust on the wafers was just blown off using high pressure nitrogen.

Figures 7.9 and 7.10 show stress versus temperature measurements. After opening the chamber, film delamination was observed: both samples looked similar to the sample shown in Fig. 7.6. In Figs. 7.9 and 7.10, both reflectivity and stress decrease significantly at the final stage of crystallization. In Fig. 7.9 the film stress does not reach the level of 240 MPa upon cooling again. Therefore it is obvious from the data that the film already delaminates at the final stage of crystallization.

In summary, film crack and delamination upon crystallization is a function of adhesion on the substrate: The film only *cracks* upon crystallization for *cleaned* substrates but *delaminates* at the *final* stage of crystallization for *uncleaned* substrates. This is easily understood: The better the substrate is cleaned, the better is the adhesion of the film on the substrate and therefore the higher is the force on the interface required to delaminate the film [Eq. (7.9)]. Upon cooling, the film *delaminates* (further) once the stress adopts the critical value of 240 or 250 MPa again. The latter effect is independent of whether the substrate was cleaned or not.

Crack formation and delamination sometimes, but not always[5], occurs for the other two alloys in 1000 nm thick films, too, but it looks different: the cracks do not run along the the (100) direction of the Si wafer as for $Ge_4Sb_1Te_5$. Figure 7.11 shows a cracked $Ge_2Sb_2Te_5$ film and Fig. 7.12 a cracked AgInSbTe film. At the darker regions, the film delaminated.

The alert reader may have wondered if the results for the crystalline biaxial

---

[5] Eventually the critical thickness for crack formation is higher for $Ge_2Sb_2Te_5$ and AgInSbTe.

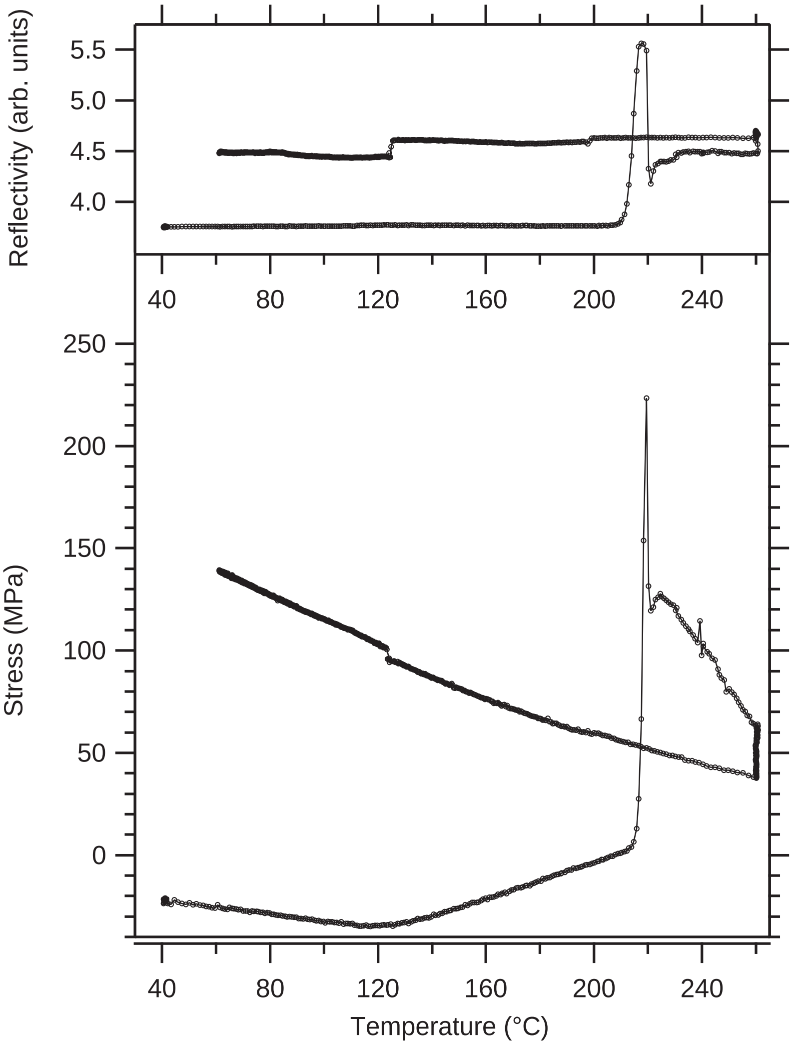

Figure 7.9: Stress and reflectivity as a function of temperature for $Ge_4Sb_1Te_5$. Heating rate: 20 K/min. At 260 ℃, the sample was annealed for 4 minutes and subsequently the heat radiators were switched off. Upon cooling, the optics were recalibrated at 120 ℃, which results in a small step in the data. Film thickness: 1000 nm. Substrate: 200 µm Silicon (*not* cleaned before deposition). Wafer curvature setup: Aachen. Sample age: 3 hours.

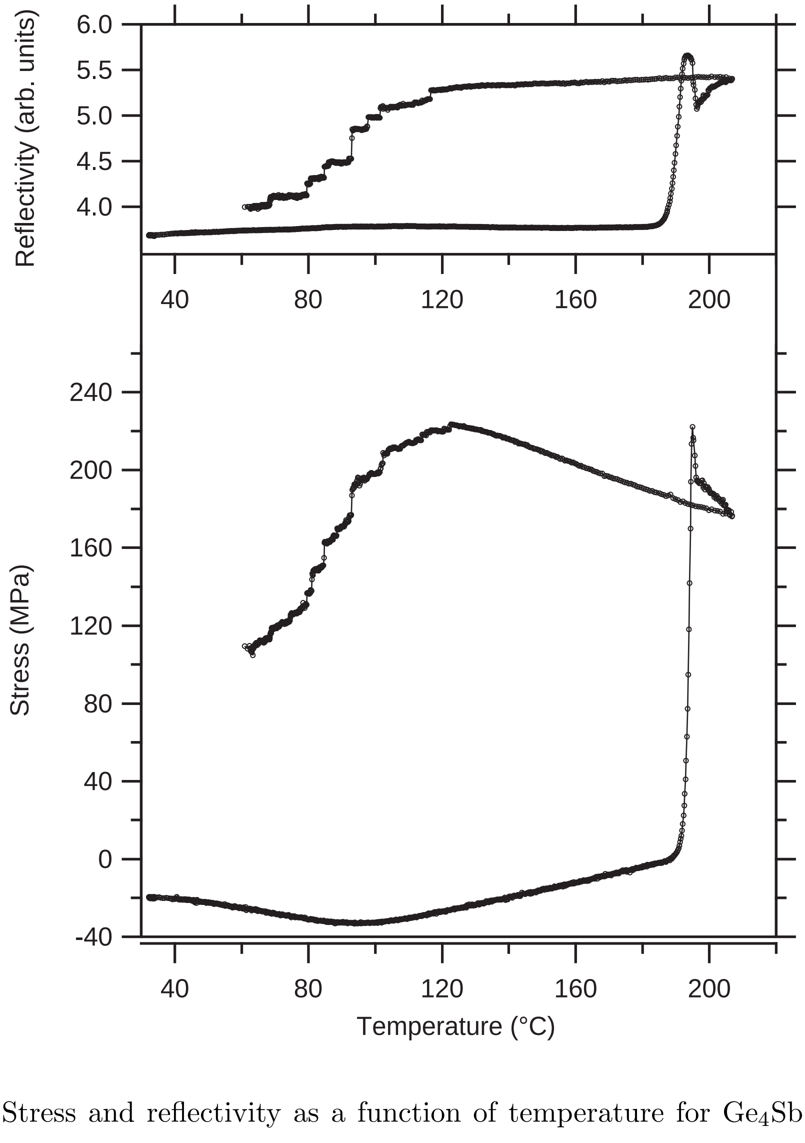

Figure 7.10: Stress and reflectivity as a function of temperature for $Ge_4Sb_1Te_5$. Heating rate: 5 K/min. At 205 °C the heat radiators were switched off. Film thickness: 1000 nm. Substrate: 200 µm Silicon (*not* cleaned before deposition). Wafer curvature setup: Aachen. Sample age: 4 hours.

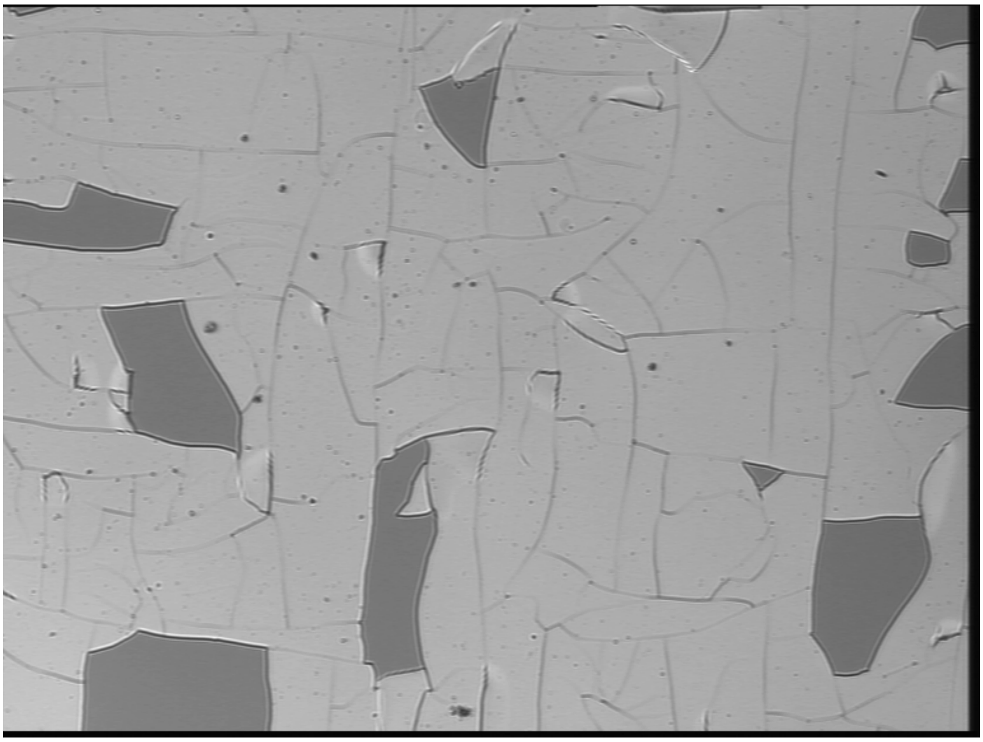

Figure 7.11: Microscopic pictures of a $Ge_2Sb_2Te_5$ sample. This picture was taken after having heated the sample above the crystallization temperature. Film thickness: 965 nm. Substrate: 200 µm Silicon (cleaned before deposition). In contrast to $Ge_4Sb_1Te_5$, the cracks in $Ge_2Sb_2Te_5$ films do not run in a uniform direction. The darker regions correspond to the Si wafer, i. e. the film delaminated here. Picture size: 850 µm by 640 µm.

moduli Y_f and CTEs α_f presented in Chapter 6.1 originate from samples, which have cracked upon crystallization. This is not the case: all samples, which were used for the determination of Y_f and α_f did not crack upon crystallization (at least no cracks were visible under the microscope). Film cracks in $Ge_4Sb_1Te_5$ were avoided by decreasing the film thickness of this alloy to 725 nm (Table 6.1).

7.4.1.2 Thin films (200 nm)

For thin films (200 nm or thinner) no cracks or delamination are visible under the microscope after annealing. Figure 7.13 shows a stress versus temperature measurement for a $Ge_4Sb_1Te_5$ film. The heat radiators were switched off immediately after the stress increase in order to induce the largest possible stress upon cooling. However, upon

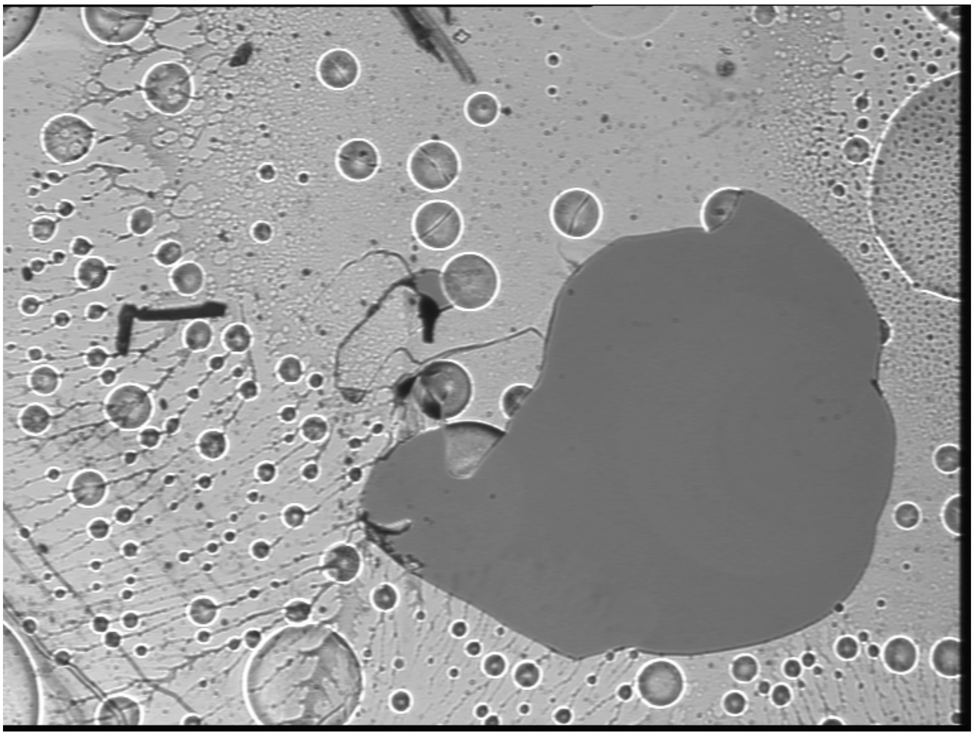

Figure 7.12: Microscopic pictures of a AgInSbTe sample. This picture was taken after having heated the sample above the crystallization temperature. Film thickness: 850 nm. Substrate: 200 µm Silicon (cleaned before deposition). The large darker region at the right bottom displays a 'hole' in the film, where the Si wafer becomes visible. The small circles are probably 'bubbles' in the film, where film delamination possibly took place. These bubbles are not observed for the other two alloys. Picture size: 850 µm by 640 µm.

cooling, the stress becomes much larger than the critical value of about 240–250 MPa. Subsequent thermal cycling was reversible, and could not crack the film. In contrast to thick films, the force F on the interface is not large enough to induce cracks in thin films [Eq. (7.9)].

For the other two alloys, cracks and delamination was not observed for film thicknesses of 200 nm either.

7.4.2 Isothermal versus non-isothermal crystallization

In an isothermal experiment, the time window of crystallization is much longer than for non-isothermal crystallization (Table 7.2). However, the magnitude of stress increase due to crystallization is independent of whether the experiment was performed isothermally or not (Fig. 7.14). For temperatures *higher* than the crystallization temperature, the stress evolution upon heating is *reversible* (Fig. 7.14). In contrast, *non*-isothermal experiments always lead to an *irreversible* stress evolution upon heating above the crystallization temperature (Figs. 6.1, 6.2, 6.3 and 7.5). It remains an open question why this is the case.

7.4.3 Sample oxidation

Figure 7.7 shows that the increase in reflectivity at the crystallization temperature occurs at a lower temperature than the stress increase. This effect is ascribed to film oxidation: During the time between sample preparation (sputtering) and start of the measurement the sample was stored in air at room temperature for about five days. For 'fresh' samples (which are only a few hours old), this earlier onset of reflectivity increase is not observed (Figs. 7.1, 7.5, 7.9, 7.10 and 7.13). In order to find out whether aged samples exhibit really an *early* increase in reflectivity rather than a *delayed* increase in stress, stress versus temperature measurements of two differently aged samples of the same sputtering series were performed at the same heating rate (not shown). The stress increase occurred at the same temperature for both fresh and aged sample, but the reflectivity increase occurred at lower temperature for the aged sample. Therefore, old samples really exhibit an *early* increase in reflectivity rather than a *delayed* increase in stress. The phenomenon is observed for all three alloys, though aging takes longest

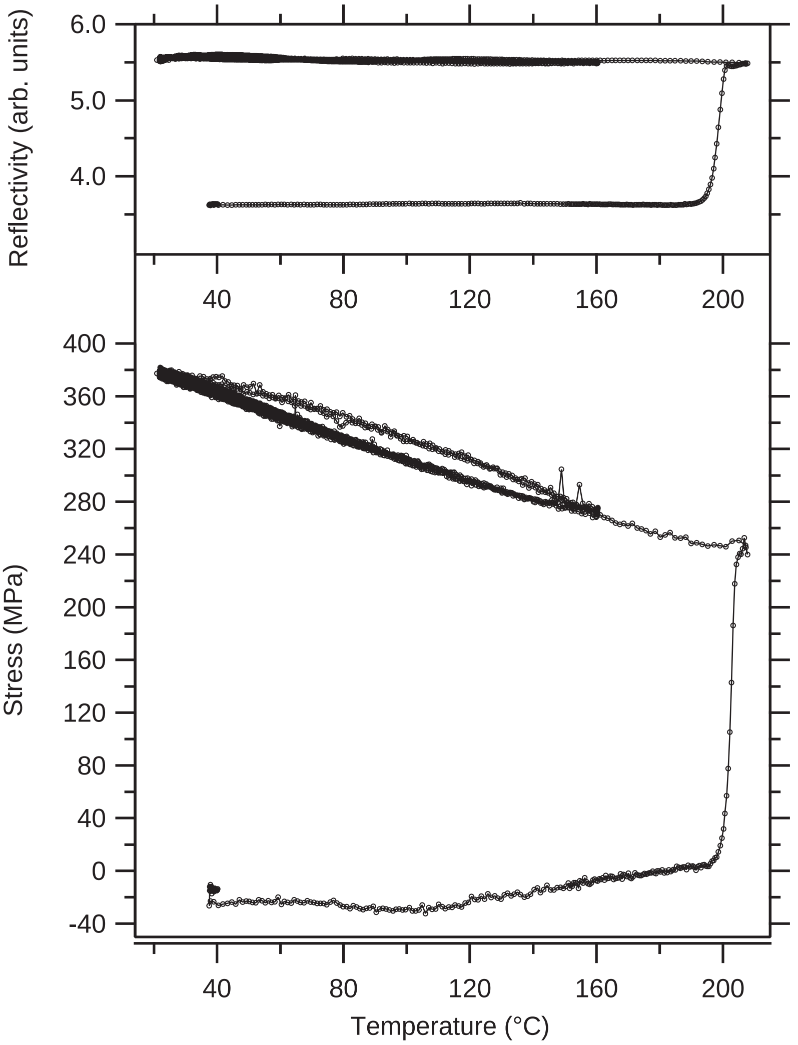

Figure 7.13: Stress and reflectivity as a function of temperature for $Ge_4Sb_1Te_5$. Heating rate: 10 K/min below 150 ℃ and 5 K/min above 150 ℃. Immediately after the stress increase due to crystallization (at 207 ℃) the heat radiators were switched off in order to induce the largest possible amount stress upon cooling. Subsequent thermal cycling in the crystalline phase is reversible. Film thickness: 200 nm. Substrate: 200 µm Silicon (cleaned before deposition). Wafer curvature setup: Aachen. Sample age: 3 hours.

Table 7.2: Stress increase due to crystallization in isothermal experiments. The experiments were performed at temperature T_{iso}. The time window of stress increase is labelled as Δt_{iso}. The Table shows that the time window is not exactly reproducible. Deviations possibly result from different thermal histories of the samples. Film thicknesses: 1000 nm (except for sample 2-225-93: 965 nm). Substrates: 200 µm Silicon. The experiments were performed using the Wafer curvature setup in Aachen.

Sample	T_{iso} (°C)	Δt_{iso} (min)
	(a) $Ge_4Sb_1Te_5$	
18-415-75	165	38
27-415-81	165	70
	(b) $Ge_2Sb_2Te_5$	
2-225-93	120	330
22-225-66	145	10
	(c) AgInSbTe	
16-ag-90	135	82
17-ag-91	135	196

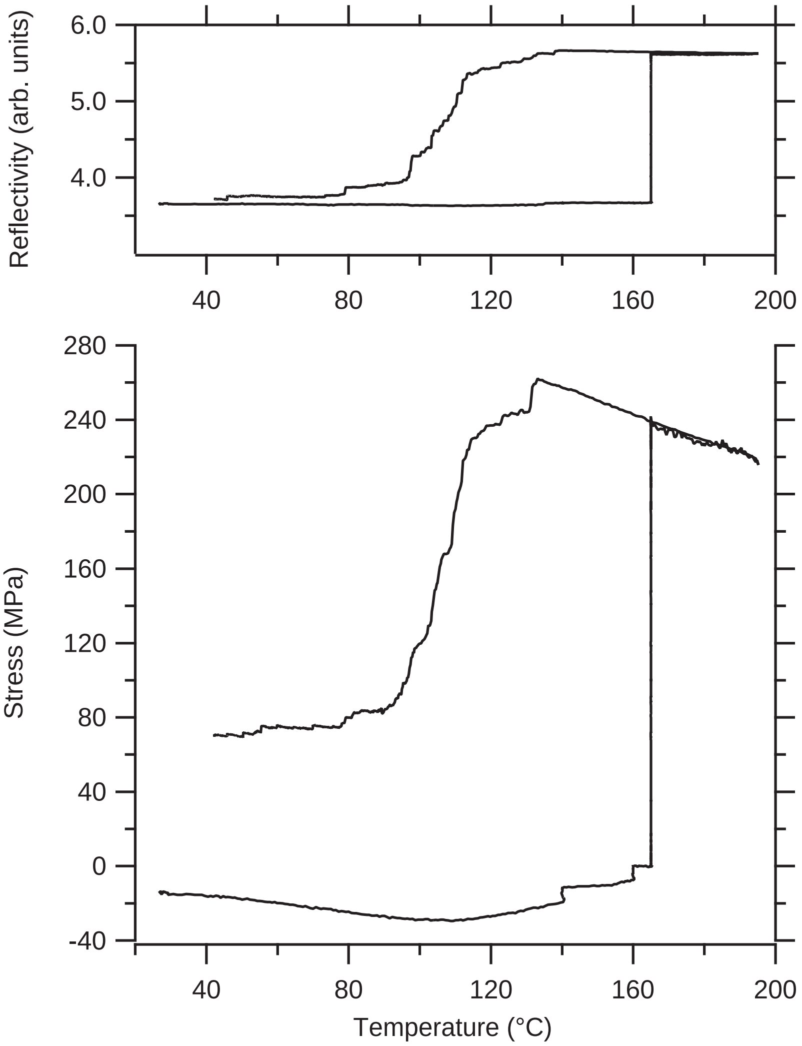

Figure 7.14: Stress and reflectivity as a function of temperature for $Ge_4Sb_1Te_5$ (heating rate: 10 K/min). The sample was annealed at 140 °C for 3 minutes and at 160 °C for 10 minutes. During these time intervals some stress was relaxing by viscous flow. At 165 °C the sample was annealed for 70 minutes and crystallized isothermally. Further heating (5 K/min) leads to *reversible* stress evolution. At 195 °C the heat radiators were switched off. Upon cooling, the film delaminated at about 130 °C and looked similar to the sample shown in Fig. 7.6. Film thickness: 1000 nm. Substrate: 200 µm Silicon (cleaned before deposition). Wafer curvature setup: Aachen. Sample age: 6 hours. For comparison with Table 7.2, this sample is labelled '27-415-81'.

for AgInSbTe. The existence of the oxidation layer is confirmed by XRR measurements and its thickness was determined to a few nanometers [63].

Two theories can be advanced about the crystallization kinetics of oxidized samples:

1. Aged samples crystallize heterogeneously from the oxidation layer (film surface) towards the substrate. In Fig. 7.7 crystallization starts at 180 ℃ and is completed at 200 ℃. During this temperature interval of 20 ℃, the interface 'amorphous-crystalline' moves *continuously* from the oxidation layer towards the substrate upon heating. Due to the fact that the laser beam is reflected at the *top* of the film, the observed increase in reflectivity occurs already at the initial stage of crystallization, i. e. at 180 ℃.

2. The oxidation layer crystallizes at 180 ℃, which leads to a reflectivity increase if it is assumed that the reflectivity of the crystalline oxide is higher than the reflectivity of the amorphous oxide. In the range between 180 ℃ and 195 ℃, the film remains amorphous (except for the crystallized oxidation layer). In the range between 195 ℃ and 200 ℃ the entire film crystallizes (either heterogeneously from the film surface towards the substrate or homogeneously).

Theory (1.) seems to be very unlikely: If this theory was right, a continuous stress increase would be expected between 180 ℃ and 200 ℃ if it is assumed that the amorphous phase is not able to relax stress upon crystallization according to Chapter 7.3. Figures 7.15 and 7.16 disprove theory (1.) and make the correctness of theory (2.) likely. The sample was heated to 110 ℃ ($\dot{T} = 5\,\mathrm{K/min}$). Subsequently, it was annealed at 110 ℃ for 17 hours. The reflectivity remained at a constant level of about 3.6 during the first 1.7 hours upon annealing. During the next 2.6 hours, the reflectivity increased continuously from a level of 3.6 to 4.7. Subsequently, the reflectivity remained at a level of 4.7 for the remaining 12.7 hours. The stress was relaxing towards zero due to viscous flow within the first 30 minutes of annealing and remained zero for the subsequent 16.5 hours. The tremendous stress increase of about 220 MPa did not occur before the sample was further heated up ($\dot{T} = 5\,\mathrm{K/min}$). At 160 ℃, the sample was annealed for 15 minutes and subsequently the heat radiators were switched off. Upon cooling, the stress adopts the critical value of about $\sigma_{\mathrm{critical}} = 240\,\mathrm{MPa}$ again, which leads to film crack and delamination at about 40 ℃. The microscopic picture shown in

Fig. 7.11 was taken from *this* sample.

The curves shown in Figs. 7.15 and 7.16 prove that there is no crystallization after the moment of reflectivity increase, i. e. theory (1.) is wrong. Based on the assumptions that the oxidation layer *indeed* crystallizes *earlier*[6] than the film and that the reflectivity of the crystalline oxidation layer is higher than the reflectivity of the amorphous oxidation layer, theory (2.) can be stated to be correct.

---

[6] This assumption is still questionable and should be investigated in more detail in future works: Due to the high electronegativity of oxygen [64], chemical bonding in oxides is often *stronger* than in the corresponding non-oxidized materials [65]. Strong bonding could *impede* rather than *facilitate* the crystallization of oxides. It has to be clarified in the future if this applies to the Te alloys and their oxides.

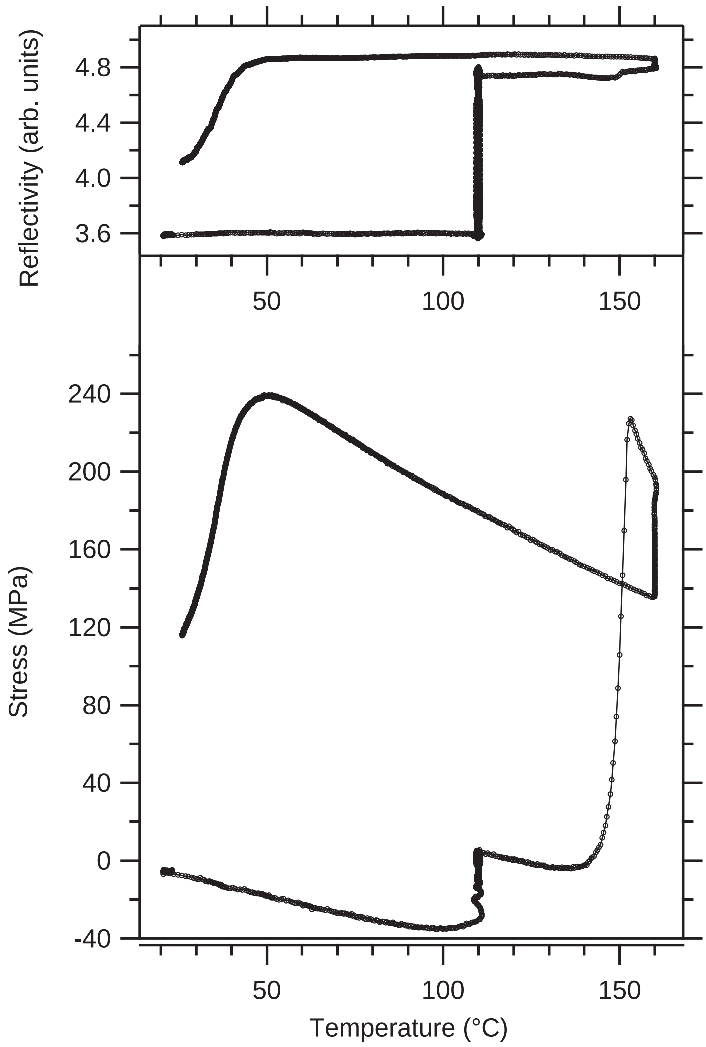

Figure 7.15: Stress and reflectivity as a function of temperature for $Ge_2Sb_2Te_5$. Film thickness: 965 nm. Substrate: 200 µm Silicon (cleaned before deposition). Wafer curvature setup: Aachen. Sample age: 10 months.

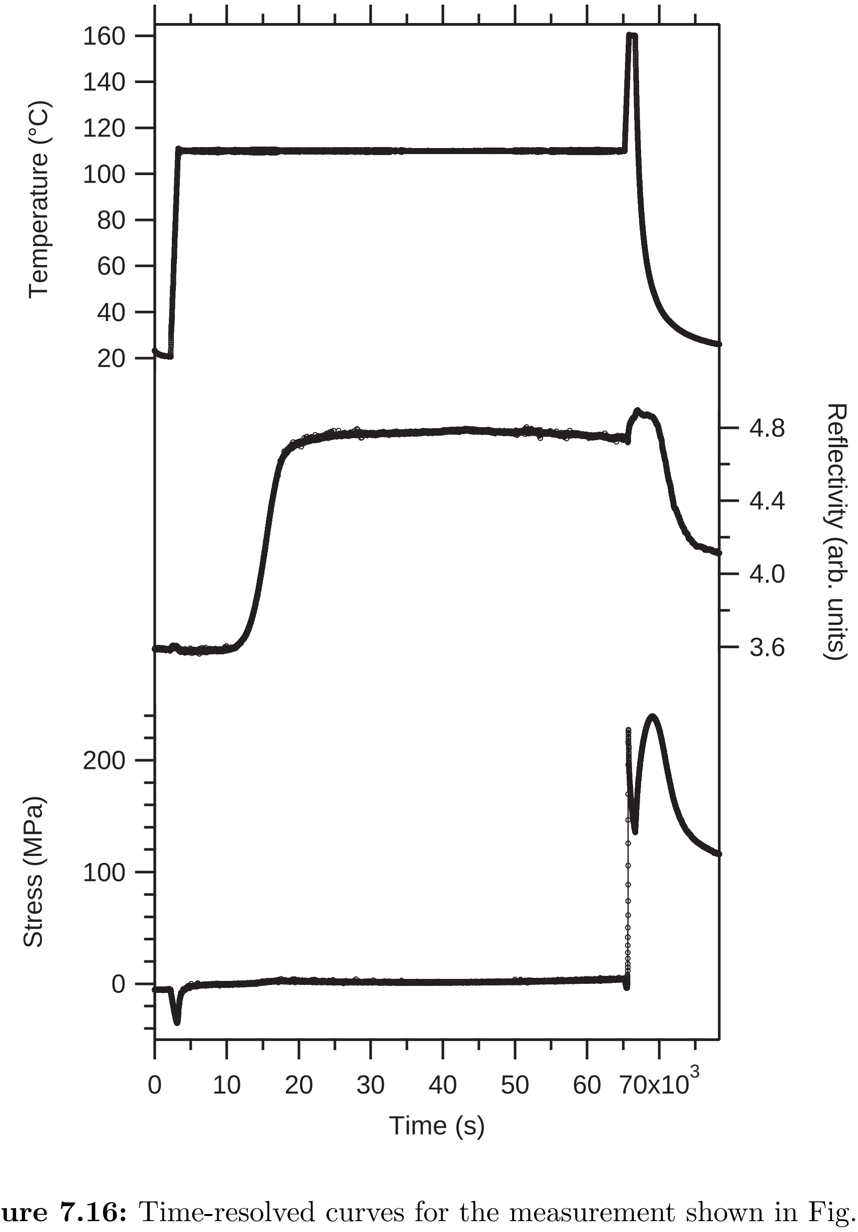

Figure 7.16: Time-resolved curves for the measurement shown in Fig. 7.15

Conclusions Part II

1. The biaxial moduli Y_f and the linear thermal expansion coefficients α_f of amorphous and crystalline $Ge_4Sb_1Te_5$, $Ge_2Sb_2Te_5$ and AgInSbTe thin films were measured. The moduli of the amorphous phases are a factor of two lower than the corresponding crystalline values. The thermal expansion coefficient of the amorphous and the crystalline phase is similar for each alloy. $Ge_4Sb_1Te_5$ exhibits the highest and AgInSbTe the lowest modulus. In contrast, $Ge_4Sb_1Te_5$ exhibits the lowest and AgInSbTe the highest expansion coefficient.
2. Far away from metastable equilibrium, the viscosity η of the amorphous phases increases linearly with time at constant temperature. This is attributed to bimolecular structural relaxation kinetics.
3. The viscosity increase rate $\dot{\eta}$ as a function of temperature was determined from several measurements. $\dot{\eta}$ is highest for $Ge_4Sb_1Te_5$ and lowest for AgInSbTe for temperatures between 60 ℃ and 120 ℃.
4. The average isoconfigurational activation energy Q_{iso} of the viscosity and the average activation energy Q_{rel} of the rate constant for structural relaxation k_r were determined from several measurements. Q_{iso} and Q_{rel} scale with the absolute melting temperature T_m of the material.
5. Upon crystallization, a film stress build-up of around 200 MPa was observed and attributed to the density increase in the film. By comparison with a theoretical estimate of the stress increase for a purely elastic process it could be concluded that stress is relaxed plastically upon crystallization. Computer simulations of this stress increase based on results from the DSC and the viscosity measurements were performed. These simulations did *not* indicate that the amorphous phase

relaxes stress upon crystallization by viscous flow for heating rates equal to and lower than 80 K/min. However, this point is not absolutely clarified before the geometry of crystallite distribution is explored, which could be responsible for a more efficient stress relaxation in the amorphous phase.

6. The film thickness dependence of crack formation upon crystallization was investigated. It was shown that film cracks and film delamination can be significantly reduced by thoroughly cleaning the substrate before film deposition. Therefore, cracks and delamination are a function of adhesion on the substrate.

Part III

Crystallization mechanisms of thin amorphous chalcogenide films used for optical data storage

Chapter 8

Theoretical background

8.1 Crystal nucleation

8.1.1 Thermodynamics of nucleus formation

According to Fig. 1.4, crystallization of the amorphous/ liquid phase lowers Gibbs free energy of the system. However, apart from this 'gain' in energy ΔG_{lc} [Eq. (1.11)], the system also has to spend *interfacial energy* ΔG_σ in order to create an interface between the crystalline nucleus and the surrounding liquid[1]. For *homogeneous nucleation*[2], the total change in Gibbs free energy ΔG_{total} is therefore [66]

$$\begin{aligned} \Delta G_{total} &= -\Delta G_{lc} + \Delta G_\sigma \\ &= -\Delta G_{lc,V} \cdot V + \sigma \cdot A, \end{aligned} \tag{8.1a}$$

where V and A are the volume and the surface of the nucleus respectively, $\Delta G_{lc,V} > 0$ is Gibbs free energy difference between liquid and crystal *per volume* and $\sigma > 0$ the crystal-melt interfacial tension ('classical' nucleation theory after Gibbs). According to Fig. 1.4, $\Delta G_{lc,V}$ increases with *decreasing* temperature. In contrast, interface modelling indicated that σ increases with *increasing* temperature [67, 68, 69]. σ scales with the entropy of fusion ΔS_f, due to the entropy loss in the liquid near the interface. For

---

[1] By convention, *both* ΔG_{lc} *and* ΔG_σ are greater than zero. This simplifies the equations below.

[2] 'Homogeneous nucleation' means that the nucleus is completely surrounded by the liquid. If foreign substances are involved (e. g. if the nucleus is in contact with a substrate), the process is commonly called 'heterogeneous nucleation'.

spherical nuclei of radius r, rewriting of Eq. (8.1a) yields

$$\Delta G_{total}(r) = -\Delta G_{lc,V} \cdot \frac{4}{3}\pi r^3 + \sigma \cdot 4\pi r^2. \tag{8.1b}$$

Figure 8.1 qualitatively displays the evolution of ΔG_{total} as a function of r. For $r < r_c$, the growth of a nucleus would be accompanied with an increase in energy. As a consequence, the nucleus decays again. Nuclei with $r > r_c$ are *stable*: a further growth is energetically favorable. r_c is commonly called the *critical radius*: a nucleus of radius $r = r_c$ becomes a *stable* nucleus if only one additional atom of the surrounding liquid is integrated into the nucleus. Equating $\frac{\partial \Delta G_{total}(r)}{\partial r} = 0$ yields

$$r_c = \frac{2\sigma}{\Delta G_{lc,V}} \tag{8.2}$$

and

$$\Delta G_c = \frac{16\pi}{3} \frac{\sigma^3}{(\Delta G_{lc,V})^2}, \tag{8.3a}$$

where the *nucleation barrier* ΔG_c is the maximum value for $\Delta G_{total}(r)$ (see Fig. 8.1). For *heterogeneous* nucleation a rigorous derivation yields [66]

$$\Delta G_c^{(*)} = \frac{16\pi}{3} \frac{\sigma^3}{(\Delta G_{lc,V})^2} \cdot f(\theta), \tag{8.3b}$$

where $f(\theta)$ is a geometrical factor, which depends on the wetting angle θ [$0 \leq f(\theta) \leq 1$; $f(\theta) = 1$ for homogeneous nucleation].

Due to thermal fluctuations nuclei are formed continuously. The *equilibrium concentration* of crystalline nuclei is then given by

$$n(r) = n_0 \cdot \exp\left(-\frac{\Delta G_{total}(r)}{k_B T}\right), \tag{8.4a}$$

where $n(r)$ is the number of nuclei of radius r and n_0 a constant. Therefore, the *equilibrium number* of critical nuclei n_c is given by

$$n_c = n_0 \cdot \exp\left(-\frac{\Delta G_c^{(*)}}{k_B T}\right). \tag{8.4b}$$

The formation of a stable nucleus is commonly called *crystal nucleation.*

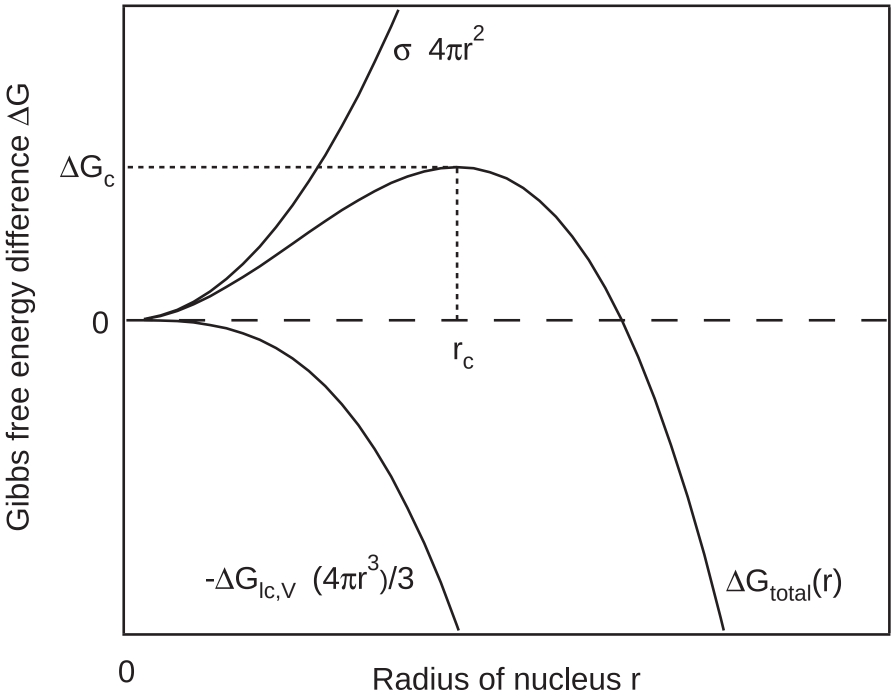

Figure 8.1: Energy balance for the formation of a crystalline nucleus of radius r

8.1.2 Kinetics of nucleation

A mathematical derivation of the frequency of crystal nucleation $I(t)$ as a function of time is a rather cumbersome process. However, when the so-called *incubation time* has elapsed, the system adopts the equilibrium concentration of crystalline nuclei given in Eq. (8.4a). In this case, the equilibrium number of critical nuclei [Eq. (8.4b)] determines the *steady state crystal nucleation frequency* I_{ss}. According to the *Becker-Döring-model* [70, 71] I_{ss} is given by

$$I_{ss} = I_0 \cdot k_j \cdot \exp\left(-\frac{\Delta G_c^{(*)}}{k_B T}\right), \tag{8.5}$$

where I_0 is a constant and k_j the jump frequency per atom across the interface. For *pure* liquids, atomic neighbors generally do not have to change upon crystallization. In this case, crystallization occurs *collision limited* and the jump frequency is

$$k_j = \frac{u_{sound}}{\lambda} \qquad \text{(collision limited)}, \tag{8.6a}$$

where λ is the interatomic distance and u_{sound} the sound velocity of the liquid. For *alloys*, changes of neighbors are in general necessary for crystallization. In this case, crystallization occurs *diffusion limited* and the jump frequency is

$$k_j = \frac{6D}{\lambda^2} \qquad \text{(diffusion limited)}, \tag{8.6b}$$

where D is the diffusivity of the liquid [66]. The diffusivity D and the viscosity η of the liquid are related by the *Stokes-Einstein relation*

$$\eta D = \frac{k_B T}{3\pi a_0}, \tag{8.7}$$

where a_0 is on the order of a molecular diameter [39, 66]. Therefore, the temperature dependence of the steady state nucleation frequency $I_{ss}^{(dl)}$ for *diffusion limited* crystallization is given by

$$\boxed{I_{ss}^{(dl)} \propto \frac{1}{\eta} \cdot \exp\left(-\frac{\Delta G_c^{(*)}}{k_B T}\right)}. \tag{8.8}$$

For the calculation of $I_{ss}^{(dl)}$ in the regime of the undercooled liquid, a Fulcher-Vogel equation [Eq. (4.2)] may be assumed for the viscosity η. In contrast, for temperatures below the glass transition temperature, an Arrhenius temperature dependence of the viscosity may be assumed [Eq. (4.9)]. The temperature dependence of $I_{ss}^{(dl)}$ in the regime of the undercooled liquid is qualitatively displayed in Appendix A.

8.2 Crystal growth

8.2.1 The crystal growth velocity

It is well established that the overall process of crystallization involves two individual processes: Crystal nucleation and crystal growth. Once a stable nucleus is formed, it grows by the transfer of atoms from the liquid to the crystalline phase through the interface (either by collision or diffusion, as discussed above). The liquid-crystalline interface then moves with the velocity u_{cg} [66]:

$$u_{cg} = u_0 \cdot k_j \cdot \left[1 - \exp\left(-\frac{\Delta G_{lc,\,\text{atom}}}{k_B T}\right)\right]. \tag{8.9}$$

u_{cg} is called the *crystal growth velocity.* u_0 is a constant and $\Delta G_{lc,\,\text{atom}} > 0$ is the difference in Gibbs free energy between the liquid and the crystal *per atom.* The prefactor k_j is the *same* as for the nucleation frequency I_{ss} [Eqs. (8.6a) and (8.6b)]. Therefore, the temperature dependence of the growth velocity for *diffusion limited* crystallization $u_{cg}^{(dl)}$ is given by

$$\boxed{u_{cg}^{(dl)} \propto \frac{1}{\eta} \cdot \left[1 - \exp\left(-\frac{\Delta G_{lc,\,\text{atom}}}{k_B T}\right)\right]}. \tag{8.10}$$

The temperature dependence of $u_{cg}^{(dl)}$ in the regime of the undercooled liquid is qualitatively displayed in Appendix A.

8.2.2 Isothermal crystallization

The interplay of crystal nucleation and crystal growth is a rather complicated process and difficult to handle mathematically. However, for the special case of *isothermal homogeneous crystallization* in *isotropic infinitively spread space* the *Johnson-Mehl-Avrami equation* [72, 73, 71, 66] yields the crystallized fraction of space f_c as a function of time t ($0 \leq f_c(t) \leq 1$):

$$f_c(t) = 1 - \exp\left(-\frac{4}{3}\pi u_{cg}^3 \cdot \int_0^t I(t) \cdot (t - t')^3 dt'\right), \tag{8.11}$$

where u_{cg} is the growth velocity defined in Eq. (8.9), and $I(t)$ is the time dependent nucleation frequency. The integral can be solved for the special case of a steady state, where $I(t) = I_{ss} =$const in time [Eq. (8.5)]. Using $\int_0^t (t - t')^3 dt' = \frac{t^4}{4}$ yields

$$f_c(t) = 1 - \exp\left[-(k_m t)^4\right], \tag{8.12}$$

where

$$k_m = \left(\frac{1}{3}\pi u_{cg}^3 I_{ss}\right)^{\frac{1}{4}} \tag{8.13}$$

is called the *rate constant.* For experimental purposes, the temperature dependence of k_m can be approximated to be Arrhenius,

$$k_m(T) \propto \exp\left(-\frac{E_A}{k_B T}\right), \tag{8.14}$$

where E_A is the effective activation energy for crystallization [Eq. (3.2) and Table 3.4].

Chapter 9

Separating nucleation and growth

In this Chapter a preliminary model will be suggested, which is able to predict the crystallization mechanism of the phase change alloys described in Chapter 2.1. The model is based on the results from the viscosity measurements presented in Chapter 6.2.

First of all, crystallization of the phase change alloys is expected to occur diffusion limited: According to Ref. [74] the coordination number of these alloys changes significantly upon crystallization. Therefore, Eqs. (8.8) and (8.10) are expected to apply for the study of crystallization kinetics. However, the choice of the temperature dependence of the viscosity η around the peak crystallization temperature $T_{c,p}$ (Table 3.1) is not straightforward as it is not known if the alloys pass the glass transition temperature T_g upon crystallization. If $T_{c,p} < T_g$, the viscosity in Eqs. (8.8) and (8.10) may be approximated by Eq. (4.9). However, since the rapid increase in atomic mobility associated with the glass transition also leads to rapid crystallization, T_g is expected to be close to $T_{c,p}$ for the phase change alloys (see also Chapter 3.3). In this case, the glass adopts its equilibrium structure upon crystallization and the temperature dependence of the viscosity is complicated: the *intrinsic* temperature dependence may be Arrhenius [Eq. (4.9)] in the first stage of crystallization and Fulcher-Vogel like [Eq. (4.2)] in the final stage of crystallization. For 'ultrahigh' heating rates ($\dot{T} \gg 80\,\mathrm{K/min}$) crystallization might even occur in the regime of the undercooled liquid. Unfortunately, the temperature dependence of the equilibrium viscosity η_{eq} is not known for the phase change alloys: Due to rapid crystallization, the undercooled liquid is not available for viscosity measurements. Therefore, the viscosity around $T_{c,p}$ can only be roughly estimated by the Arrhenius temperature dependence [Eq. (4.9)]. Hence, all conclusions presented hereafter must be handled carefully and may be considered as qualitative estimates only.

The temperature dependence of the nucleation frequency $I_{ss}^{(dl)}$ around the peak crystallization temperature $T_{c,p}$ is given by

$$I_{ss}^{(dl)} \propto \exp\left(-\frac{Q_{iso} + \Delta G_c^{(*)}}{k_B T}\right) \tag{9.1}$$

and the temperature dependence of the growth velocity $u_{cg}^{(dl)}$ by

$$u_{cg}^{(dl)} \propto \exp\left(-\frac{Q_{iso}}{k_B T}\right) \cdot \left[1 - \exp\left(-\frac{\Delta G_{lc,\,\mathrm{atom}}}{k_B T}\right)\right]. \tag{9.2a}$$

The temperature dependence of the term $\left[1 - \exp\left(-\frac{\Delta G_{lc,\,\mathrm{atom}}}{k_B T}\right)\right]$ is in general expected to be much weaker than the temperature dependence of the term $\left[\exp\left(-\frac{Q_{iso}}{k_B T}\right)\right]$ as $\Delta G_{lc,\,\mathrm{atom}} \ll Q_{iso}$. For instance, a value of $\Delta G_{lc} \approx 4.2\,\mathrm{kJ/mol}$ was determined for AgInSbTe around $T_{c,p}^{(80)}$ (Fig. 3.17). Conversion yields $\Delta G_{lc,\,\mathrm{atom}} \approx 44\,\mathrm{meV}$. In contrast, the isoconfigurational activation energy for AgInSbTe is $Q_{iso} = 1.33\,\mathrm{eV}$. Therefore, $Q_{iso}/\Delta G_{lc,\,\mathrm{atom}} \approx 30$ and the temperature dependence of the growth velocity is dominated by the viscosity part:

$$u_{cg}^{(dl)} \propto \exp\left(-\frac{Q_{iso}}{k_B T}\right). \tag{9.2b}$$

For *low* heating rates crystal growth can be roughly approximated to occur under *isothermal* conditions. Therefore, the Johnson-Mehl-Avrami equation [Eq. (8.11)] is expected to apply. If one restricts oneself to the steady state only, the temperature dependence of the rate constant k_m [Eq. (8.13)] can be evaluated using Eqs. (9.1) and (9.2b):

$$\begin{aligned} k_m(T) &\propto (u_{cg}^{(dl)})^{(3/4)} \cdot (I_{ss}^{(dl)})^{(1/4)} \\ &\propto \exp\left(-\frac{Q_{iso}}{k_B T}\right)^{(3/4)} \cdot \exp\left(-\frac{Q_{iso} + \Delta G_c}{k_B T}\right)^{(1/4)} \\ &\propto \exp\left(-\frac{Q_{iso} + \frac{1}{4}\Delta G_c}{k_B T}\right). \end{aligned}$$

The asterisk ($*$) was dropped now as the Johnson-Mehl-Avrami model assumes homogeneous nucleation [$f(\theta) = 1$]. By comparison with Eq. (8.14) one obtains:

$$\boxed{E_A = Q_{iso} + \frac{1}{4}\Delta G_c}. \tag{9.4}$$

At this point the assumptions stated for the derivation of Eq. (9.4) may be repeated clearly arranged:

1. Crystallization occurs diffusion limited.
2. The Stokes-Einstein relation [Eq. (8.7)] can be used to approximate the relation between the diffusivity D and the viscosity η.
3. $\Delta G_{lc,\text{ atom}} \ll Q_{iso}$ is valid for all three phase change alloys.
4. The crystal nucleation frequency is constant in time (steady state).
5. Crystal growth occurs in three dimensions in isotropic, infinitively spread space.
6. Crystal growth occurs by homogeneous nucleation.
7. Crystal growth occurs isothermally.
8. The temperature dependence of the viscosity around the peak crystallization temperature $T_{c,p}$ can be approximated by Eq. (4.9) (i. e. $T_{c,p} < T_g$).
9. The temperature dependence of the viscosity in the isoconfigurational states can be approximated to be Arrhenius *over a wide temperature range*. Therefore, the value for Q_{iso}, which was measured for a temperature range between 60 ℃ and 120 ℃, can be used to approximate the temperature dependence of the viscosity in the isoconfigurational states around $T_{c,p}$, where E_A was measured.

Assumptions (1.) – (3.) are expected to be valid. Deviations from assumptions (4.) – (6.) (i. e. crystal growth in only two dimensions or a nucleation frequency that is non-equal to zero only at the initial stage of nucleation) change the factor of 1/4 only slightly and therefore do not affect the following conclusions *qualitatively*. If one confines oneself to 'low' heating rates, crystallization occurs 'approximately' isothermally [assumption (7.)] and the validity of Eq. (9.4) is not affected qualitatively. The same is expected for assumption (9.): A slightly temperature dependent value for Q_{iso} does not affect the conclusions presented hereafter qualitatively. The most questionable assumption by far is assumption (8.). For 'low' heating rates ($\dot{T} \leq 80\,\mathrm{K/min}$), T_g was not observed to be lower than the *onset* temperature of crystallization T_c (Chapter 3.3). Therefore, T_g might be slightly higher than T_c or even slightly higher than $T_{c,p}$, and assumption (8.) may be valid for 'low' heating rates. However, experience indicates that the heating rate dependence of T_g is often weaker than the heating rate dependence of $T_{c,p}$ [30]. Therefore, T_g may be *lower* than $T_{c,p}$ for 'ultrahigh' heating rates ($\dot{T} \gg 80\,\mathrm{K/min}$), and Eq. (4.9) is not an appropriate approximation any more.

In summary: The conclusions drawn from Eq. (9.4), which are presented hereafter, may be qualitatively valid for 'low' heating rates. However, one has to be careful with these conclusions for 'ultrahigh' heating rates, which are applied for the bit erasure in rewritable CDs.

Equation (9.4) yields a quantitative separation of nucleation and growth, which has not yet been obtained for the phase change alloys: The effective activation energy for crystallization E_A is known from Table 3.4 and the isoconfigurational activation energy Q_{iso} from Table 6.5. Therefore, ΔG_c can be evaluated. According to Table 9.1, ΔG_c is much larger for $Ge_4Sb_1Te_5$ and AgInSbTe than for $Ge_2Sb_2Te_5$. In contrast to Q_{iso}, ΔG_c does not scale with the peak melting temperature T_m, due to the low value of E_A for $Ge_2Sb_2Te_5$. *Therefore, it can be concluded that the nucleation barrier ΔG_c is the important quantity that determines the crystallization mechanism as Q_{iso} does not differ significantly for the three materials:* The crystallization of $Ge_4Sb_1Te_5$ and AgInSbTe is expected to occur *diffusion controlled* or *growth controlled* as the high value for ΔG_c does not enable efficient nucleation [Eq. (9.1)]. On the other hand, due to the relatively low value for ΔG_c of $Ge_2Sb_2Te_5$ this alloy is expected to crystallize *nucleation controlled* [Eq. (9.1)].

An experimental confirmation of this statement for 'low' heating rates cannot be given here as no experimental data focusing on this topic are available. However, experimental data exist for 'ultrahigh' heating rates (i. e. for the erasure (*re*-crystallization) of amorphous marks in a crystalline matrix of a rewritable CD using laser power). Even though assumptions (7.) – (9.) are expected to be violated for 'ultrahigh' heating rates, it is *amazing* that Eq. (9.4) agrees qualitatively with the experiment in this

Table 9.1: Isoconfigurational activation energy Q_{iso} for the viscosity of the amorphous phase, effective activation energy for crystallization E_A, and nucleation barrier ΔG_c evaluated from Eq. (9.4).

	Q_{iso} (eV)	E_A [a] (eV)	ΔG_c (eV)
$Ge_4Sb_1Te_5$	1.94 ± 0.09	3.48 ± 0.12	6.16 ± 0.84
$Ge_2Sb_2Te_5$	1.76 ± 0.05	2.24 ± 0.11	1.92 ± 0.64
AgInSbTe	1.33 ± 0.09	3.03 ± 0.17	6.80 ± 1.04

[a] from Refs. [19, 33, 26, 34, 13, 24]

case. Equation (9.4) explains that amorphous bits of $Ge_4Sb_1Te_5$ and AgInSbTe *re*-crystallize by the growth of the crystalline phase *from the rim* of the amorphous bit: The re-crystallized bit area fraction decreases with increasing bit diameter if the laser power and the laser pulse length are unchanged [75]. Therefore, *re*-crystallization is *indeed observed* to occur diffusion controlled (diffusion at the rim of the amorphous bit). In contrast, *re*-crystallization of $Ge_2Sb_2Te_5$ is observed to occur by the growth of subcritical nuclei *inside* the amorphous bit: The re-crystallized bit area is independent of bit diameter [75]. Therefore, re-crystallization is *indeed observed* to occur nucleation controlled for $Ge_2Sb_2Te_5$. In addition, the observation of melt crystallization in $Ge_2Sb_2Te_5$ indicates a fast nucleation process for this material [75]. Melt crystallization is not observed for $Ge_4Sb_1Te_5$ and AgInSbTe, which is indicative for a slow nucleation process.

Hence, the commonly used term *fast nucleation material* is appropriate for $Ge_2Sb_2Te_5$: Due to the low value for ΔG_c, the crystal nucleation frequency is rather high [Eq. (9.1)]. However, the commonly used term *fast growth material* is inappropriate for $Ge_4Sb_1Te_5$ and AgInSbTe. These two alloys should rather be called *slow nucleation materials*: They do not exhibit a faster crystal growth velocity than $Ge_2Sb_2Te_5$ due to similar values for Q_{iso} [Eq. (9.2b)]; they rather exhibit a lower nucleation frequency [Eq. (9.1)].

It remains an open question why Eq. (9.4) agrees with the experiment for 'ultrahigh' heating rates. In order to clarify this further, additional phase change alloys may be investigated on their re-crystallization mechanisms, and their activation barriers E_A and Q_{iso} may be measured. However, it is probably more helpful to direct the attention to the regime of the undercooled liquid, where crystallization is more likely to occur at 'ultrahigh' heating rates. If the undercooled liquid is not available for physical measurements, equilibrium properties have to be estimated based on measurements in the amorphous, liquid and crystalline phase (as it was done in Chapter 3). Moreover, attempts should be made to estimate the glass transition temperature more precisely. Eventually, this will answer the question whether the qualitative agreement of Eq. (9.4) with the experiment at 'ultrahigh' heating rates has a profound physical reason.

Conclusions Part III

A preliminary model was suggested, which yields a quantitative separation of nucleation and growth upon crystallization of the Te alloys. The magnitude of the activation energy for crystallization E_A was compared with the magnitude of the isoconfigurational activation energy Q_{iso} for the viscosity for each alloy. As a result, the magnitude of the nucleation barrier ΔG_c could be identified as the criterion for the differentiation between fast nucleation and fast growth (i. e. slow nucleation) materials.

Part IV

Appendix

Appendix A

On the ease of glass formation

Figure A.1 qualitatively displays the variation of the homogeneous steady state crystal nucleation frequency $I_{ss}^{(dl)}$ and the crystal growth velocity $u_{cg}^{(dl)}$ for diffusion limited crystallization in the regime of the undercooled liquid. Both quantities are plotted in a logarithmic representation as a function of reduced temperature $T_r = T/T_l$, where T_l is the melting point of liquidus temperature. The calculations are based on Eqs. (8.8) and (8.10). The curve parameter is the reduced glass transition temperature $T_{rg} = T_g/T_l$. A Fulcher-Vogel equation [Eq. (4.2)] was assumed for the temperature dependence of the viscosity η. Further assumptions were a unique melting point $T_l = T_m$ (as for a single component system), a glass transition temperature T_g equal to the temperature T_0 defined in Eq. (4.2) (where the viscosity diverges), a crystal-melt interfacial tension σ proportional to T_r, homogeneous nucleation [$f(\theta) = 1$] and a difference in Gibbs free energy between undercooled liquid and crystal ΔG_{lc} proportional to the undercooling $\Delta T_r = (1 - T_r)$. Save for the assumption of a Fulcher-Volgel equation, deviations from the other assumptions do not affect the shape of the curves qualitatively. Therefore, the dominant influence on the shape of the curves *by far* is the viscosity rise, which is determined by the value for T_{rg}. The curves for $I_{ss}^{(dl)}$ and $u_{cg}^{(dl)}$ differ by the position of their maxima: The maximum of $u_{cg}^{(dl)}$ is located at a higher temperature than the maximum of $I_{ss}^{(dl)}$ for the same value of T_{rg}, which is due to the different temperature dependence of Eqs. (8.8) and (8.10).

It was one of David Turnbull's preeminent contributions to science to identify the magnitude of $T_{rg} = T_g/T_l$ as the criterion for the ease of glass formation [3]: He was able to show that the maximum crystal nucleation frequency is negligibly small for $T_{rg} > \frac{2}{3}$. Therefore, glass formation upon melt quenching is almost 'guaranteed' in this case. He also pointed out that the minimum cooling rate $|\dot{T}_{min}|$ required to prevent nucleation and growth and hence enable glass formation increases with decreasing value for T_{rg}. This led to the discovery of several easy glass formers: Since the glass transition temperature T_g is in general less composition dependent than the liquidus temperature T_l, the easiest glass formers were expected and indeed found at the minimum value for T_l, i. e. at the eutectic composition.

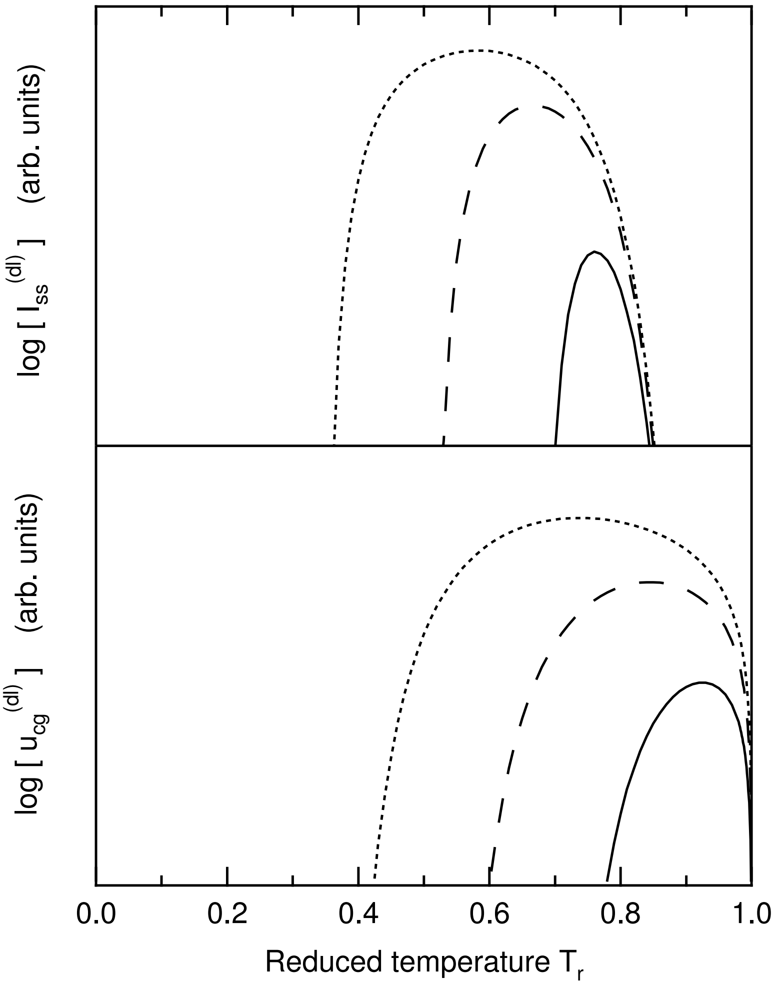

Figure A.1: Nucleation frequency $I_{ss}^{(dl)}$ and crystal growth velocity $u_{cg}^{(dl)}$ for three values of the reduced glass transition temperature: $T_{rg} = \frac{2}{3}$ (solid), $T_{rg} = \frac{1}{2}$ (dashed), and $T_{rg} = \frac{1}{3}$ (dotted).

Appendix B

Acknowledgements

First, I would like to thank my advisors Prof. Dr. Matthias Wuttig and Prof. Dr. Frans Spaepen for giving me the opportunity to work on a challenging and sophisticated research project in two different laboratories located in two different countries. I enormously benefited from this, as it extensively broadened my mind in terms of science, new experiences and way of living.

Matthias Wuttig is gratefully acknowledged for several encouraging discussions and suggestions, which gave me direction and inspiration. Due to him the working atmosphere in the lab was always very pleasant, which provided an important basis for enjoyable but effective work.

I consider myself extraordinarily fortunate to have had the opportunity to work closely with Frans Spaepen. I benefited extensively from his enormous physical insight and scientific experience. Discussions with him were always absolutely constructive.

When Robert Graham went to meet me at Logan Airport, I had no idea that the next months would exceed all of my expectations. I just loved it there - America, Boston and Harvard. I made so many things and met so many nice people. I sincerely thank Robert Graham for accepting me to the *Research Experience for Undergraduates* program and for his kind assistance during my stay. Plus, for organizing several volleyball games.

The *Harvard Materials Research Science and Engineering Center* (funded by the *National Science Foundation*), the *Ministerium für Schule, Wissenschaft und Forschung des Landes Nordrhein-Westfalen* and the *Deutscher Akademischer Aus-*

tauschdienst are gratefully acknowledged for providing the financial basis for my stay at Harvard.

Several people contributed to this research project by their kind assistance. First of all, Tom Pedersen helped me a lot with the operation of the wafer curvature setup. I also had several pleasant and useful discussions with him. Elizabeth Shack is acknowledged for help with the DSC measurements. Dillon Fong and Denis Yu assisted me with the wafer curvature measurements. Henning Dieker, Daniel Wamwangi, Stefan Hermes and Stefan Ziegler supported me with the sample preparation. Henning also did the XRD measurements. Han-Willem Wöltgens, Ralf Detemple, Stefan Ziegler, Daniel Wamwangi, Walter Njoroge and Oliver Heinen are acknowledged for useful discussions on phase change materials. Han-Willem did the electrical film resistance measurements. Oliver Kappertz supported me with the film thickness determination.

Frans Spaepen, Matthias Wuttig and Tom Pedersen are gratefully acknowledged for their help on the elaboration of this thesis concerning linguistic and stylistic problems of the English language.

I am very grateful to my fellow students and long standing friends Linus Lindfeld, Carsten Schmitz, Christian Panofen and Henning Dieker. Studying with them for several years was of enormous benefit to me, as they are all excellent physicists. I am utmost fortunate that I got to know them and can really call them friends. I wish the best to all of them.

Last but not least, my parents are gratefully acknowledged for their great support during my graduation.

Bibliography

[1] C. Kittel. *Einführung in die Festkörperphysik.* Oldenbourg, Munich, 9th edition, 1991.

[2] M.H. Cohen and D. Turnbull. Molecular transport in liquids and glasses. *Journal of Chemical Physics*, 31:1164, 1959.

[3] D. Turnbull. Under what conditions can a glass be formed? *Contemporary Physics*, 10:473, 1969.

[4] F. Spaepen. The identification of the metallic glass state. In *Materials Research Society Symposia Proceedings*, volume 57, page 161, 1986.

[5] W. Kauzmann. The nature of the glassy state and the behavior of liquids at low temperatures. *Chemical Reviews*, 43:219, 1948.

[6] D.R. Uhlmann and N.J. Kreidl, editors. *Glass: Science and Technology*, volume 3. Academic Press, 1986.

[7] S.I. Tsao. *Structural Relaxation and Isoconfigurational Flow in Metallic Glasses.* PhD thesis, Harvard University, 1983.

[8] S. Roorda, J.M. Poate, D.C. Jacobson, D.J. Eaglesham, B.S. Dennis, S. Dierker, W.C. Sinke, F. Spaepen, and P. Fuoss. Structural relaxation and defect annihilation in pure amorphous silicon. *Physical Review B*, 44:3702, 1991.

[9] H.S. Chen, L.C. Kimerling, J.M. Poate, and W.L. Brown. Diffusion in a Pd-Cu-Si metallic glass. *Applied Physics Letters*, 32:461, 1978.

[10] M.P. Rosenblum, F. Spaepen, and D. Turnbull. Diffusion and structural relaxation in compositionally modulated amorphous metal films. *Applied Physics Letters*, 37:184, 1980.

[11] A.I. Taub and F. Spaepen. The kinetics of structural relaxation of a metallic glass. *Acta Metallurgica*, 28:1781, 1980.

[12] J.R. Hook and H.E. Hall. *Solid State Physics*. John Wiley & Sons, New York, 2nd edition, 1991.

[13] W.K. Njoroge and M. Wuttig. Crystallization kinetics of sputter-deposited amorphous AgInSbTe films. *Journal of Applied Physics*, 90:3816, 2001.

[14] H.-W. Wöltgens, R. Detemple, I. Friedrich, W.K. Njoroge, I. Thomas, V. Weidenhof, S. Ziegler, and M. Wuttig. Exploring the limits of fast phase change materials. In *Materials Research Society Symposia Proceedings*, volume 674, page V1.3, 2001.

[15] J. Feinleib, J. deNeufville, S.C. Moss, and S.R. Ovshinsky. Rapid reversible light-induced crystallization of amorphous semiconductors. *Applied Physics Letters*, 18:254, 1971.

[16] N. Akahira, N. Miyagawa, K. Nishiuchi, Y. Sakaue, and E. Ohno. *Proceedings of the International Society for Optical Engineering (SPIE)*, 2514:294, 1995.

[17] N. Nobukuni, M. Takashima, T. Ohno, and M. Horie. Microstructural changes in GeSbTe film during repetitious overwriting in phase-change optical recording. *Journal of Applied Physics*, 78:6980, 1995.

[18] N. Yamada. Erasable phase-change optical materials. *Materials Research Society Bulletin*, 21:48, 1996.

[19] D. Wamwangi, W.K. Njoroge, and M. Wuttig. Crystallization kinetics of $Ge_4Sb_1Te_5$ films. *Thin Solid Films*, 408:310, 2002.

[20] V. Weidenhof, I. Friedrich, S. Ziegler, and M. Wuttig. Atomic force microscopy study of laser induced phase transitions in $Ge_2Sb_2Te_5$. *Journal of Applied Physics*, 86:5879, 1999.

[21] IGOR PRO 4.01 program by Wave Metrics.

[22] T. Massalski, editor. *Binary Alloy Phase Diagrams.* ASM International, Materials Park, OH, 2nd edition, 1990.

[23] N.Kh. Abrikosov and G.T. Danilova-Dobryakova. An investigation of the structural diagram of Sb_2Te_3-GeTe. *Translated from Izvestiya Akademii Nauk SSSR, Neorganicheskie Materialy*, 1:204, 1965.

[24] N. Yamada, E. Ohno, K. Nishiuchi, N. Akahira, and M. Takao. Rapid phase transitions of GeTe-Sb_2Te_3 pseudobinary amorphous thin films for an optical disk memory. *Journal of Applied Physics*, 69:2849, 1991.

[25] T.H. Jeong, M.R. Kim, H. Seo, S.J. Kim, and S.Y. Kim. Crystallization behavior of sputter-deposited amorphous $Ge_2Sb_2Te_5$ thin films. *Journal of Applied Physics*, 86:774, 1999.

[26] J. Park, M.R. Kim, W.S. Choi, H. Seo, and C. Yeon. Characterization of amorphous phases of $Ge_2Sb_2Te_5$ phase-change optical recording material on their crystallization behavior. *Japanese Journal of Applied Physics*, 38:4775, 1999.

[27] E. Morales-Sanchez, E.F. Prokhorov, A. Mendoza-Galvan, and J. Gonzalez-Hernandez. Determination of the glass transition and nucleation temperatures in $Ge_2Sb_2Te_5$ sputtered films. *Journal of Applied Physics*, 91:697, 2002.

[28] H. Seo, T.-H. Jeong, J.-W. Park, C. Yeon, S.-J. Kim, and S.-Y. Kim. Investigation of crystallization behavior of sputter-deposited nitrogen-doped amorphous $Ge_2Sb_2Te_5$ thin films. *Japanese Journal of Applied Physics*, 39:745, 2000.

[29] E.F. Prokhorov (author of Ref. [27]), private communication.

[30] F. Spaepen, private communication.

[31] O. Heinen, private communication.

[32] H.E. Kissinger. Reaction kinetics in differential thermal analysis. *Analytical Chemistry*, 29:1702, 1957.

[33] N. Yamada, E. Ohno, N. Akahira, K. Nishiuchi, K. Nagata, and M. Takao. High speed overwritable phase change optical disk material. *Japanese Journal of Applied Physics*, 26, Supplement 26–4:61, 1987.

[34] I. Friedrich, V. Weidenhof, W. Njoroge, P. Franz, and M. Wuttig. Structural transformations of $Ge_2Sb_2Te_5$ films studied by electrical resistance measurements. *Journal of Applied Physics*, 87:4130, 2000.

[35] J.A. Mullin. *Viscous Flow and Structural Relaxation in Amorphous Silicon and Amorphous Selenium Thin Films.* PhD thesis, Harvard University, 2000.

[36] H. Vogel. Das Temperaturabhängigkeitsgesetz der Viskosität von Flüssigkeiten. *Physikalische Zeitschrift*, 22:645, 1921.

[37] G.S. Fulcher. Analysis of recent measurements of the viscosity of glasses. *Journal of the American Ceramic Society*, 8:339, 1925.

[38] F. Spaepen and D. Turnbull. Metallic glasses. *Annual Review of Physical Chemistry*, 35:241, 1984.

[39] F. Spaepen. *Physics of Defects.* Les Houches XXXV. North-Holland, Amsterdam, 1981. Page 133.

[40] R.C. Weast, editor. *CRC Handbook of Chemistry and Physics.* CRC Press, Boca Raton, FL, 60th edition, 1979.

[41] S.S. Tsao and F. Spaepen. Structural relaxation of a metallic glass near equilibrium. *Acta Metallurgica*, 33:881, 1985.

[42] G.J. Roberts and J.P. Roberts. *7th International Conference on Glass*, 31, 1965.

[43] H.R. Lillie. *Journal of the American Ceramic Society*, 16:619, 1933.

[44] C.A. Volkert. *Flow and Relaxation of Amorphous Metals.* PhD thesis, Harvard University, 1988.

[45] D. Turnbull and M.H. Cohen. Free-volume model of the amorphous phase: glass transition. *Journal of Chemical Physics*, 34:120, 1961.

[46] D. Turnbull and M.H. Cohen. On the free-volume model of the liquid-glass transition. *Journal of Chemical Physics*, 52:3038, 1970.

[47] A. Witvrouw. *Viscosity and Elastic Constants of Amorphous Thin Films.* PhD thesis, Harvard University, 1992.

[48] A. Witvrouw and F. Spaepen. Viscosity and elastic constants of amorphous Si and Ge. *Journal of Applied Physics*, 74:7154, 1993.

[49] J.F. Nye. *Physical properties of crystals: their representation by tensors and matrices.* Clarendon Press, Oxford, 1985.

[50] F.A. McClintock and A.S. Argon, editors. *Mechanical Behavior of Materials.* Addison-Wesley, Reading, 1966.

[51] R.J. Drese. *Stresses and Recrystallization in Thin Metallic Films.* Diploma thesis, RWTH Aachen, 2000.

[52] G.G. Stoney. *Proceedings of the Royal Society of London, Series A*, 82:172, 1909.

[53] W.D. Nix. Mechanical properties of thin films. *Metallurgical and Materials Transactions A*, 20 A:2217, 1989.

[54] M. Ohring. *The materials science of thin films.* Academic Press, 1992.

[55] W.A. Brantley. Calculated elastic constants for stress problems associated with semiconductor devices. *Journal of Applied Physics*, 44:534, 1973.

[56] W.E. Tefft. Elastic constants of synthetic single crystal corundum. *Journal of Research of the National Bureau of Standards*, 70A:277, 1966.

[57] G.K. White. Reference materials for thermal expansion: certified or not? *Thermochimica Acta*, 218:83, 1993.

[58] H. Dieker. *Charakterisierung von Chalkogenidlegierungsschichten mittels Röntgenreflektometrie und spektroskopischer Ellipsometrie.* Diploma thesis, RWTH Aachen, 2002.

[59] U. Laudahn, S. Fähler, H.U. Krebs, A. Pundt, M. Bicker, U. v. Hülsen, U. Geyer, and R. Kirchheim. Determination of elastic constants in thin films using hydrogen loading. *Applied Physics Letters*, 74:647, 1999.

[60] A. Einstein. Eine neue Bestimmung der Moleküldimensionen. *Annalen der Physik*, 19:289, 1906.

[61] A. Einstein. Berichtigung zu meiner Arbeit "Eine neue Bestimmung der Moleküldimensionen". *Annalen der Physik*, 34:591, 1911.

[62] K.-H. Robrock. *Dünne Schichten und Schichtsysteme: Bruch- und Haftfestigkeit von Schichten.* 17. IFF-Ferienkurs im Forschungszentrum Jülich, March 1986. Page 429.

[63] W.K. Njoroge (author of Ref. [13]), private communication.

[64] L. Pauling. *The nature of the chemical bond.* Cornell University Press, Ithaca, NY, 3rd edition, 1960.

[65] J. Ngaruiya, private communication.

[66] F. Spaepen. *Lectures on phase transformations.* Lecture notes for students, Leuven, Belgium, Fall 1984.

[67] F. Spaepen and R.B. Meyer. The surface tension in a structural model for the solid-liquid interface. *Scripta Metallurgica*, 10:257, 1976.

[68] C.V. Thompson and F. Spaepen. Homogeneous crystal nucleation in binary metallic melts. *Acta Metallurgica*, 31:2021, 1983.

[69] F. Spaepen. Homogeneous nucleation and the temperature dependence of the crystal-melt interfacial tension. *Solid State Physics*, 47:1, 1994.

[70] R. Becker and W. Döring. Kinetische Behandlung der Keimbildung in übersättigten Dämpfen. *Annalen der Physik*, 24:719, 1935.

[71] D.R. Uhlmann and N.J. Kreidl, editors. *Glass: Science and Technology*, volume 1. Academic Press, 1983.

[72] M. Avrami. Kinetics of phase change. I. General theory. *Journal of Chemical Physics*, 7:1103, 1939.

[73] W.A. Johnson and R.F. Mehl. Reaction kinetics in process of nucleation and growth. *Transactions of the American Institute of Mining, Metallurgical and Petroleum Engineers*, 135:416, 1939.

[74] J.-Y. Raty, J.-P. Gaspard, M. Bionducci, R. Ceolin, and R. Bellissent. On the structure of liquid IV-VI semiconductors. *Journal of Non-Crystalline Solids*, 250–252:277, 1999.

[75] R. Detemple, I. Friedrich, W. Njoroge, I. Thomas, V. Weidenhof, H.-W. Wöltgens, S. Ziegler, and M. Wuttig. Microscopic studies of fast phase transformations in GeSbTe films. In *Materials Research Society Symposia Proceedings*, volume 674, page V1.8, 2001.